

Control Layout of Doubly Fed Induction Generator with Respect to Low Voltage Ride Through for Wind Energy Conversion System

Vorgelegt von
M. Sc. Eng.
Alaa Al-Quteimat
geb. in Oman

von der Fakultät IV - Elektrotechnik und Informatik
der Technischen Universität Berlin
zur Erlangung des akademischen Grades
Doktor der Ingenieurwissenschaften
- Dr.-Ing. -

genehmigte Dissertation

Promotionsausschuss:

Vorsitzender: Prof. Dr.-Ing. Ronald Plath
Gutachter: Prof. Dr.-Ing. Uwe Schäfer
Gutachterin: Prof. Dr. Ing. Sibylle Dieckerhoff
Gutachter: Prof. Dr. Saleh Al-Jufout

Tag der wissenschaftlichen Aussprache: 24. August 2018

Berlin 2018

Acknowledgements

Most of all, I would like to express my sincere gratitude and deepest appreciation to my supervisor Prof. Dr. Ing. Uwe Schäfer for the continuous support and guidance in my PhD study and related research, for his patience, motivation, and immense knowledge. His guidance helped me throughout all the time researching and writing this thesis. Without his valuable suggestions and guidelines, this research work would not have materialized.

I would like to thank my parents, brothers, and sisters for their blessings and for being a constant source of encouragement and support; I am forever grateful.

Last but not least, I would like to thank my loving and supportive husband, Abdullah, for always being the shoulder I could lean on throughout my study, and my children Mohammad and Rayyan for filling my heart with love and strength.

Abstract

Moving forward, the demand on renewable energy resources is increasing due to their advantages over the fossil fuels, which have harmful effects on the environment. Currently, doubly fed induction generators (DFIG) are widely used for wind turbines. Compared to other variable-speed generators; the main advantage of the DFIG is that the power electronic devices must deal with only about a third of the generator power, compared to full power converters used in synchronous generators [1, 2]. This difference reduces the costs and losses in the power electronic components, rather than other solutions, such as fully converting systems; finally, the overall efficiency is improved.

Field-oriented control (FOC) and direct control algorithms are used to control the performance of DFIG wind energy. Due to complexity and machine parameters dependency, the direct control techniques are gradually replacing the conventional FOC [3]. Two direct control strategies are implemented in this work, direct torque control (DTC) and direct power control (DPC).

This dissertation deals with the performance analysis, modeling, and control of DFIG-based wind energy conversion.

Controllers for rotor side converter (RSC) and grid side converter (GSC) are analyzed. DTC is used in this work to control the RSC; several approaches of this control technique will be presented and the results are compared according to the total harmonic distortion (THD) and ripples to define the best performance. Moreover, DPC is applied and the performance of active and reactive power is analyzed. The grid synchronization of DFIG is an important issue to be discussed, as the DFIG can be controllable only around synchronous speed. It will lose its controllability during startup since the voltage requested from the machine at that time is higher than the voltage requested at normal operations around the synchronous speed.

DFIG under voltage dip is also discussed and analyzed under symmetrical and asymmetrical grid faults. The possible solutions of low voltage ride through to meet grid-codes requirements is presented, and the selected algorithm is discussed in detail. Last, the results are thus compared.

Zusammenfassung

In der Zukunft steigt die Nachfrage nach erneuerbaren Energiequellen aufgrund ihrer Vorteile gegenüber den fossilen Brennstoffen, die schädliche Auswirkungen auf die Umwelt haben. Gegenwärtig werden doppelt gespeiste Induktionsgeneratoren (DFIG) für Windkraftanlagen häufig verwendet. Im Vergleich zu anderen Generatoren mit variabler Drehzahl besteht der Hauptvorteil des DFIG darin, dass die Leistungselektronikgeräte nur etwa ein Drittel der Generatorleistung im Vergleich zu Vollumrichtern mit Synchrongeneratoren bewältigen müssen [1, 2]. Dies verringert die Kosten und die Verluste in den leistungselektronischen Komponenten im Vergleich zu anderen Lösungen wie Vollumwandlungssystemen; weiterhin wird die Gesamteffizienz verbessert. Feldorientierte Regelung (FOC) und direkte Steuerungsalgorithmen werden verwendet, um die Leistung der DFIG-Windenergie zu steuern. Aufgrund der Komplexität und der Abhängigkeit von Maschinenparametern ersetzen die direkten Steuerungstechniken allmählich die herkömmliche FOC [3]. Zwei direkte Steuerstrategien wurden in dieser Arbeit implementiert, direkte Drehmomentsteuerung (DTC) und direkte Leistungssteuerung (DPC).

Diese Dissertation befasst sich mit der Leistungsanalyse, Modellierung und Steuerung der DFIG-basierten Windenergiekonversion. Regler für den rotorseitigen Umrichter (RSC) und den netzseitigen Umrichter (GSC) werden analysiert. In dieser Arbeit wird DTC verwendet, um den RSC zu steuern. Mehrere Ansätze dieser Steuerungstechnik werden präsentiert und die Ergebnisse werden entsprechend der gesamten harmonischen Verzerrung und der Rippleströme verglichen, um das bestgeeignete System festzulegen. Darüber hinaus wird DPC angewendet, und Wirk- und Blindleistung werden analysiert.

Die Netzsynchronisation bei DFIG ist ein wichtiges zu diskutierendes Thema. Der DFIG ist nur um die synchrone Geschwindigkeit sinnvoll steuerbar, so dass es während des Starts seine Steuerbarkeit verliert, da die von der Maschine während des Startens benötigte Spannung höher ist als die bei normalem Betrieb um die synchrone Geschwindigkeit erforderliche. DFIG unter Spannungseinbrüchen wird auch in dieser Arbeit unter symmetrischen und asymmetrischen Netzfehlern diskutiert und analysiert. Die möglichen Lösungen für LVRT (Low Voltage Ride Through) zur Erfüllung der Anforderungen der Grid-Codes werden vorgestellt und der ausgewählte Algorithmus wird im Detail diskutiert. Abschließend werden die Ergebnisse verglichen.

Table of Contents

Nomenclature	viii
1 Introduction	1
1.1 Wind Energy Development	1
1.2 Wind Turbines Concept	2
1.3 DFIG Principle and Advantages	4
1.4 Literature Review	6
1.5 Thesis Layout	8
1.6 Chapter Conclusion	9
2 Dynamic Modeling of Doubly Fed Induction Generator	10
2.1 Doubly Fed Induction Machine Expressed in the ABC Reference Frame	10
2.2 Reference Frames and the Two-Axis Transformation	16
2.2.1 Space Vector Representation	16
2.2.2 DFIG Model Expressed in the $\alpha\beta$ Reference Frame	17
2.2.3 DFIG Model Expressed in the dq Reference Frame	18
2.2.4 Power and Torque in dq Reference Frame	20
2.2.5 The Mechanical Subsystem	21
2.3 Chapter Conclusion	21
3 Rotor Side Converter Control	22
3.1 Direct Torque Control for DFIG	23
3.1.1 DTC Implementation	26
3.1.2 Electromagnetic Torque and Rotor Flux Estimation	27
3.1.3 Electromagnetic Torque and Rotor Flux Reference Values Determination	28
3.1.4 Hysteresis Controllers and Rotor Voltage Vector Selection	29
3.1.5 Switching Control	31
3.2 DTC Improvement	32
3.2.1 Twelve Sectors DTC	32
3.2.2 Modified Switching Table DTC	34

3.3	Simulation Results and Discussion	35
3.3.1	Conventional DTC	36
3.3.2	Twelve Sectors DTC	38
3.3.3	DTC with Modified Switching Table	39
3.3.4	Comparison and Discussion	40
3.4	Direct Power Control for DFIG	42
3.4.1	DPC Implementation	45
3.4.2	Active Power, Reactive Power and Stator Flux Estimation	45
3.4.3	Active Power Reference	46
3.4.4	Hysteresis Controllers and Rotor Voltage Vector Selection	46
3.4.5	Simulation Results and Discussion	47
3.5	Chapter Conclusion	48
4	Grid Side Converter	49
4.1	Grid Side Converter Structure	49
4.2	Vector Control	51
4.3	Reference Frame Alignment	54
4.3.1	Zero Crossing Method	54
4.3.2	Arctangent Method	55
4.3.3	Phase Locked Loop	55
4.3.4	Reference Frame Method Selection	55
4.4	LCL Filter Design	57
4.4.1	Filter Parameters	58
4.5	Chapter Conclusion	61
5	Synchronization	62
5.1	Principles of Direct Virtual Torque Control	62
5.2	DVTC for Grid Synchronization	64
5.3	Chapter Conclusion	66
6	Low Voltage Ride Through for DFIG	67
6.1	LVRT Grid Codes Requirements for a DFIG Wind Turbine	67

6.2	DFIG Under Voltage Dip	69
6.2.1	Voltage Sag Generator	69
6.2.2	DFIG Behavior Under Grid Fault	71
6.2.3	Simulation Results and Discussion	71
6.3	LVRT Solutions	77
6.3.1	Crowbar Protection	78
6.4	Practical Implementation of Impedance Based Voltage Sag Generator for 3.5 kW DFIG	82
6.4.1	Fault Detection	83
6.4.2	Circuit Components	83
6.4.3	Test Realization	84
6.5	Chapter Conclusion	85
7	Conclusion	86
7.1	Conclusion	86
7.2	Future Work	87
7.3	Associated publications	88
	References	89
	List of Figures	101
	List of Tables	104
	Appendix A System Parameters	105
A.1	Machine Parameters	105
A.2	DC Link Parameters	106
A.3	GSC Control Parameters	106
A.4	RSC Control Parameters	107
A.5	Fault Detection Parameters	107
	Appendix B Results of 3.5 kW	108
B.1	Results of DTC Algorithms	108
B.2	DFIG under Three Phase Voltage Dip	110

Nomenclature

Roman Symbols

ΔI_{ripmax}	Maximum current ripple
C_f	Filter capacitance
eP_s, eQ_s	Active and reactive powers errors
$eT_{em}, e\Psi_r$	Torque and flux errors
f_s	Stator frequency
f_{grid}	Grid frequency
f_{res}	Resonance frequency
f_{sw}	Switching frequency
$HT_{em}, H\Psi_r$	Torque and flux hysteresis comparatos outputs
HB_T, HB_Ψ	Hysteresis band of torque and flux
HBP_s, HBQ_s	Hysteresis band of active and reactive powers
HP_s, HQ_s	Active and reactive powers hysteresis comparatos outputs
I_{abcr}	Rotor instantaneous current vector
I_{abcs}	Stator instantaneous current vector
i_{ac}, i_{bc}, i_{cc}	Currents through filter capacitor branch
i_{ag}, i_{bg}, i_{cg}	Grid currents
$i_{ar}(t), i_{br}(t), i_{cr}(t)$	Rotor currents
$i_{as}(t), i_{bs}(t), i_{cs}(t)$	Stator currents
$i_{g(f_{sw})}, i_{c(f_{sw})}$	The grid and converter currents ripple
i_{rsc}	RSC current

j	Inertia
k_p, K_i	Gains of PI controllers for grid side converter
k	Sector number in which flux is located
L_i, L_g	inverter and grid side filter inductances
L_m	Mutual inductance
L_r	Rotor inductance
L_s	Stator inductance
L_{lr}	Rotor leakage inductance
L_{ls}	Stator leakage inductance
N_r	Rotor rotational speed (r.p.m)
N_s	Synchronous speed
N_{ϕ_r}	Speed of rotor currents magnetic field
P_n	Machine rated power
P_p	Number of pole pairs
P_r, Q_r	Rotor active and reactive power
P_s, Q_s	Stator active and reactive powers
P_{gc}, Q_{gc}	Active and reactive powers of grid side converter
P_{nom}, Q_{nom}	Active and reactive powers nominal values
PI, PD, QI, QD	Increase and decrease of active and reactive powers.
PLL	Phase locked loop
R_c	Damping resistance
R_f, L_f	Resistance and inductance of L-filter

R_g, L_g	Resistance and inductance of grid
R_r	Rotor resistance
R_s	Stator resistance
T_{em}	Electromagnetic torque
T_{em}^*, ψ_r^*	Torque and flux reference values
T_{load}	Torque applied on the shaft
T_{nom}, ψ_{nom}	Torque and rotor flux nominal values
T_{set}	Settling time
T_{vi}	Virtual torque
TI, TD, FI, FD	Increase and decrease of torque and flux.
V_n	Nominal Grid voltage
V_{abcr}	Rotor instantaneous voltage vector
V_{abcs}	Stator instantaneous voltage vector
V_{sag}	Voltage during the sag condition
x	Percentage of maximum reactive power absorbed at nominal conditions
Z_1, Z_2	Series and shunt impedance
Z_b, C_b	Impedance and capacitance base values
Z_g	Grid impedance
Greek Symbols	
δ_v	Angle between real rotor flux and virtual grid flux
δ	Angle between stator and rotor flux
ω_a	Angular speed

ω_m	Rotor angular speed (rad/s)
ω_n	Undamped natural frequency
ω_s	Synchronous speed (rad/s)
ω_{gs}	Grid angular speed
ω_{mech}	Rotor mechanical rotational speed
\vec{v}_s', \vec{i}_s'	Stator voltage and current vectors in rotor reference frame
$\psi_{as}(t), \psi_{bs}(t), \psi_{cs}(t)$	Stator fluxes
σ	Leakage factor
θ_m	The angle between phase as of stator and phase ar of rotor
θ_r	Rotor angular position
θ_{ψ_r}	Rotor flux position
θ_{sg}	Virtual flux phase angle
v_{ag}, v_{bg}, v_{cg}	Grid phase voltages
v_{ar}, v_{br}, v_{cr}	Rotor voltages
v_{as}, v_{bs}, v_{cs}	Stator voltages
v_{d0}, v_{q0}	d-q components of converter voltage
v_{dc}, i_{dc}	DC link voltage and current
$v_{dg}, v_{qg}, i_{dg}, i_{qg}$	d q components of grid voltage and current
$v_{g\alpha}, v_{g\beta}$	$\alpha\beta$ components of grid voltage
$v_{rd}^a, v_{rq}^a, i_{rd}^a, i_{rq}^a, \psi_{rd}^a, \psi_{rq}^a$	dq components of rotor voltage, current, and flux in arbitrary reference frame
$v_{sd}^a, v_{sq}^a, i_{sd}^a, i_{sq}^a, \psi_{sd}^a, \psi_{sq}^a$	dq components of stator voltage, current, and flux in arbitrary reference frame

ξ	damping factor
$\vec{v}_a, \vec{v}_b, \vec{v}_c$	Space vectors voltages
$\vec{v}_{\alpha\beta r}^r, \vec{i}_{\alpha\beta r}^r, \vec{\psi}_{\alpha\beta r}^r$	Rotor space vectors of voltage, current, and flux in the $\alpha\beta$ reference frame referred to the rotor
$\vec{v}_{\alpha\beta s}^s, \vec{i}_{\alpha\beta s}^s, \vec{\psi}_{\alpha\beta s}^s$	Stator space vectors of voltage, current, and flux in the $\alpha\beta$ reference frame referred to the stator
$\psi_{ar}(t), \psi_{br}(t), \psi_{cr}(t)$	Rotor fluxes
$f_{\phi r}$	Frequency of rotor currents

Acronyms / Abbreviations

BRICS	Brazil, Russian Federation, India, China and South Africa.
DFIG	Doubly Fed Induction Generator.
DPC	Direct Power Control.
DTC	Direct Torque Control.
DVTC	Direct Virtual Torque Control.
EU-28	European Union.
FOC	Field Oriented Control.
GSC	Grid Side Converter.
GWEC	Global Wind Energy Council.
HOSM	High Order Sliding Mode.
LVRT	Low Voltage Ride Through.
NC-MBFCL	Nonlinear Control Based Modified Bridge-type Fault Current Limiter.
PCC	Point of Common Coupling.
RSC	Rotor Side Converter.

SCR	Silicon Controlled Rectifier.
SG	Synchronous Generator.
THD	Total Harmonic Distortion.
VSC	Voltage Source Converter.
WECS	Wind Energy Conversion System.
WRIM	Wound Rotor Induction Machine.

Chapter 1

Introduction

Recently, due to the increase of CO₂ emissions, the world power sector is moving away from the technologies related to fuel oil, coal, and gas, which are used as primary sources. Conversely, renewable energy systems, and especially wind energy, show continued growth in power generation around the world, as the Global Wind Energy Council (GWEC) reports in the 'Global Wind Report 2014' [4]. Renewable energy sources will account for more than one-quarter of global electricity production by 2020; the hydro power generation has the largest part of the renewable energy resources, while wind power is the second-highest renewable source from global production [5, 6]. According to the Global Status Report (Renewables 2017); wind energy contributes 4 % of electricity global production [7].

1.1 Wind Energy Development

The discovery of wind energy and its use was first in the Middle East exactly in Iran, which was known as 'Persia' in the tenth century. The vertical axis principle was employed to extract energy from the wind [8]. The first windmills were used for wheat milling and water pumping. Around the 1900s, the first windmills for electrical production were built. In the 1970s, the rapid development of wind energy technology had advanced, and large wind turbines were set in operation [9, 10].

The quick development of wind energy has strongly drawn the attention of public, political, and scientific interest [9]. By the end of 2016, the countries with the most installed electric capacity from renewable energy were China, the United States, Brazil, Germany and Canada [7]. China has more than one-quarter of the world's capacity for renewable power with a total capacity of 564 GW, which includes about 305 GW of hydropower [7]. Considering non-hydro capacity, the top countries were China, the United States, and Germany; they were followed by Japan, India, and Italy, as seen in Figure 1.1 [7].

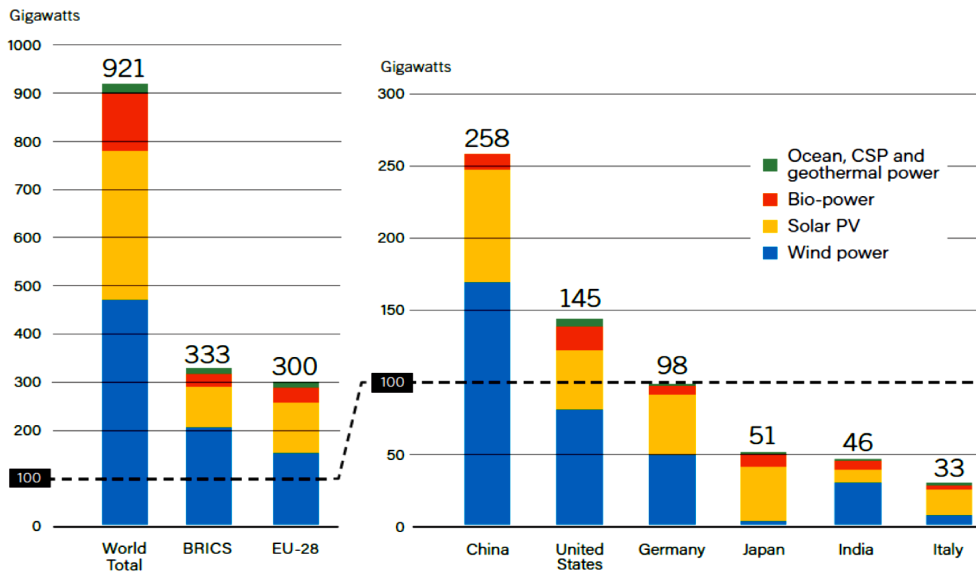


Figure. 1.1 Capacities of renewable power in world, BRICS (Brazil, Russian Federation, India, China and South Africa), EU-28 (European Union) and Top 6 Countries, 2016 [7].

1.2 Wind Turbines Concept

Wind turbines are essentially divided into two important categories depending on the behavior of wind speed variations: variable-speed and fixed-speed. In fixed-speed wind turbines asynchronous machines are typically used, but the current number of systems based on this topology is relatively low [11]. In fact, because the generator output is directly connected to the grid, the generator speed and thus the rotor turbine speed are fixed. But the wind has a variable behavior, so any fluctuation in its speed causes the mechanical power at the rotor turbine to vary, and the torque at the wind rotor turbine as well, the rotor speed is fixed (taking into consideration the slip of an induction machine, a variation of 2-3 % may be allowed). As such, each blade of wind causes stress in the mechanical components, especially in the gearbox. Moreover, the quick variations of torque can affect the output power and thus the stability of the power network to which the generator is connected. Regarding the variable-speed wind turbines, the advantage is that the rotor speed can vary as the wind speed varies. Therefore, to capture the greatest amount of power from the wind, the turbine could run at different speeds and follow a curve of maximum power extraction [12]. This assumes the form like in Figure 1.2, which shows clearly the advantage of using variable-speed wind turbines.

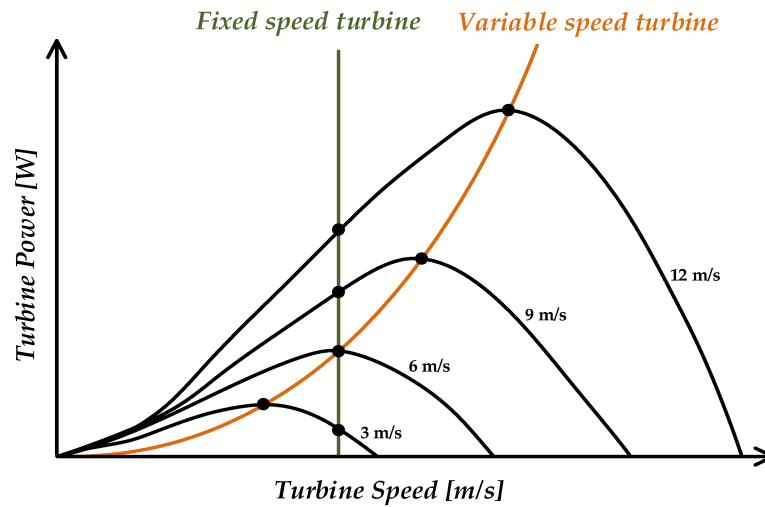


Figure. 1.2 Maximum power tracking for fixed and variable speed turbines.

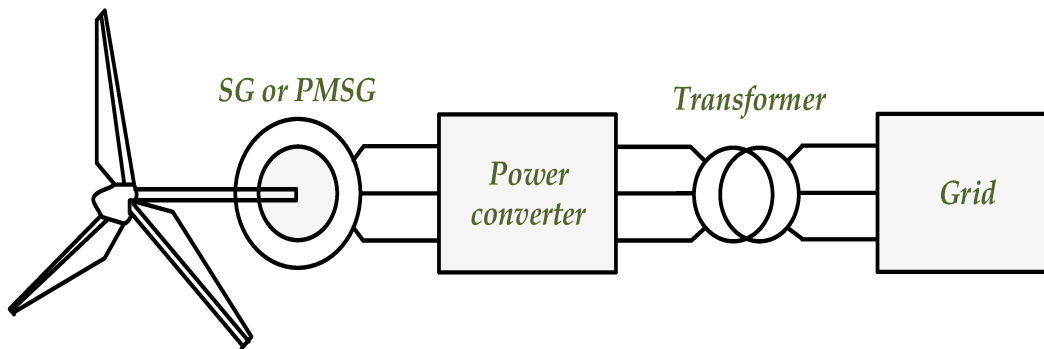


Figure. 1.3 Wind turbine configuration using Synchronous Generators.

In synchronous generators, the relationship between the frequency of output stator voltages and the synchronous speed is given by the following equation:

$$f_s = P_p \cdot N_s \quad (1.1)$$

Where N_s is the synchronous speed of the shaft, f_s is the stator frequency, and P_p is the number of pole pairs. Since the stator is connected to the power grid where voltages and currents have a fixed frequency (50 or 60 Hz), if the rotor speed N_r is changed, a power converter must be inserted between stator and grid. In this case, a Synchronous Generator (SG) with either rotor windings or permanent magnet excitation is most often used; the Wind Energy Conversion System (WECS)-based SG is shown in Figure 1.3. As can be noticed in this configuration, the power converter must be designed with the same power size of the machine as it needs to handle all power that the generator produces.

An alternative to the last configuration is represented by the Doubly Fed Induction Generator (DFIG), which allows the obtaining of a fixed output frequency as requested from the grid and a variable rotor speed behavior as well. The configuration of a WECS using a DFIG is shown in Figure 1.4, and the machine used is a well-known Wound Rotor Induction Machine (WRIM), where the windings on the rotor are taken out through terminals by using slip rings. The DFIG is then fed from the rotor side by a power converter whose size is dramatically reduced, if compared with the full-size converter used in the wind turbine configuration based on SGs. The DFIG principles, as well as its advantages and disadvantages, are explained in the following sections.

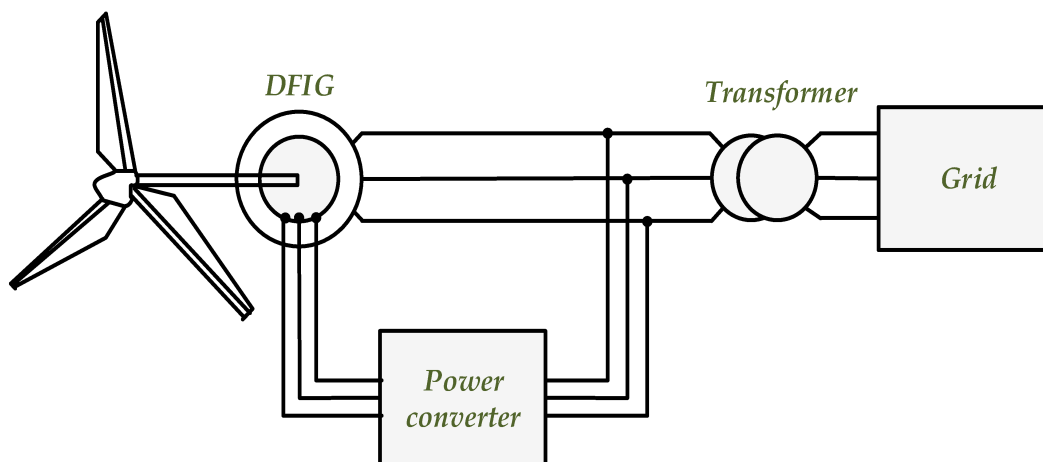


Figure. 1.4 Wind turbine configuration using Doubly Fed Induction Generators.

1.3 DFIG Principle and Advantages

In a SG, a static magnetic field is created by the DC currents that are injected into the rotor windings or created through permanent magnets. If a prime mover makes the rotor of the machine rotate, the static magnetic field rotates at the same speed of the rotor. In a DFIG, the rotor magnetic field is created by three-phase AC currents, instead of DC currents as in SG. Thus, the magnetic field produced by these currents is not static but rotates at a speed N_r , which is proportional to the frequency of the currents injected into the rotor windings. As a consequence, the stator rotating magnetic field, and thus the induced alternating voltage in the stator windings, is generated from the effect of the rotation of the generator rotor at a speed N_{mech} and the rotation of the rotor magnetic field at a speed N_r , produced by the AC currents fed into the rotor windings. In a wind turbine, the generator rotor always rotates in the same direction. Therefore, depending on the direction of the rotor magnetic field rotation, the

speeds N_{mech} and N_r are added or subtracted from each other [12]. From Equation 1.1, if the rotor magnetic field is considered, the following can be written:

$$f_s = P_p \cdot (N_r \pm N_{I_r}) \quad (1.2)$$

Where: f_r is the frequency of the currents that are injected into the rotor of the machine. From this equation, it can be understood that the purpose of keeping constant the stator frequency f_s can be achieved by adjusting the frequency of the AC rotor currents fed into the rotor, depending on the rotation speed of the generator rotor N_{mech} . Therefore, the natural fluctuations of the turbine speed are compensated for supplying the rotor in the proper way. As stated before, the main advantage of using a DFIG is that the power converter to control the machine is located on the rotor side. The power managed by the rotor is strictly dependent on the slip of the machine: If the rotor rotates slower or faster than the synchronous speed, the slip starts to increase, as does the power through the rotor. If the slip of the machine is limited to a small range of speeds above and below the synchronous speed, the same limitation is achieved in the power managed by the rotor. To cover the range of possible wind speeds, it has been found that the slip range should vary by about $\pm 30\%$ of the synchronous speed ω_s [12]. Thus, the rotor side converter can be designed for an active power of about 30% of the rated power of the machine. The other feature that makes this configuration particularly suitable for wind applications, is that the DFIG can generate power from its stator, at both sub-synchronous (rotor speed slower than synchronous speed), and hyper-synchronous (rotor speed faster than synchronous speed) modes. Accordingly, if the rotor rotates below synchronous speed, then power must be injected into the rotor to sustain generation; if the rotor rotates above synchronous speed, additional power is generated by the rotor. The exchanges of power at sub-synchronous and hyper-synchronous speed are allowed if a bidirectional converter is used on the rotor side. Typically, a back-to-back converter made of two three-phase converters sharing the DC link is used. In Figures 1.5 and 1.6, sub-synchronous and hyper-synchronous speed states of power exchange are presented respectively, where ω_m is the rotor rotational speed of the rotor flux.

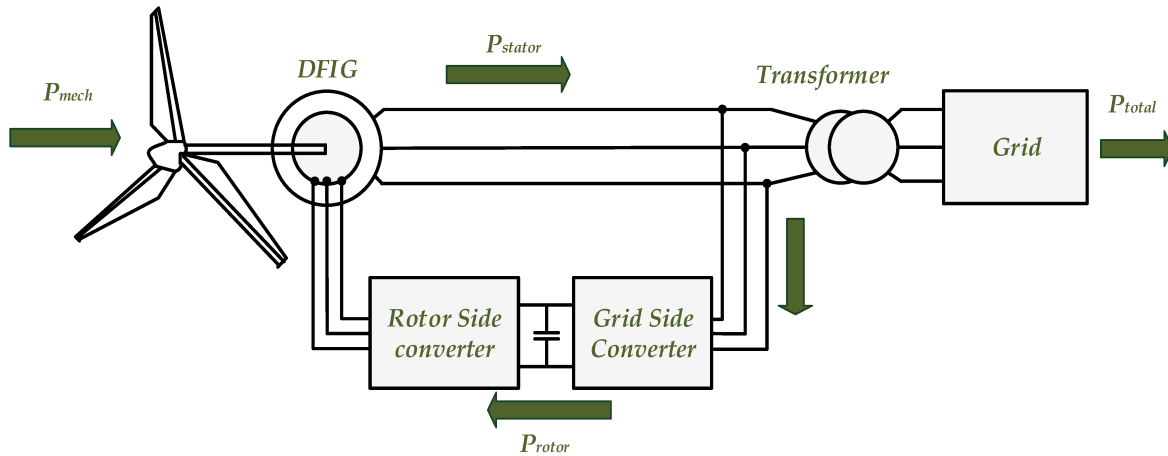


Figure 1.5 Sub-synchronous speed ($\omega_m < \omega_s$).

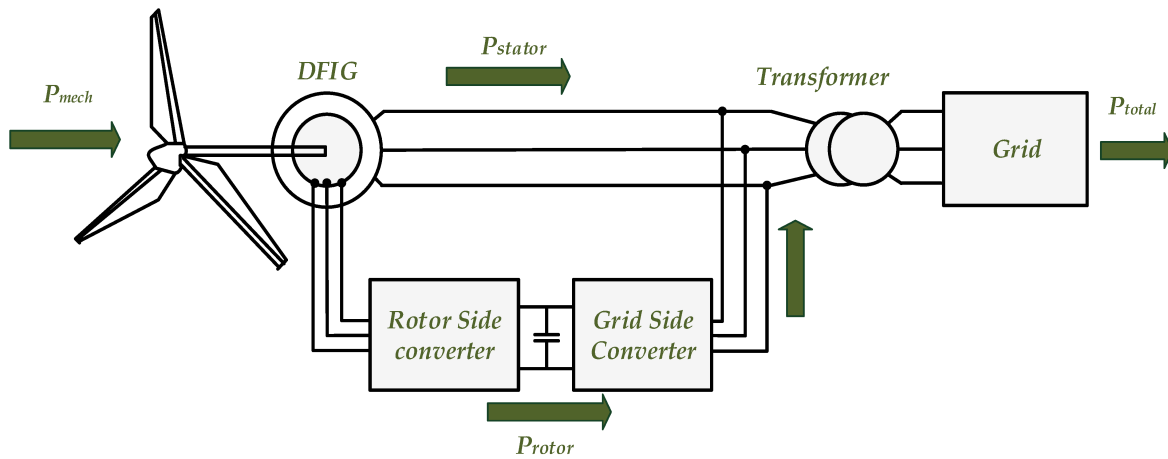


Figure 1.6 Hyper-synchronous speed ($\omega_m > \omega_s$).

1.4 Literature Review

Due to the rapid growth of wind energy in power systems, there are many studies that have investigated to understand the performance and behavior of wind power generation and its effect on the power system.

DFIG is a competitive choice for wind power generation due to its attractive factors when compared to other variable speed generators. Thus, it has been handled by many sources in the literature, such as in [12], a comprehensive study for DFIG including dynamic modeling, different control strategies, grid code requirements, voltage dips, and low voltage ride through (LVRT).

Different control topologies for DFIG based wind power have been discussed in literature, such as

the following: field-oriented control (FOC) [13, 14], high-order sliding mode (HOSM) [15–17], flux-oriented control [18], direct voltage control [19], direct torque control (DTC) [20–22], direct power control (DPC) [23–26], and fuzzy logic control [27–29]. Moreover, authors in [30] implemented a feedback linearization control technique and compared the results with the conventional FOC and V/f control.

As stated before, DTC is a common control strategy used for DFIGs-based wind power; it was first established in the 1980s by I. Takahashi [31] and M. Depenbrock [32]. Then, it became an alternative control algorithm for the classical FOC, developed and studied by many authors [2, 33–36] under different operating conditions. This control algorithm is discussed in detail in this dissertation, as well as the DPC scheme that was handled by [37–42].

The voltage dip for DFIG is an important topic in wind power generation due to the high sensitivity of DFIGs to grid disturbances. The DFIG system must remain connected during grid faults and support the grid with reactive power to fulfill grid codes.

A number of previous studies have discussed the possible solution of LVRT capability, [43–52] presented D-STATCOM based on a PID fuzzy controller to enhance the dynamic performance during the fault.

The authors found that by using this control scheme, the fluctuations of reactive power were reduced, leading to improvement in the LVRT performance. Moreover, the harmonics in the rotor current were reduced so the system was more stable, and thus also improving the LVRT stability.

Study [53] presented a comprehensive analysis of LVRT for DFIG based wind turbines. It described the DFIG dynamic modeling and implemented the transient characteristics of DFIGs, under symmetrical and asymmetrical grid voltage dip. It also provided a new rotor side control scheme for LVRT capability improvement during grid faults. This control scheme depends on the reduction of the rotor over voltage and current during grid unbalance conditions; without adding cost, this improved the LVRT capability and fulfilled the grid codes.

According to [54], the LVRT capability can be improved by using a nonlinear control based modified bridge-type fault current limiter (NC-MBFCL).

The study in [35] proposed and solved the problem of high rotor voltage during a voltage dip by magnetizing the DFIG from the stator circuit instead of the rotor circuit.

Another LVRT solution was presented in [55], a ‘virtual resistance demagnetization approach’ based on the dq control, and a reduction of switching losses was analyzed for a 2.1 MW DFIG system under

15%, 20%, 50%, and 80% voltage dip to meet the Indian grid-codes requirements.

This dissertation proposes different control algorithms for DFIG control. Conventional DTC is implemented and applied on the Rotor Side Converter (RSC) [56–59].

In addition to the conventional DTC method, improved DTC algorithms [60–65] are implemented, such as modified switching table DTC [20], and twelve sectors DTC [66–68]. Then, a comparison takes place according to torque, flux ripples, and current harmonics. Thus, a proposal can be put forth on a control technique that provides low ripples of torque and flux while also demonstrating better performance of DFIG during transient.

As stated before, because the DFIG-based wind energy conversion should fulfill special requirements during faults [69], it is important to study the LVRT effects on the grid connected DFIG [70, 71]. In this analysis, the effects of symmetrical and asymmetrical grid faults are analyzed, and the possible solutions to these effects are presented [72–79].

The aforementioned direct control methods are analyzed using MATLAB Simulink for a 2 MW DFIG, and the LVRT behavior of DFIG wind energy based is presented and discussed.

1.5 Thesis Layout

The aim of the thesis is to employ DTC for modern wind turbines to fulfill the revised grid requirements.

The parts of the dissertation are arranged as follows:

Chapter 2: The DFIG expressed in the ABC reference frame is first established, then the reference frames and two-axis transformation are explained.

Chapter 3: DTC strategy is applied to the (RSC) of DFIG. Then two DTC topologies are presented, in addition to the conventional method, and the results are compared. Finally, the DPC is presented, and the results are discussed.

Chapter 4: The grid side converter (GSC) vector control is described in detail, then the reference frame alignment and a grid filter are presented.

Chapter 5: Grid synchronization using direct virtual control is carried out, and the reference values of rotor flux and torque to achieve synchronization are calculated.

Chapter 6: Different types of grid faults (symmetrical and asymmetrical three-phase dip) are analyzed; the DFIG behavior is discussed. Further, the LVRT solutions to improve LVRT capability

are presented.

Chapter 7: Work conclusion, future work, and publications associated to this work are presented.

1.6 Chapter Conclusion

The development of wind power generation raised recently due to increased attention on environmental effects of conventional energy resources. There are different topologies of wind power generation were explained in this chapter, DFIG configuration was chosen in this analysis due to it's attractive advantages; good efficiency. The converter used with DFIG has low ratings and this will reduce the cost compared to the SG's.

Chapter 2

Dynamic Modeling of Doubly Fed

Induction Generator

For a better understanding of the DFIG performance as well as studying all the possible transient behaviors of it, this chapter introduces the machine model. First, the model in the three-phase reference frame is introduced. Then, using coordinate transformations, the dynamic model in the dq rotating reference frame is presented. This model is useful for the study of all important dynamic effects occurring during steady-state and transient operations. Hence, it should be valid for any time variation of the voltages or currents generated by the inverter that supplies the machine.

2.1 Doubly Fed Induction Machine Expressed in the ABC Reference Frame

According to the dynamic models of induction machines developed by many authors [80, 81] and as discussed in [12, 82, 83], the model of the DFIG is performed using some simplifications, which make it simpler compared to the real operation of the machine. In the idealized DFIG model, a WRIM with two symmetrical poles and three phase windings for both stator and rotor is considered. Figure 2.1 demonstrates the sectional view of the Wound Rotor Induction Machine (WRIM). As can be seen in the idealized machine, the stator windings (a, b, and c), as well as the rotor windings, are displaced from each other by 120 electrical degrees. The angle between the phase "as" of the stator and the phase "ar" of the rotor is called " θ_m ". Thus, the speed of the rotor can be calculated as follows:

$$\omega_m = d\theta_m/dt \quad (2.1)$$

Where the rotor windings are rotating in the counter clockwise direction. The relationship between the electrical and mechanical angle of the rotor depends on the number of pole pairs P_p as follows:

$$\omega_{mech} = \frac{\omega_m}{P_p} \quad (2.2)$$

Here, ω_{mech} is the rotor mechanical rotational speed.

As stated before, for simplicity, and according to [83], the following assumptions are used:

- Stator and rotor windings are symmetrically distributed; therefore, the resistances and the magnetizing and leakage inductances are equal for each phase.
- It will be considered only the sinusoidal component of the magnetomotive force in the air gap. In large generators, harmonic effects may be neglected due to the high number of slots.
- The magnetic saturation is neglected.
- The air gap is assumed constant.
- Skin effect in the stator and rotor phase winding conductors is neglected.

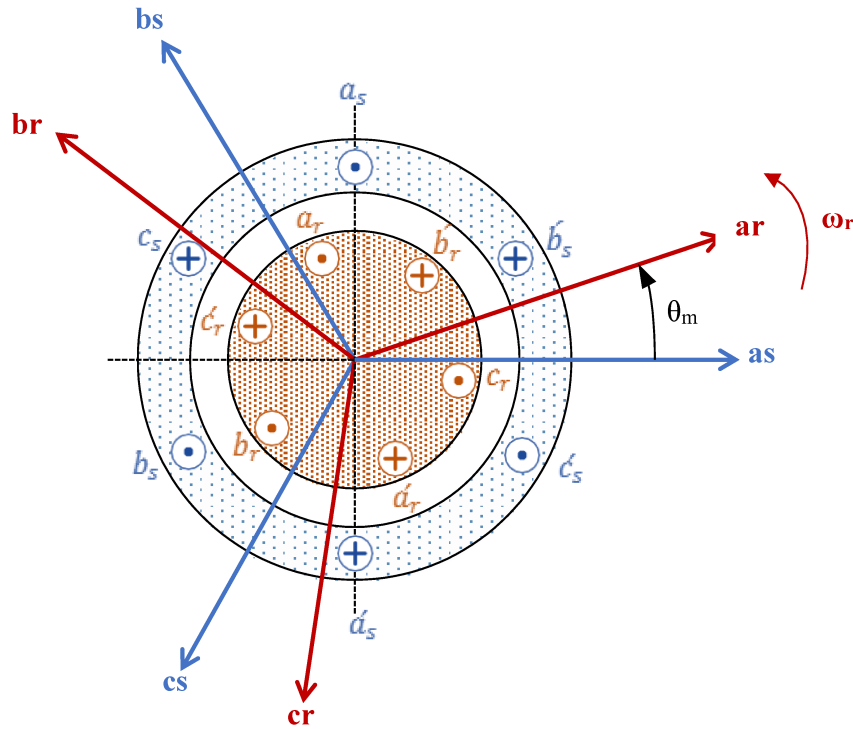


Figure. 2.1 Sectional view of the wound rotor induction machine.

Under these idealized assumptions, the electrical quantities for each stator winding can be described by the following equations [12]:

$$v_{as}(t) = R_s \cdot i_{as}(t) + \frac{d}{dt} \psi_{as}(t) \quad (2.3)$$

$$v_{bs}(t) = R_s \cdot i_{bs}(t) + \frac{d}{dt} \psi_{bs}(t) \quad (2.4)$$

$$v_{cs}(t) = R_s \cdot i_{cs}(t) + \frac{d}{dt} \psi_{cs}(t) \quad (2.5)$$

Where: $v_{as}(t)$, $v_{bs}(t)$, and $v_{cs}(t)$ are the stator voltages, $i_{as}(t)$, $i_{bs}(t)$, and $i_{cs}(t)$ are the stator currents, $\psi_{as}(t)$, $\psi_{bs}(t)$, and $\psi_{cs}(t)$ are the stator fluxes, R_s is the stator resistance.

In the same way, the rotor equations can be written as [12]:

$$v_{ar}(t) = R_r \cdot i_{ar}(t) + \frac{d}{dt} \psi_{ar}(t) \quad (2.6)$$

$$v_{br}(t) = R_r \cdot i_{br}(t) + \frac{d}{dt} \psi_{br}(t) \quad (2.7)$$

$$v_{cr}(t) = R_r \cdot i_{cr}(t) + \frac{d}{dt} \psi_{cr}(t) \quad (2.8)$$

Where: $v_{ar}(t)$, $v_{br}(t)$, and $v_{cr}(t)$ are the rotor voltages, $i_{ar}(t)$, $i_{br}(t)$, and $i_{cr}(t)$ are the rotor currents, $\psi_{ar}(t)$, $\psi_{br}(t)$, and $\psi_{cr}(t)$, are the rotor fluxes, R_r is the rotor resistance.

The resistances for both stator and rotor are supposed to be equal for each winding. Hence, the magnetic equations that relate the stator and rotor windings through the inductance coefficients and currents can be written as below:

$$\psi_{as} = L_{ls}i_{as} + L_{asas}i_{as} + L_{asbs}i_{bs} + L_{ascs}i_{cs} + L_{asar}i_{ar} + L_{asbr}i_{br} + L_{ascr}i_{cr} \quad (2.9)$$

$$\psi_{bs} = L_{ls}i_{bs} + L_{bsas}i_{as} + L_{bsbs}i_{bs} + L_{bscs}i_{cs} + L_{bsar}i_{ar} + L_{bsbr}i_{br} + L_{bscr}i_{cr} \quad (2.10)$$

$$\psi_{cs} = L_{ls}i_{cs} + L_{csas}i_{as} + L_{csbs}i_{bs} + L_{cscs}i_{cs} + L_{csar}i_{ar} + L_{csbr}i_{br} + L_{cscr}i_{cr} \quad (2.11)$$

In the same way, the three phases rotor fluxes are given by:

$$\psi_{ar} = L_{lr}i_{ar} + L_{arar}i_{ar} + L_{arbr}i_{br} + L_{arcr}i_{cr} + L_{aras}i_{as} + L_{arbs}i_{bs} + L_{arcs}i_{cs} \quad (2.12)$$

$$\Psi_{br} = L_{lr}i_{br} + L_{brar}i_{ar} + L_{brbr}i_{br} + L_{brcr}i_{cr} + L_{bras}i_{as} + L_{brbs}i_{bs} + L_{brcs}i_{cs} \quad (2.13)$$

$$\Psi_{cr} = L_{lr}i_{cr} + L_{crar}i_{ar} + L_{crbr}i_{br} + L_{crer}i_{cr} + L_{cras}i_{as} + L_{crbs}i_{bs} + L_{crce}i_{cs} \quad (2.14)$$

Here, L_{ls} and L_{lr} are the stator and rotor leakage inductances that should be equal for all stator and rotor phases. The value of each self-inductance and mutual-inductance can be calculated by using the principle of superposition, as the model has considered to be linear. Thus, the following equation can calculate the generic inductance:

$$L_{ij} = \frac{\Psi_{ij}}{i_j} \quad (2.15)$$

Note that Ψ_{ij} is the flux created by the current i_j and concatenated with the winding i [83].

From the geometries, it is clear that the inductances L_{asas} , L_{bsbs} , and L_{cses} are equal because the flux path for the three respective phases is identical. Moreover, these inductances are independent of the rotor position. Consequently, the following relationship is deduced:

$$L_{asas} = L_{bsbs} = L_{cses} = L_{ss} \quad (2.16)$$

The same considerations can be made for the mutual inductances between any two stator phases:

$$L_{asbs} = L_{bsas} = L_{ascs} = L_{csas} = L_{bscs} = L_{csbs} = -\frac{1}{2}L_{ss} = L_{sm} \quad (2.17)$$

Similarly, from the calculation of the rotor self-inductance and mutual-inductance coefficients, it can be noted that they are independent of the rotor position. Hence, their relationships can be written as:

$$L_{arar} = L_{brbr} = L_{crer} = L_{rr} \quad (2.18)$$

$$L_{arbr} = L_{brar} = L_{arcr} = L_{crar} = L_{brer} = L_{erbr} = -\frac{1}{2}L_{rr} = L_{rm} \quad (2.19)$$

Thus, with the model simplifications made before, only the mutual inductances between stator and rotor are dependent on the angular position of the rotor phase with respect to the stator phase windings.

From Figure 2.1, it can be deduced that all these coefficients vary with the rotor angular position θ_r with phase differences. As such, the inductances can be written as:

$$L_{asar} = L_{aras} = L_{bsbr} = L_{brbs} = L_{cscr} = L_{crCs} = L_{sr} \cos(\theta_r) \quad (2.20)$$

$$L_{asbr} = L_{bras} = L_{bscr} = L_{crbs} = L_{csar} = L_{arCs} = L_{sr} \cos(\theta_r + \frac{2}{3}\pi) \quad (2.21)$$

$$L_{ascr} = L_{cras} = L_{bsar} = L_{arbs} = L_{csbr} = L_{brCs} = L_{sr} \cos(\theta_r - \frac{2}{3}\pi) \quad (2.22)$$

Once the magnetic equations have been presented, by substituting all the fluxes expressions in the stator and rotor voltage equations, the model for a WRIM in the ABC reference frame can be achieved. This model can be written in a simplified matrix format as follows:

$$V_{abcs} = R_s \cdot I_{abcs} + \frac{d}{dt}(L_{abcSS} \cdot I_{abcs} + L_{abcSr} \cdot I_{abcr}) \quad (2.23)$$

$$V_{abcr} = R_r \cdot I_{abcr} + \frac{d}{dt}(L_{abcrr} \cdot I_{abcr} + L_{abcrs} \cdot I_{abcs}) \quad (2.24)$$

Here, V_{abcs} , I_{abcs} , V_{abcr} and I_{abcr} are the vectors representing the instantaneous values of voltages and currents for both stator and rotor respectively. Moreover, the resistance matrices are thus:

$$[R_s] = \begin{bmatrix} R_s & 0 & 0 \\ 0 & R_s & 0 \\ 0 & 0 & R_s \end{bmatrix}, \quad [R_r] = \begin{bmatrix} R_r & 0 & 0 \\ 0 & R_r & 0 \\ 0 & 0 & R_r \end{bmatrix} \quad (2.25)$$

The stator and rotor matrix of the self-inductances and mutual-inductances are as follows:

$$[L_{abcSS}] = \begin{bmatrix} L_{SS} + L_{Ls} & L_{sm} & L_{sm} \\ L_{sm} & L_{SS} + L_{Ls} & L_{sm} \\ L_{sm} & L_{sm} & L_{sm} + L_{SS} \end{bmatrix} \quad (2.26)$$

$$[L_{abcrr}] = \begin{bmatrix} L_{rr} + L_{lr} & L_{rm} & L_{rm} \\ L_{rm} & L_{rr} + L_{lr} & L_{rm} \\ L_{rm} & L_{rm} & L_{rr} + L_{lr} \end{bmatrix} \quad (2.27)$$

L_{ls} and L_{lr} are the leakage inductance of stator and rotor respectively. And finally, the mutual inductance coefficients between stator and rotor where $\theta_m = \theta_r$ is therefore:

$$[L_{abc sr}] = L_{sr} \begin{bmatrix} \cos(\theta_r) & \cos(\theta_r + \frac{2}{3}\pi) & \cos(\theta_r + \frac{4}{3}\pi) \\ \cos(\theta_r + \frac{4}{3}\pi) & \cos(\theta_r) & \cos(\theta_r + \frac{2}{3}\pi) \\ \cos(\theta_r + \frac{2}{3}\pi) & \cos(\theta_r + \frac{4}{3}\pi) & \cos(\theta_r) \end{bmatrix} \quad (2.28)$$

$$[L_{abc rs}] = L_{sr} \begin{bmatrix} \cos(\theta_r) & \cos(\theta_r + \frac{4}{3}\pi) & \cos(\theta_r + \frac{2}{3}\pi) \\ \cos(\theta_r + \frac{2}{3}\pi) & \cos(\theta_r) & \cos(\theta_r + \frac{4}{3}\pi) \\ \cos(\theta_r + \frac{4}{3}\pi) & \cos(\theta_r + \frac{2}{3}\pi) & \cos(\theta_r) \end{bmatrix} \quad (2.29)$$

From this model, it seems clearly that the dependence of the mutual inductances on the rotor angle, and hence on the time, would complicate the solution, because the inductance matrix would therefore need to be calculated at each time step. Thus, it has been well known that it is advantageous to seek a different approach [84, 85]. The different approach is based on the space vector representation of the electrical quantities, which allows the projection of the ABC components onto a pair of stationary axes, called the α - β axes. By expressing the model in this reference frame, the advantages of simplicity of formulation and implementation can be achieved. Moreover, if the frame of reference is rotated at the proper speed, the rotor angle dependence can be eliminated, and the inductances will appear as constants. For this purpose, the rotational transformation in the dq axes are presented. It is more convenient to separate these two steps, as explained in the next sections.

2.2 Reference Frames and the Two-Axis Transformation

As stated in the previous section, the transformation of the electrical equations into a two-phase reference frame allows us to obtain a simpler model than the three-phase one. To achieve this simplified model, the space vector theory is initially mentioned, then, the dynamic models are achieved.

2.2.1 Space Vector Representation

In this work, space vectors are used to represent voltages, fluxes, and currents, in both stator and rotor windings. Considering the three phase voltages $v_a(t)$; $v_b(t)$ and $v_c(t)$ as a balanced set, it can be written that:

$$v_a(t) = V \cdot \cos(\omega t + \phi) \quad (2.30)$$

$$v_b(t) = V \cdot \cos\left(\omega t + \phi - \frac{2\pi}{3}\right) \quad (2.31)$$

$$v_c(t) = V \cdot \cos\left(\omega t + \phi - \frac{4\pi}{3}\right) \quad (2.32)$$

This balanced three-phase system can be represented in a plane, as a space vector \vec{v} that rotates at ω angular speed across the origin of the three axes \vec{a} , \vec{b} , and \vec{c} shifted by 120 degrees. Therefore, by taking the \vec{a} axis as reference, the space vector components along each phase axis are mathematically as follows:

$$\vec{v}_a = v_a(t) \cdot e^{j0} \quad (2.33)$$

$$\vec{v}_b = v_b(t) \cdot e^{j2\pi/3} \quad (2.34)$$

$$\vec{v}_c = v_c(t) \cdot e^{j4\pi/3} \quad (2.35)$$

Thus, the space vector ('Clarke Transformation') can be found by adding the contribute of each phase:

$$\vec{v}_{abc} = \vec{v}_a + \vec{v}_b + \vec{v}_c = v_a(t) \cdot e^{j0} + v_b(t) \cdot e^{j2\pi/3} + v_c(t) \cdot e^{j4\pi/3} \quad (2.36)$$

Examining the space vector notation, it can be seen that the contributions from three axes can be represented with just two magnitudes in the real-imaginary complex plane $\vec{v}_{\alpha\beta}$, which can be expressed as:

$$\vec{v}_{\alpha\beta} = v_\alpha + jv_\beta = \frac{2}{3} \left(v_a(t) \cdot e^{j0} + v_b(t) \cdot e^{j2\pi/3} + v_c(t) \cdot e^{j4\pi/3} \right) \quad (2.37)$$

The factor $2/3$ is inserted in order to adjust the amplitude of $\vec{v}_{\alpha\beta}$ to the one of the original sinusoidal 3 phase voltages. The $\alpha\beta$ magnitudes can be calculated in an easier way from the last equation:

$$v_\alpha = \text{Re}(\vec{v}_{\alpha\beta}) \quad (2.38)$$

$$v_\beta = \text{Im}(\vec{v}_{\alpha\beta}) \quad (2.39)$$

2.2.2 DFIG Model Expressed in the $\alpha\beta$ Reference Frame

In the previous section, the relationship between the $\alpha\beta$ and abc magnitudes was presented. In this section, the DFIG model in the $\alpha\beta$ reference frame is discussed. Using equations (2.3)-(2.5) for stator and rotor in $\alpha\beta$ reference frame, the following expressions are thus achieved:

$$\vec{v}_{\alpha\beta s}^s = R_s \cdot \vec{i}_{\alpha\beta s}^s + \frac{d}{dt} \vec{\psi}_{\alpha\beta s}^s \quad (2.40)$$

$$\vec{v}_{\alpha\beta r}^r = R_r \cdot \vec{i}_{\alpha\beta r}^r + \frac{d}{dt} \vec{\psi}_{\alpha\beta r}^r \quad (2.41)$$

Note that the superscripts "s" and "r" are indicating that the space vectors are referring to the stator and rotor reference frames, respectively. Hence, in the stator voltage equation, the voltage, current, and flux refer to the stator and similarity in the rotor equation. Next, the relationship between the

current and flux linkage is provided as:

$$\vec{\Psi}_{\alpha\beta s}^s = L_s \cdot \vec{i}_{\alpha\beta s}^s + L_{sr} \cdot \vec{i}_{\alpha\beta r}^s, \quad \text{with: } L_s = L_{ss} + L_{ls} \quad (2.42)$$

$$\vec{\Psi}_{\alpha\beta r}^r = L_{sr} \cdot \vec{i}_{\alpha\beta s}^r + L_r \cdot \vec{i}_{\alpha\beta r}^r, \quad \text{with: } L_r = L_{rr} + L_{lr} \quad (2.43)$$

As written in the earlier section, the rotor position dependence needs to be eliminated. Moreover, for implementation purposes, all the equations must be written in the same reference frame. Thus, once these equations have been obtained, it is convenient to use a different reference frame, rotating with speed that helps us for the studies of the DFIG. This transformation, also known as 'Park Transformation', changes the reference frame from the stationary $\alpha\beta$ to dq , it is introduced in the following section.

2.2.3 DFIG Model Expressed in the dq Reference Frame

There are three different preferred reference frames used in d and q axes calculations for induction machines simulation. Figure 2.2 shows the space vectors in the three reference frames, these frames can be classified according to the d and q axes rotation speed [12]:

- Stationary reference frame $\alpha\beta$ (known as the stator reference frame): The rotational speed is zero.
- Synchronous reference frame DQ : the D and Q axes rotate at the rotational speed ω_s of the stator flux or stator voltage.
- Rotor reference frame dq : The d and q axes rotate at the rotor speed ω_m .

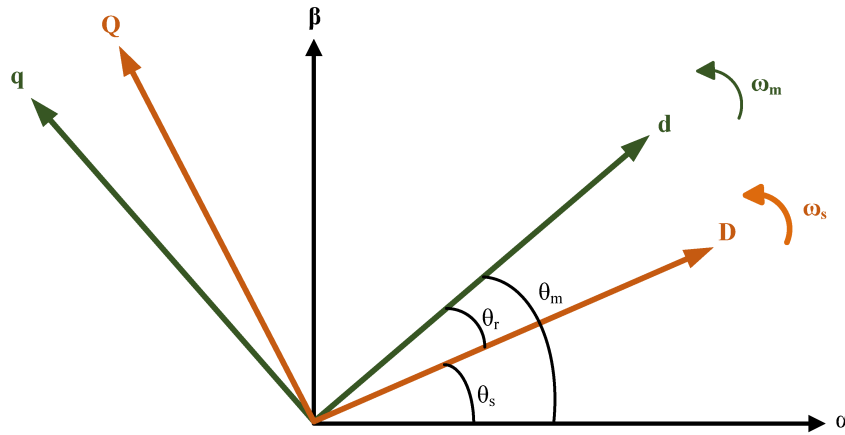


Figure. 2.2 The space vectors in the three reference frames.

Choosing the reference frame depends on the problem that needs to be studied. The stationary reference frame is used for the stator transient's investigation, while the synchronous reference frame is most suitable for the controller's stability, and the rotor reference frame is commonly used for the rotor variables study, in which there is no need to use the inverse Park's transformations to calculate the actual rotor current [80]. In this analysis, because the rotor transients are important for the direct control of induction machine, the rotor reference frame is used. Any dq reference frame can be obtained using the complex notations by multiplying the stator and rotor equations (2.40)-(2.43) respectively by $e^{j\theta}$ and $e^{-j(\theta-\theta_m)}$, where θ refers to the chosen reference frame and θ_m is the rotor electrical angular position. Thus, depending on the last definition of the reference frames the electrical equations in a generic reference frame (with $\omega = d\theta/dt$) can be written as:

$$\begin{cases} v_{sq}^a = R_s \cdot i_{sq}^a + \frac{d}{dt} \psi_{sq}^a + \omega \psi_{sd}^a \\ v_{rd}^a = R_r \cdot i_{rd}^a + \frac{d}{dt} \psi_{rd}^a - (\omega - \omega_m) \psi_{rq}^a \\ v_{rq}^a = R_r \cdot i_{rq}^a + \frac{d}{dt} \psi_{rq}^a + (\omega - \omega_m) \psi_{rd}^a \end{cases} \quad (2.44)$$

And the flux linkages can be replaced with currents and inductances as:

$$\begin{cases} \psi_{sd}^a = L_s \cdot i_{sd}^a + L_{sr} i_{rd}^a \\ \psi_{sq}^a = L_s \cdot i_{sq}^a + L_{sr} i_{rq}^a \\ \psi_{rd}^a = L_r \cdot i_{rd}^a + L_{sr} i_{sd}^a \\ \psi_{rq}^a = L_r \cdot i_{rq}^a + L_{sr} i_{sq}^a \end{cases} \quad (2.45)$$

Here, "a" stands for arbitrary reference frame, depending on the reference angle which is chosen ($\omega = d\alpha/dt = 0$, $\omega = \omega_m$, or $\omega = \omega_s$). The superscripts "0", "r" and "s" represent stationary, rotor and synchronous reference frame respectively.

2.2.4 Power and Torque in dq Reference Frame

Once voltages, currents, and fluxes have been projected in the d and q axes, torque and power must be calculated to complete the dynamic model. Electromagnetic torque is the link between electrical and mechanical systems. Physically, the torque is generated by the forces present when the conductor current passes through a magnetic field. Then, as the torque does not depend on the reference frame, it can be expressed by using the space vectors with the superscript 'a', which indicates the arbitrary reference frame. Thus, the torque can be expressed as [12]:

$$T_{em} = \frac{3}{2} p \frac{L_{sr}}{L_s} \text{Im}(\vec{\psi}_s^a \cdot \vec{i}_r^{a*}) = \frac{3}{2} p \frac{L_{sr}}{L_s} (\psi_{sq}^a i_{rd}^a - \psi_{sd}^a i_{rq}^a) \quad (2.46)$$

Here, the $3/2$ is due to the transformation, and it is necessary for the power equivalence between the two axis and three axis systems. Some other equivalent expression can be obtained for the torque by substituting the current or flux expressions in (2.46).

Finally, to complete the model, it is necessary to compute the active and reactive powers for both stator and rotor, by using the space vector notation in the general reference frame. Those expressions are thus:

$$P_s = \frac{3}{2} \text{Re}(\vec{v}_s^a \cdot \vec{i}_s^{a*}) = \frac{3}{2} (v_{sd}^a i_{sd}^a + v_{sq}^a i_{sq}^a) \quad (2.47)$$

$$Q_s = \frac{3}{2} \text{Im}(\vec{v}_s^a \cdot \vec{i}_s^a) = \frac{3}{2} (v_{sq}^a i_{sd}^a - v_{sd}^a i_{sq}^a) \quad (2.48)$$

$$P_r = \frac{3}{2} \text{Re}(\vec{v}_r^a \cdot \vec{i}_r^a) = \frac{3}{2} (v_{rd}^a i_{rd}^a + v_{rq}^a i_{rq}^a) \quad (2.49)$$

$$Q_r = \frac{3}{2} \text{Im}(\vec{v}_r^a \cdot \vec{i}_r^a) = \frac{3}{2} (v_{rq}^a i_{rd}^a - v_{rd}^a i_{rq}^a) \quad (2.50)$$

2.2.5 The Mechanical Subsystem

By applying the fundamental dynamic equation to the rotor of the machine, the relationship between acceleration and torque balance can be written as follows:

$$T_{em} - T_{load} = J \frac{d\omega_{mech}}{dt} \quad (2.51)$$

Thus, T_{load} is the torque on the shaft originating from the mechanical input, ω_{mech} is the mechanical speed, J is the inertia on the shaft*. The convention is that a positive T_{em} and T_{load} correspond to the motoring mode and a negative T_{em} and T_{load} correspond to a generating mode. Either way, these torques are always in opposition to each other. This model is used for a wind turbine, which is always made to spin in the same direction, assumed to be counter-clockwise. In summary, it can be said for steady state:

- Motoring: $T_{em} > 0$, $T_{load} > 0$ (both in counter-clockwise sense), $\omega_{mech} > 0$.
- Generating: $T_{em} < 0$, $T_{load} < 0$ (both in clockwise sense), $\omega_{mech} > 0$.

* Assumption: all mechanical inertias are concentrated in one value (single mass oscillator).

2.3 Chapter Conclusion

The dynamic modeling of DFIG is the basic step for working on grid connected DFIG. In this chapter the DFIG model in three-phase reference frame was introduced, along with ABC space vector representation, $\alpha\beta$ reference frame, and the dq rotating reference frame which was presented using the coordinate transformations.

Chapter 3

Rotor Side Converter Control

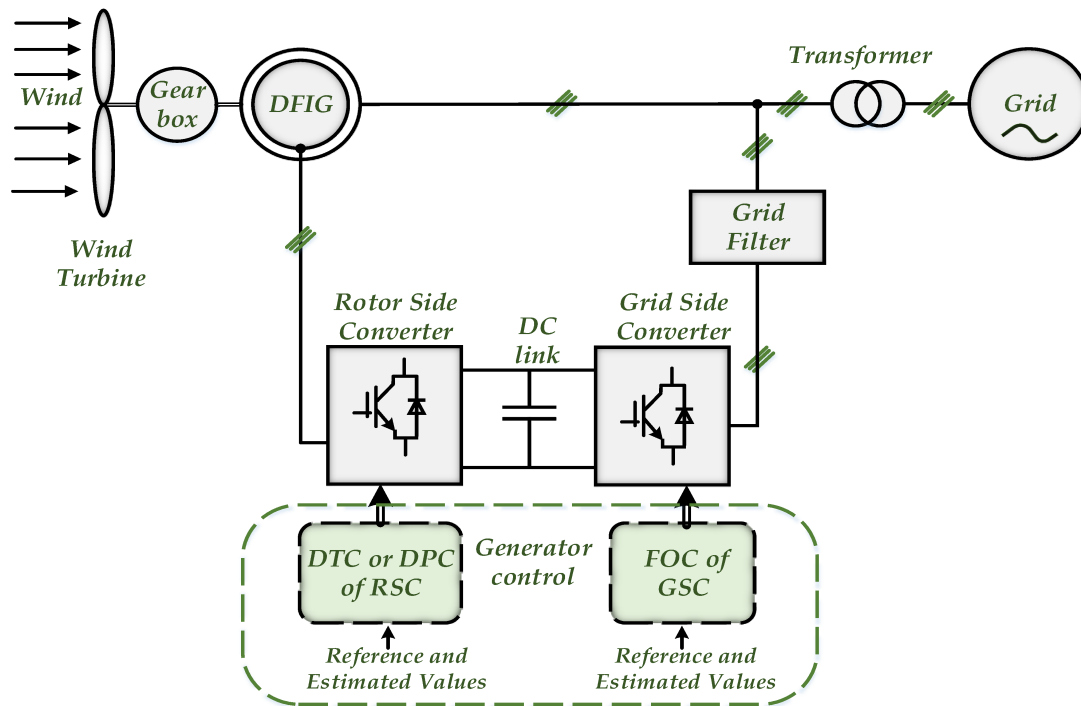


Figure. 3.1 DFIG system based wind power generation.

The DFIG system for wind power generation as in Figure 3.1 consists of the following:

- DFIG connected to the wind turbine through a gear box.
- Back-to-back converter with its control: RSC (Rotor Side Control) and GSC (Grid Side Control).
- Grid filter connected to GSC output.
- Transformer.
- The grid.

Most of the control strategies that have been used to control the DFIG's are based on FOC (Field Oriented Control or Vector Control); this control scheme requires complex computational tasks and very accurate values for the machine parameters. And such, this requirement may lead to an inaccuracy when operating under grid disturbances.

Direct control techniques (DTC and DPC) can overcome these drawbacks with their reduction of computations and the simplified control algorithm, which does not require coordinate transformations. More details are discussed later.

In this chapter, the DTC is presented in detail, then several possible techniques that improve the switching table of DTC are presented. Further, the DPC is also explained. Including these sections, some simulations carried out with MATLAB/Simulink are shown in order to demonstrate the performances and feasibility of these algorithms.

3.1 Direct Torque Control for DFIG

DTC is a popular direct control strategy of the three phase drive system; the torque and the rotor flux are controlled using the hysteresis controllers and a switching table for choosing the voltage vectors [2, 31–33, 56–58].

DTC is an effective alternative technique for the vector control mainly according to the control variables that are used in both algorithms. In DTC, the electromagnetic torque and the rotor flux of the machine are used as primary control variables, but in the FOC the q and d components of the stator current control the active and reactive power of the stator when the stator reference frame is used [12].

The advantages and features of DTC over FOC can be summarized according to [20–22] as:

- Fast torque response.
- Minimized dependency on machine parameters.
- Reducing the complexity of vector control algorithm, the modulation technique and PID controllers are not needed, which reduces the effort on the controllers.
- The coordinate transformations are not required.
- Simplicity and reliability.

Thus, with DTC, there is no need for separate voltage and frequency modulators, which cause an additional delay time of torque and speed response. Conventional DTC is discussed in this section; the DTC technique is based on the direct regulation of the electromagnetic torque and the rotor flux. Modifying (2.46), the electromagnetic torque can be expressed as a function of the rotor flux, the stator flux, and the angle δ between them:

$$T_{em} = \frac{3}{2} p \frac{L_{sr}}{\sigma L_s L_r} |\vec{\psi}_s| \cdot |\vec{\psi}_r| \cdot \sin \delta \quad (3.1)$$

Where σ is the leakage factor and given by:

$$\sigma = 1 - \frac{L_{sr}^2}{L_s L_r}$$

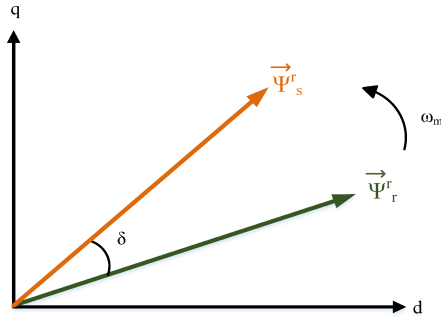


Figure. 3.2 Flux vectors diagram in rotor reference frame.

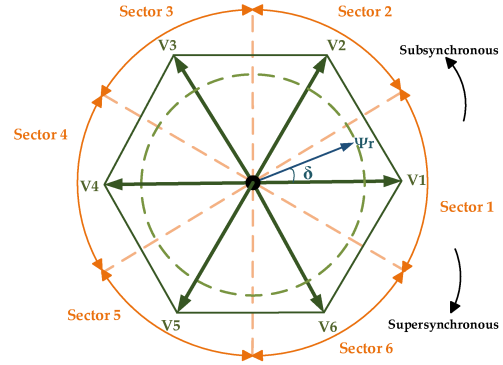


Figure. 3.3 Space vector representation of voltage vectors.

Table 3.1 Voltage vectors selection table, where (1,-1, and 0): denote increasing, decreasing, and constant torque and flux variables. (k-1): the previous sector, (k+1): the next sector.

$H\psi_r$	HT_{em}	Voltage Vector
	1	V(k-1)
1	0	V(0,7)
	-1	V(k+1)
	1	V(k-2)
-1	0	V(0,7)
	-1	V(k+2)

In this analysis, as the aim of direct control strategy is the control of torque, the torque expression should be analyzed in detail. The variables that can influence the torque behavior are as follows [12]:

- Stator flux (ψ_s): because the stator of the machine is directly connected to the grid, the stator flux is established according to the network voltage and frequency. Hence, the stator flux space vector can be assumed with constant amplitude and rotating speed.
- Rotor flux (ψ_r) and angle (δ): As a consequence of the stator flux behavior, if the rotor flux space vector is created with the same angular speed as the stator flux, then by

controlling the angle the desired torque can be achieved.

The vector diagram of the rotor and stator fluxes expressed in the rotor reference frame is shown in Figure 3.2, and the hexagon voltage vectors are shown in Figure 3.3.

From section 2.2.3, the rotor voltage expression in the rotor reference frame assumes the following form:

$$\vec{v}_r = R_r \cdot \vec{i}_r + \frac{d}{dt} \vec{\psi}_r \quad (3.2)$$

Here, if the voltage drop in the rotor resistance is neglected, it yields to a direct dependence between rotor voltage and rotor flux derivative:

$$\vec{v}_r \simeq \frac{d}{dt} \vec{\psi}_r \quad (3.3)$$

Taking into account the rotor voltage in the above equation, it can be written as:

$$\vec{\psi}_r = \int_0^t \vec{v}_r dt \quad (3.4)$$

From the last expression, it is easy to understand that by imposing the right rotor voltage for each time interval (Δt), it is possible to manipulate the rotor flux, and thus the electromagnetic torque is selected as a result of equation (3.1). If the rotor is fed by a two-level voltage source converter, the eight different voltages that can be applied to the machine are: V1, V2, V3, V4, V5, V6 and the zero vectors V0 and V7. Hence, the way to impose the desired rotor flux is achieved by choosing the most suitable state of the Voltage Source Converter (VSC). Depending on the position of the rotor flux, each inverter state corresponds to a different behavior of torque and rotor flux. Thus, by injecting different rotor voltages, the rotor flux follows a nearly circular trajectory beyond the stator flux, as shown in Figure 3.4. Repeating a large sequence of possible voltage injections in each sector, it can become a switching table, which permits the selection of the appropriated inverter voltage vector to be applied to the converter on the basis of rotor flux and electromagnetic torque errors. The errors are obtained by comparing the estimated and reference values of flux and torque. The possible combination of the voltage vectors is shown in Table 3.1, where k indicates the number of the sector in which the flux is located. Four active voltage vectors can be injected in each sector (e.g. V6, V2, V5, and V3 when the rotor flux space vector in sector 1). As an example, if $\vec{\psi}_r$ in sector 6, $H\psi_r = -1$, and $HT_{em} = -1$,

then, using Table 3.1 the voltage vector is $V(k+2)$ that is the following second sector after the current sector, thus, $V(k+2)=V2$.

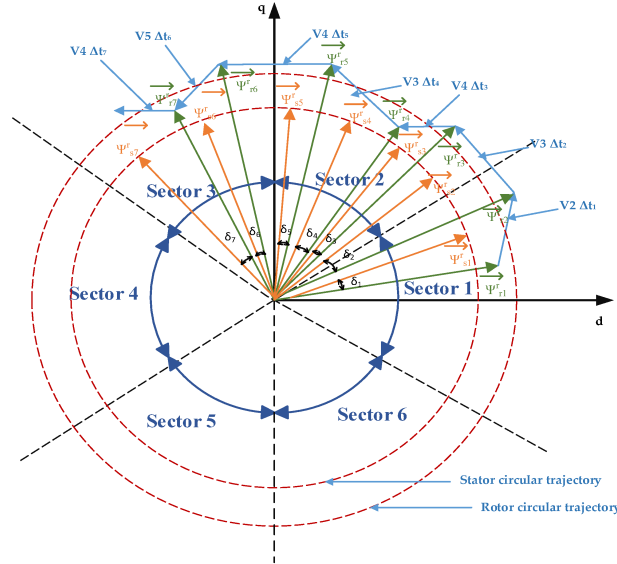


Figure. 3.4 Rotor and stator flux trajectory in first three sectors with the active voltage vectors.

3.1.1 DTC Implementation

The block diagram of DTC is shown in Figure 3.5. The DTC technique can be summarized into the following steps:

- Electromagnetic torque and rotor flux estimation.
- Torque reference determination according to wind and rotor speed.
- Desired rotor flux evaluation.
- Comparison between reference and estimated values.
- Torque and flux errors (eT_{em} , $e\psi_r$) elaboration through torque and flux hysteresis controllers.
- Rotor voltage vector selection from torque error, rotor flux error, and the rotor flux position.
- Switching frequency limitation.

In the following sections, each step corresponding to the blocks in the diagram is explained.

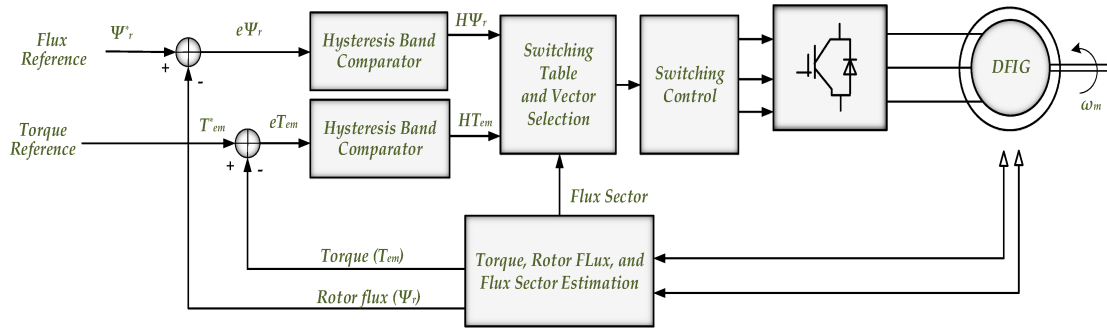


Figure 3.5 Conventional DTC scheme for DFIG.

3.1.2 Electromagnetic Torque and Rotor Flux Estimation

The electromagnetic torque and rotor flux can be estimated by using either currents or voltages of rotor and stator. Using voltages in calculations requires the use of integration and thus requires a high numerical accuracy and proper initialization of initial values. Moreover, because the rotor voltage has low fundamental frequency, the integrators may have a not satisfactory behavior, due to the possible difference between the actual value of R_r and the value used in calculations, because of the uncertainty and large fluctuations of the rotor resistance value during operation, which can cause the integrators to saturate [59, 86].

In this analysis, to avoid using integrators, the rotor and stator currents are used to estimate torque (T_{em}) and rotor flux (ψ_r). Substituting the rotor and stator flux from (2.45) in (2.46), the electromagnetic torque can be expressed as:

$$T_{em} = \frac{3}{2} p L_{sr} (i_{sq}^r i_{rd}^r - i_{sd}^r i_{rq}^r) \quad (3.5)$$

The position of the rotor flux space vectors determine in which sector the flux lies. The flux phase θ_{ψ_r} is the phase angle of ψ_r^r . Then, the flux position can be determined using Table 3.2.

Table 3.2 Sector division for the flux position determination

Sector Number	Flux Angle θ_{ψ_r}
1	$-30^\circ < \theta_{\psi_r} < 30^\circ$
2	$30^\circ < \theta_{\psi_r} < 90^\circ$
3	$90^\circ < \theta_{\psi_r} < 150^\circ$
4	$150^\circ < \theta_{\psi_r} < 210^\circ$
5	$210^\circ < \theta_{\psi_r} < 270^\circ$
6	$270^\circ < \theta_{\psi_r} < 330^\circ$

3.1.3 Electromagnetic Torque and Rotor Flux Reference Values Determination

Electromagnetic Torque Reference The conventional scheme used to perform the reference value of the torque is a speed controller using PI control algorithm, but in this study, the speed is assumed to be constant. The torque reference is a time step function to study different levels of machine torque, as well as generating and motoring modes to prove the system reliability and flexibility on different conditions. Motoring operation can occur in case of modern increased inertia simulation.

Rotor Flux Reference Since a wind turbine should follow specific codes related to the power generation, the rotor flux reference can be replaced with a power reference [12]. This goal can be achieved by manipulating the machine equations introduced in Section 2.2. The result is represented by the following [12, 87]:

$$|\vec{\psi}_r^*| = \sqrt{\left(k_1 |\vec{\psi}_s| + k_2 \frac{Q_{sref}}{|\vec{\psi}_s|}\right)^2 + \left(k_3 \frac{T_{em}^*}{|\vec{\psi}_s|}\right)^2} \quad (3.6)$$

Where:

$$k_1 = \frac{\sigma}{L_r} L_{sr} + \frac{L_{sr}}{L_s}, \quad k_2 = \frac{-\sigma L_r L_s}{1.5 \omega_s L_{sr}}, \quad k_3 = \frac{-\sigma L_r L_s}{1.5 p L_{sr}}$$

The electromagnetic torque is already known from the previous section, and the stator flux can be obtained from the stator voltage expression if the resistive drop is neglected:

$$|\vec{\psi}_s| \approx \frac{|\vec{v}_s|}{\omega_s} \quad (3.7)$$

3.1.4 Hysteresis Controllers and Rotor Voltage Vector Selection

The estimated and reference values are compared, then the resulting error is delivered to two hysteresis controllers, as shown before in Figure 3.5: one for the electromagnetic torque and one for the rotor flux. A three-level hysteresis comparator is used for the torque, and a two-level hysteresis comparator is used for the flux, as shown in Figure 3.6. As can be noted, the output of the torque controller is represented by a variable HT, which indicates directly if the amplitude of the torque must be increased (HT = 1), decreased (HT = -1), or kept constant (HT = 0), depending on the input.

The conditions of the torque comparator are given as (with T_{em}^* is the torque reference value):

$$HT_{em} = 1, \quad for: \quad (T_{em}^* - T_{em}) \geq HB_T/2 \quad (3.8)$$

$$HT_{em} = -1, \quad for: \quad (T_{em}^* - T_{em}) \leq -HB_T/2 \quad (3.9)$$

$$HT_{em} = 0, \quad for: \quad -HB_T/2 \leq (T_{em}^* - T_{em}) \leq HB_T/2 \quad (3.10)$$

Here, HT_{em} and HB_T are the torque status signal and the hysteresis band of the torque and T_{em}^* is the torque reference value. A similar scheme is used with the rotor flux; the error obtained serves as an input of the two-level hysteresis comparator. If the error is positive $H\psi_r = 1$; the flux magnitude should be increased, and when the error is negative $H\psi_r = -1$, the magnitude of flux should be decreased. The conditions of the flux comparator are given as follows (with ψ_r^* is the rotor flux reference value):

$$H\psi_r = 1, \quad for: \quad |\psi_r^*| - |\psi_r| \geq HB_\psi/2 \quad (3.11)$$

$$H\psi_r = -1, \quad for: \quad |\psi_r^*| - |\psi_r| \leq -HB_\psi/2 \quad (3.12)$$

Thus, $H\psi_r$ and $HB\psi_r$ are the flux status signal and the hysteresis band of the flux and ψ_r^* is the flux reference value.

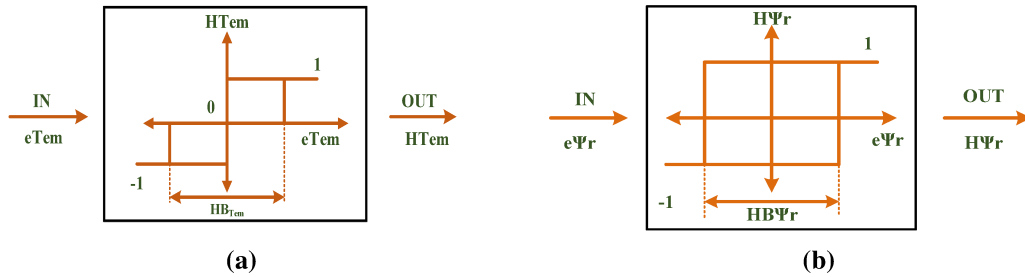


Figure. 3.6 a) Three-level hysteresis comparator for torque control, b) Two-level hysteresis comparator for flux control.

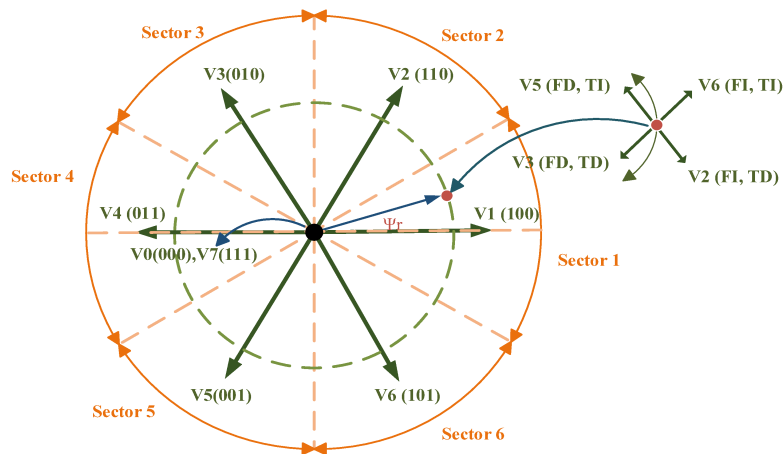


Figure. 3.7 Voltage vectors in conventional DTC scheme, with: TI, TD and FI, FD: Increase and Decrease of Torque and Flux.

The voltage vector plane is divided into six sectors as illustrated in Figure 3.7. An example of a rotor flux in the first sector region is also shown. The sector is calculated from the rotor flux angle, which determines the current rotor flux vector position, and the voltage vector is selected from the switching table shown in Table 3.3.

Table 3.3 Voltage vectors in conventional DTC scheme, with: TI, TD and FI, FD: Increase and Decrease of Torque and Flux.

Number of Sector		1	2	3	4	5	6
$H\psi_r$	HT_{em}						
	1	V6	V1	V2	V3	V4	V5
1	0	V7	V0	V7	V0	V7	V0
	-1	V2	V3	V4	V5	V6	V1
	1	V5	V6	V1	V2	V3	V4
-1	0	V0	V7	V0	V7	V0	V7
	-1	V3	V4	V5	V6	V1	V2

3.1.5 Switching Control

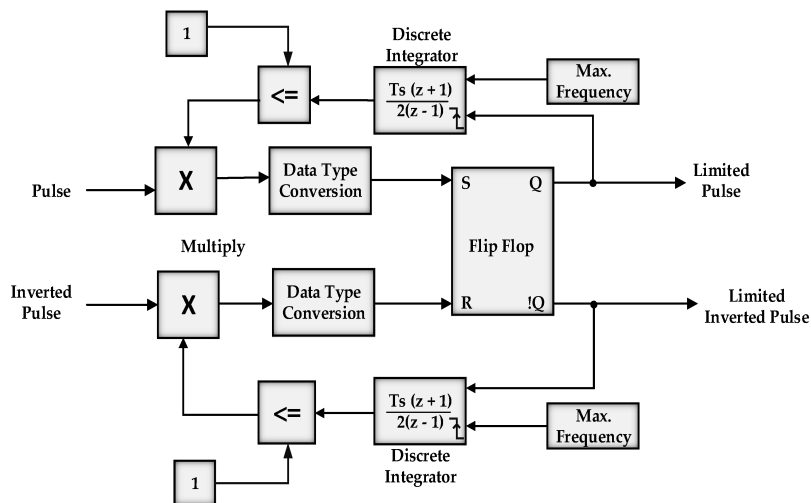


Figure. 3.8 Switching frequency limiter.

The switching frequency of DTC is variable due to the use of hysteresis band controllers of torque and flux. Higher switching frequency is preferable because it reduces the harmonics of torque, flux, and stator current. However, it also leads to an increase of the semiconductors switching losses, which results in increasing cost of semiconductors.

Thus, it is necessary to limit the switching frequency. The switching control block [88], which can be

seen in Figure 3.5, is used for this purpose. It is placed after the switching table and vector selection, the main purpose of this block is to limit the switching frequency, so that it does not exceed a limit, which has to be defined. Figure 3.19 shows the block diagram of the switching frequency limitation, a predefined maximum switching frequency is used to limit the output pulses frequency. A feed back signal from the limited pulse performs the external reset of discrete integer, after integration the output of integrator is compared with a constant 1 to multiply it with the input pulse. Thus, the result is subjected to a S-R flip-flop through a data conversion block. The flip-flop records the over-flow status, for the input signal.

3.2 DTC Improvement

As well as the advantages of DTC that were handled in the previous section, there are some drawbacks that affect system reliability and performance. Much of the literature discuss these drawbacks and suggest several possibilities for improvement [60–65]. The disadvantages of DTC can be summarized as:

- Problems during starting.
- Variable switching frequency that leads to undefined semiconductors switching losses.
- Problems in torque and flux at low speed values.
- Ripples in electromagnetic torque, current, and flux.
- Effect on torque and flux estimation due to resistances, voltage and current measurement variation.
- The desired torque is satisfied for only a few switching points as two voltage vectors are visible in each sector.

In this section, three different DTC techniques are used to overcome these drawbacks. The simulation results are discussed and compared with conventional DTC.

3.2.1 Twelve Sectors DTC

One of the disadvantages of the conventional DTC algorithm is the use of six non-zero voltage vectors by the VSC, as the desired torque is satisfied for only few switching points, and most voltage vectors introduce a torque that is either greater or less than the desired torque [66–68]. In addition, each sector in the conventional DTC has two states, which present torque ambiguity, and they are not used;

it can be noted from Table 3.3 that the voltage vectors V1 and V4 do not appear in the first sector. The same thing for the other sectors with different voltage vectors; this will lead to an uncertainty in the flux and torque within a 60 degree sector. Moreover, large and small errors in torque and flux cannot be distinguished in classical DTC because the same voltage vectors are used during different operating conditions [68, 67].

These drawbacks can be solved by using the 12-sector DTC technique. In this control strategy, all voltage vectors are used in all twelve sectors, as can be seen in Table 3.4. The switching is therefore more accurate; the voltage vector plane is divided into twelve sectors instead of six. The rotor flux locus is illustrated in Figure 3.9, where: TI,TD ($HT_{em}=2,-2$) is a large increase and decrease of torque, FI,FD ($H\psi_r=1,-1$) is an increase and decrease of flux, and TsI,TsD ($HT_{em}=1,-1$) is a small increase and decrease of torque.

Table 3.4 Switching table for the twelve sector DTC.

Sector Number		1	2	3	4	5	6	7	8	9	10	11	12
$H\psi_r$	HT_{em}												
1	2	V2	V3	V3	V4	V4	V5	V5	V6	V6	V1	V1	V2
	1	V2	V2	V3	V3	V4	V4	V5	V5	V6	V6	V1	V1
	-1	V1	V1	V2	V2	V3	V3	V4	V4	V5	V5	V6	V6
	-2	V6	V1	V1	V2	V2	V3	V3	V4	V4	V5	V5	V6
-1	2	V3	V4	V4	V5	V5	V6	V6	V1	V1	V2	V2	V3
	1	V4	V4	V5	V5	V6	V6	V1	V1	V2	V2	V3	V3
	-1	V7	V5	V0	V6	V7	V1	V0	V2	V7	V3	V0	V4
	-2	V5	V6	V6	V1	V1	V2	V2	V3	V3	V4	V4	V5

Torque comparator conditions for this scheme are provided by the following equations:

$$HT = 2 \text{ for } (T_{em}^* - T_{em}) \geq HB_T/2 \quad (3.13)$$

$$HT = 1 \text{ for } HB_T/2 \geq (T_{em}^* - T_{em}) \geq 0 \quad (3.14)$$

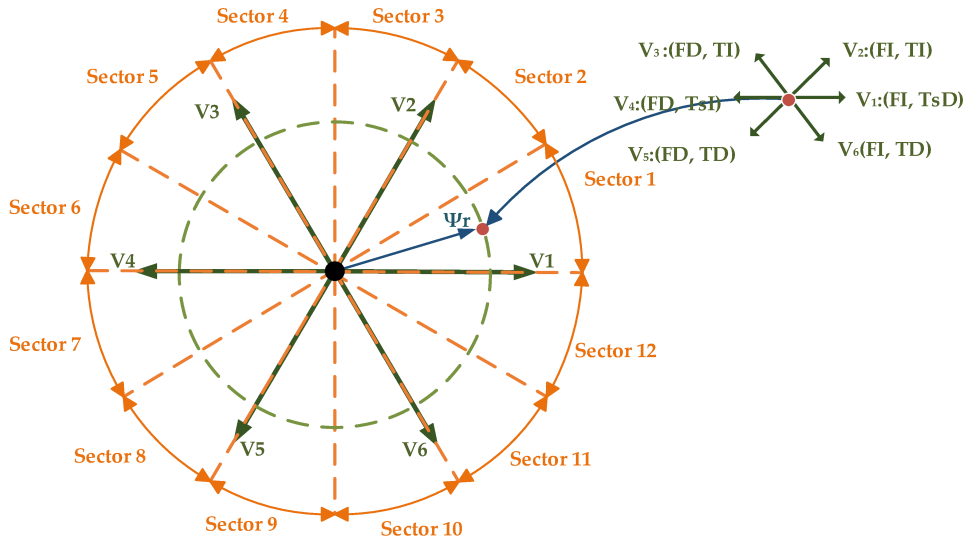


Figure. 3.9 Voltage vectors in twelve sector DTC scheme.

$$HT = -1 \text{ for } -HB_T/2 \leq (T_{em}^* - T_{em}) \leq 0 \quad (3.15)$$

$$HT = -2 \text{ for } (T_{em}^* - T_{em}) \leq -HB_T/2 \quad (3.16)$$

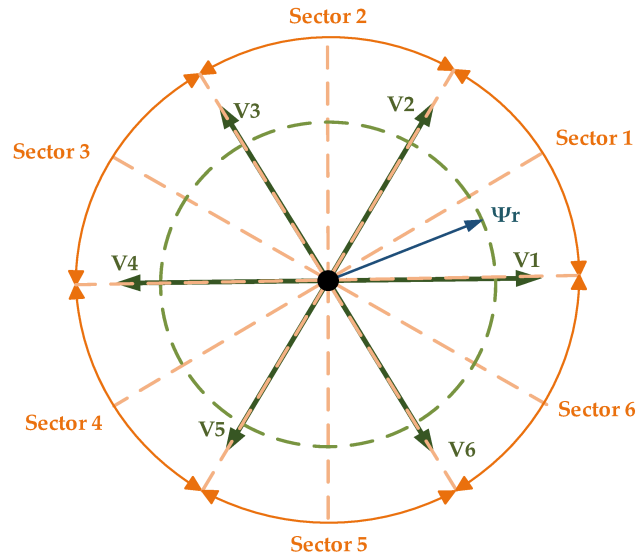
3.2.2 Modified Switching Table DTC

In the conventional DTC, there are two states in each sector not used (e.g V1, V4 in the first sector), and the torque is not determined. These conditions can be seen in Table 3.3. Torque can increase during 30° of the sector and decrease in the other 30° within the same sector; this drawback can be avoided by using a modified switching table in which there are two states where the flux is not determined (e.g V3, V6 in the first sector) instead of torque. Nevertheless, with the DTC mainly focused on torque control, this can be considered as an advantage of this scheme, a comparison of sectors zones for both schemes. Torque and flux status are illustrated in Table 3.5. The sectors in the modified DTC are shifted by 30° , as shown in Figure 3.10. Thus the first sector zone is changed from $-30^\circ \rightarrow 30^\circ$ in conventional DTC, to $-60^\circ \rightarrow 0^\circ$ in modified DTC.

The torque and flux comparator conditions for this scheme are the same as for conventional section which were given by (3.8-3.10). The difference between both control methods concerns the switching table. Table 3.6 presents the switching table for the modified DTC.

Table 3.5 Comparison of sectors zones for conventional and modified DTC.

Sector Number	Conventional DTC	Modified DTC
1	$-30^\circ \rightarrow 30^\circ$ Torque not determined	$-60^\circ \rightarrow 0^\circ$ TI, FI
2	$30^\circ \rightarrow 90^\circ$ TD, FI	$0^\circ \rightarrow 60^\circ$ TD,FI
3	$90^\circ \rightarrow 150^\circ$ TD, FD	$60^\circ \rightarrow 120^\circ$ Flux not determined
4	$150^\circ \rightarrow 210^\circ$ Torque not determined	$120^\circ \rightarrow 180^\circ$ TD, FD
5	$210^\circ \rightarrow 270^\circ$ TI, FD	$180^\circ \rightarrow 240^\circ$ TI, FD
6	$270^\circ \rightarrow 330^\circ$ TI, FI	$240^\circ \rightarrow 300^\circ$ Flux not determined

**Figure. 3.10** Voltage vectors in modified DTC scheme.

3.3 Simulation Results and Discussion

A 3-phase 2 MW DFIG is used for simulations with the characteristics in Appendix A. The simulations have been made under a constant sub-synchronous speed $N_{mech} = 0.8 N_s$, with $N_s = 1500$ rpm, and the

Table 3.6 Switching table of modified DTC

Number of Sector		1	2	3	4	5	6
$H\psi_r$	$H\text{Tem}$						
	1	V1	V2	V3	V4	V5	V6
1	0	V7	V0	V7	V0	V7	V0
	-1	V2	V3	V4	V5	V6	V1
	1	V5	V6	V1	V2	V3	V4
-1	0	V0	V7	V0	V7	V0	V7
	-1	V4	V5	V6	V1	V2	V3

results is presented in this section (the same simulations were done for different rotating speeds and the results give similar behavior), and imposing step changes of the torque in generating in addition to motoring modes which could be used in grid stabilization during fault conditions. For simulation of the three different DTC techniques that were mentioned before, the voltage source inverter is used, and the simulations have been carried out using MATLAB/SIMULINK.

The results were obtained for conventional six sectors DTC, twelve sectors DTC, and DTC with modified switching table. The inverter switching frequency was limited to 5 kHz, and the sampling time was 0.3 μsec .

The torque hysteresis band was 5% T_{nom} , and flux hysteresis value was 2% ψ_{nom} . The DC-link voltage was kept constant at the value of 1200 V.

The same simulations in this section have been also implemented for a 3.5 kW DFIG and its parameters were determined experimentally and provided in Appendix A. The results with the three DTC techniques are presented in Appendix B.

3.3.1 Conventional DTC

The torque oscillated around its reference values, which varied as: $0 \rightarrow -0.5 T_{nom} \rightarrow -0.2 T_{nom} \rightarrow 0.4 T_{nom}$ at 0, 1.5, 2.5, and 3.5 sec respectively, as can be seen in Figure 3.11. Electromagnetic torque was not distorted, and followed the reference but with notable ripples. The reference was reached very quickly. This behavior confirms one of the most significant advantages of DTC.

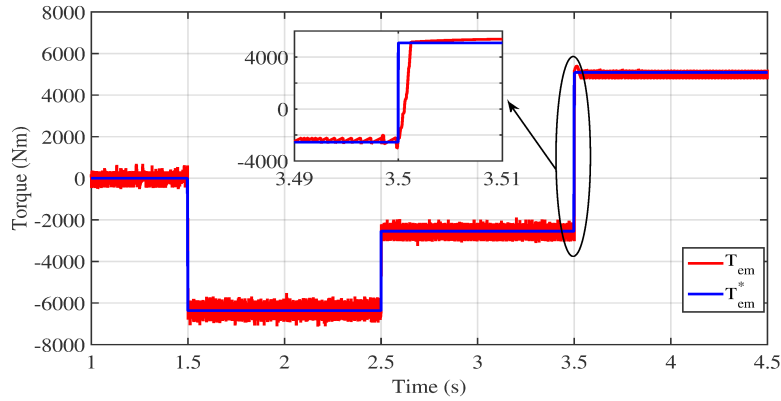


Figure. 3.11 Electromagnetic torque.

The steady state response of the rotor circuit of DFIG is presented in Figure 3.12. The rotor current and voltage reacted with the torque step changes, and the flux followed its reference value with respect to the imposed band.

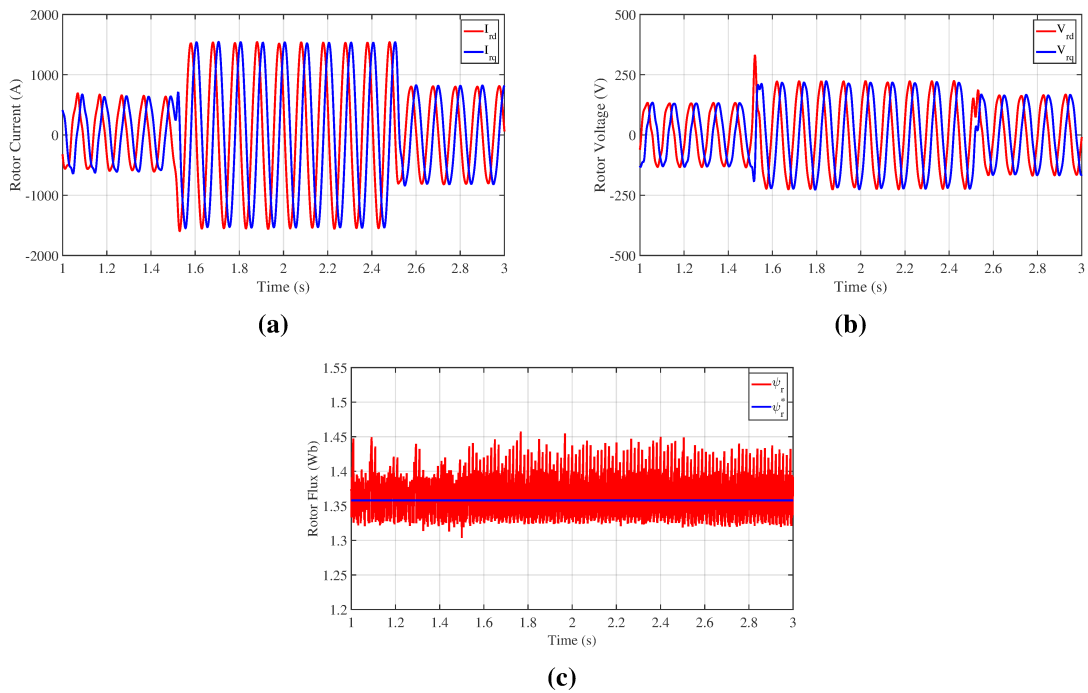


Figure. 3.12 (a) Rotor current in dq, (b) Rotor voltage in dq, and (c) Rotor flux.

The stator three phase current and voltage are sinusoidal, as can be seen in Figure 3.13. Figure 3.14 presents the stator active and reactive powers, which vary according to the torque as well. The occupation zones (sectors) where rotor flux is located can be seen in Figure 3.15.

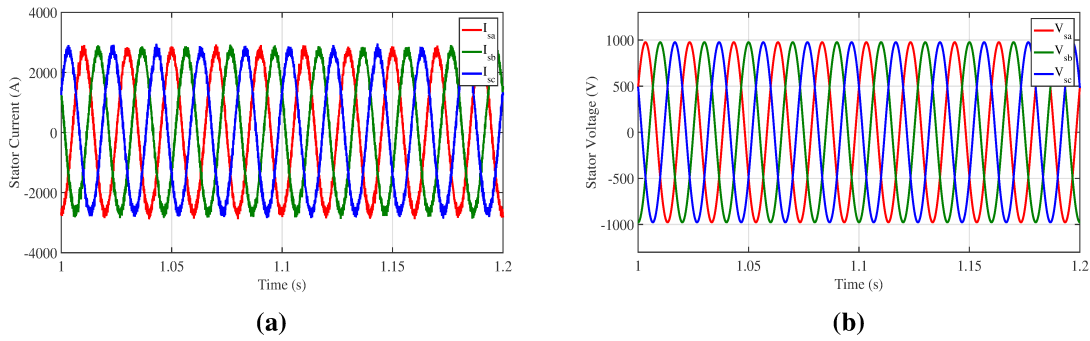


Figure. 3.13 (a) Three phase stator current, (b) Three phase stator voltage.

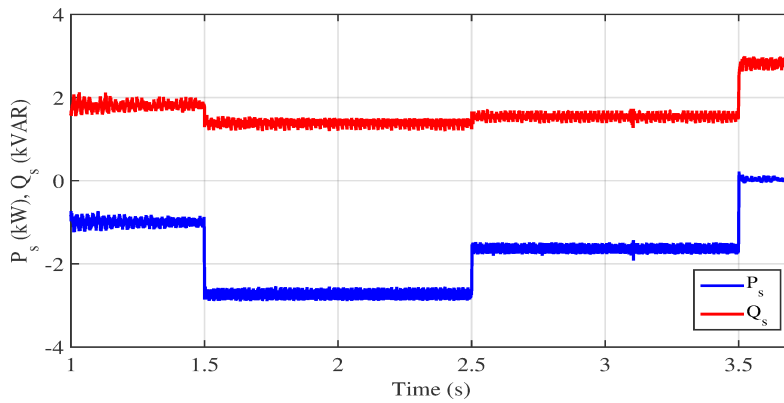


Figure. 3.14 Active and reactive powers.

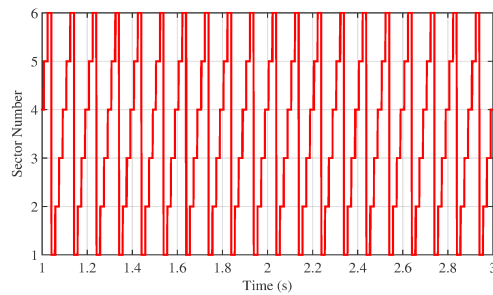


Figure. 3.15 Rotor flux sectors for conventional DTC.

3.3.2 Twelve Sectors DTC

The electromagnetic torque and rotor flux response for DFIG in twelve sectors DTC is shown in Figure 3.16. The main difference between this control scheme and the conventional one is the sectors division, Figure 3.17 presents the sector number with respect to time.

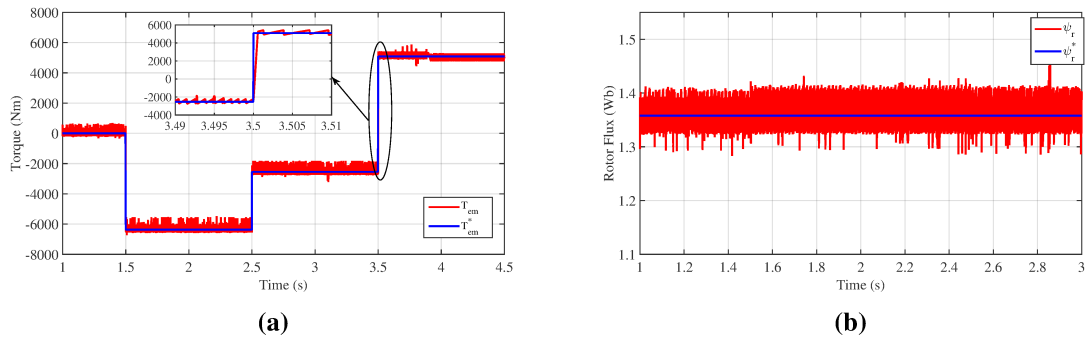


Figure. 3.16 (a) Electromagnetic torque, (b) Rotor flux for twelve sectors DTC.

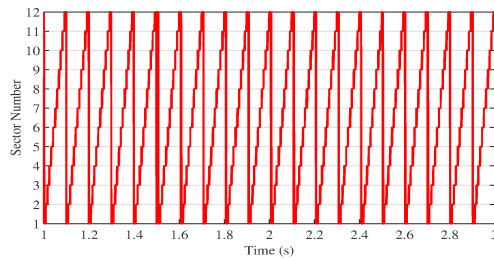


Figure. 3.17 Rotor flux sectors for twelve sectors DTC.

3.3.3 DTC with Modified Switching Table

The steady state response for DFIG in modified switching table DTC is shown in Figures 3.18. Electromagnetic torque and rotor flux are presented, and the torque response is zoomed for better insight. The main difference between this control scheme and the conventional one is the sectors division, as described before in Section 3.2.2.

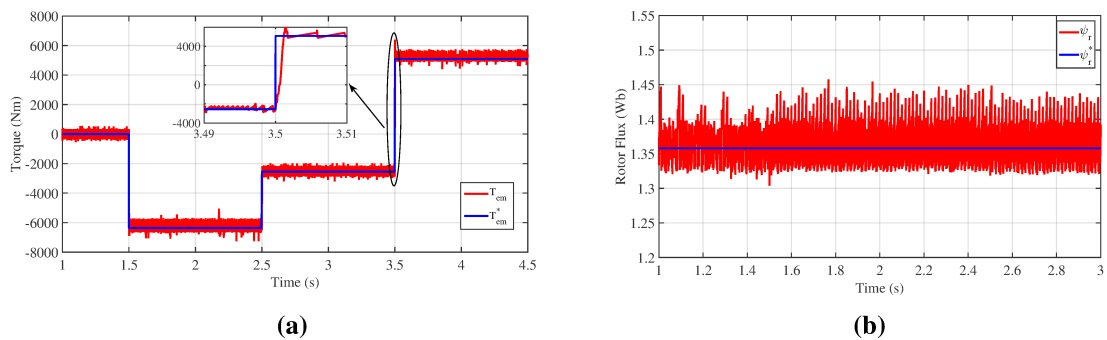


Figure. 3.18 (a) Electromagnetic torque, (b) Rotor flux with modified DTC.

3.3.4 Comparison and Discussion

According to the torque response developed, it becomes clear that the different DTC strategies have a very good torque performance in which the torque reaches steady state very fast. Nevertheless, there are some differences in torque, flux, and current ripples, which are discussed in this section in further detail to define the best DTC technique. As stated in Section 3.1.5, the switching frequency of the DTC algorithm is variable due to hysteresis controllers, but it has to be limited to protect the IGBTs from high frequency values. Thus it is useful if the switching frequency is compared for the three DTC techniques; Figure 3.19 shows the average values for the switching frequency of the proposed DTC algorithms, the switching frequency was calculated every 20 ms periods. It can be noted that the switching frequency of the DTC methods are relatively close to each other, though in the case of modified DTC, it has more fluctuations.

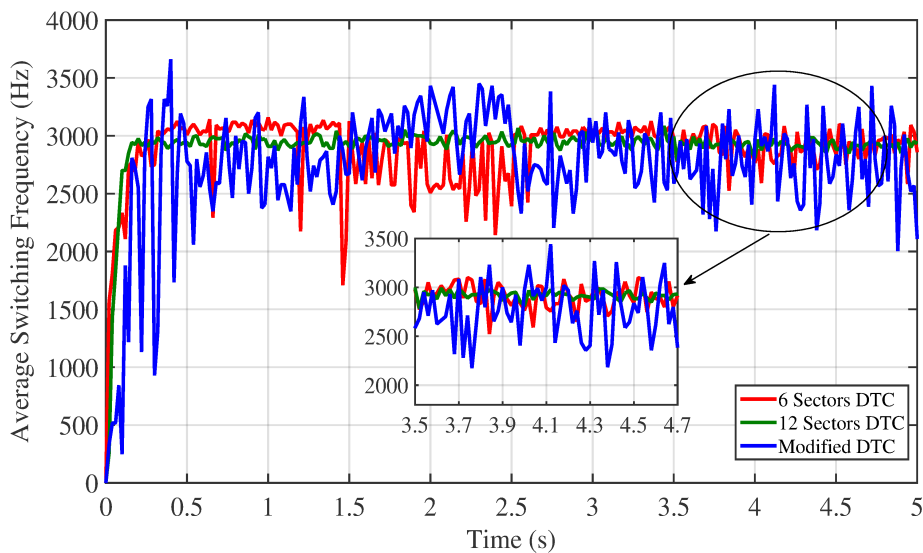


Figure. 3.19 Average switching frequency of DTC techniques.

Table 3.7 shows comparison analysis between DTC techniques with respect to some properties. From the table, it can be realized that twelve sectors DTC has some attractive factors over the other control techniques.

Table 3.7 Comparison analysis between DTC algorithms.

Property	Conventional DTC	Twelve Sectors DTC	Modified DTC
Dynamic response	Fast (700 μ s)	Fast (700 μ s)	Fast (800 μ s)
Torque and flux states in each sector	Two torque states are not determined	All voltage vectors torque and flux are determined	Two flux states are not determined
Ripples	Torque and flux ripples	Torque and flux ripples	Torque and flux ripples
Torque and flux variation	Small and large torque variation are not notable	Small and large torque variation can be notable	Small and large torque variation are not notable

As mentioned before, the main disadvantage of DTC is the ripple in torque and flux due to switching, so that it is useful to study this factor and compare DTC methods. Table 3.8 presents the ripples percentage of torque and flux at different times. Accordingly, as expected, all DTC algorithms have ripples in torque and flux. Conventional and modified DTC have close ripple percentages, but the conventional DTC has lower ripples values, while it is obvious that the twelve sectors DTC has the best performance, and the ripples are reduced over the other methods.

Table 3.8 Ripples percentage of torque and flux for DTC algorithms.

DTC Method	Conventional DTC		Modified DTC		Twelve Sectors DTC	
	Torque Ripple	Rotor Flux Ripple	Torque Ripple	Rotor flux Ripple	Torque Ripple	Rotor Flux Ripple
-0.5 *Tnom	6.28 %	2.39%	4.78%	3.86%	3.81%	2.61%
-0.2 *Tnom	13.12%	2.45%	10.99%	3.61%	9.58%	2.2%
0.4 *Tnom	6.41%	12.56%	6.06%	12.84%	4.55%	1.77%

To achieve a deeper analysis of DTC schemes, the waveform of stator current and its harmonic spectrum in the time interval (1.5-2.5)s for all DTC strategies is shown in Figure 3.20. The total harmonic distortion (THD) of stator current are 6.5%, 2.25%, and 16.95% for conventional, twelve sectors, and modified DTC respectively.

It is clear from the analysis of the performance, ripple calculations, and THD comparison of the DTC techniques that the twelve sectors DTC has the best performance and least amount ripples when compared to conventional and modified DTC.

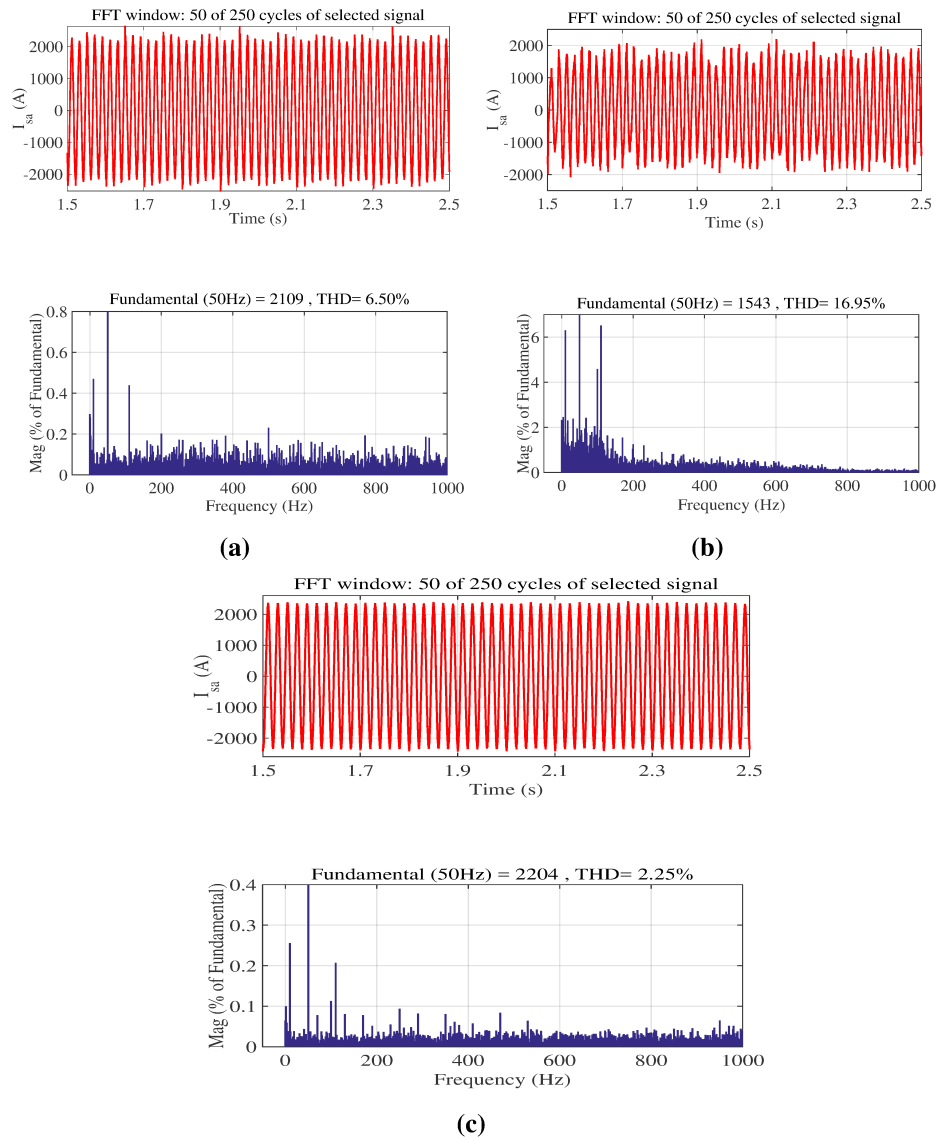


Figure. 3.20 Spectrum waveform of the stator current for: (a) Conventional DTC, (b) Modified DTC. (c) Twelve sectors DTC.

3.4 Direct Power Control for DFIG

The main control algorithms for DFIGs are vector control and direct control. The direct control algorithm has two different approaches depending on the control parameters. In the previous sections, DTC has been explained as well as various improvement possibilities; in this section, the direct power control DPC is presented and the results are compared with the conventional DTC. As mentioned before, the principle of DPC is very close to the DTC. The main difference between them is in the

variables that are used to directly control the machine [23–26]. In the DPC, control variables are the active and reactive powers on the stator side, which can be expressed as:

$$P_s = \frac{3}{2} \text{Re}(\vec{v}_s^r \cdot \vec{i}_s^{r*}) \quad (3.17)$$

$$Q_s = \frac{3}{2} \text{Im}(\vec{v}_s^r \cdot \vec{i}_s^{r*}) \quad (3.18)$$

Using (2.45), the stator current can be given by:

$$\vec{i}_s^r = \frac{\vec{\psi}_s^r}{\sigma L_s} - \frac{L_{sr} \vec{\psi}_r^r}{\sigma L_s L_r} \quad (3.19)$$

Moreover, from (2.44) the stator voltage in the rotor reference frame can be written as:

$$\vec{v}_s^r = R_s \cdot \vec{i}_s^r + \frac{d}{dt} \vec{\psi}_s^r + j\omega_m \vec{\psi}_s^r \quad (3.20)$$

Thus, if the voltage drop in the stator resistance is neglected, by substituting (3.19) and (3.20) into the power expressions and with some mathematical calculations, these assume the form:

$$P_s = \frac{3}{2} \frac{L_{sr}}{\sigma L_s L_r} \omega_s |\vec{\psi}_s^r| \cdot |\vec{\psi}_r^r| \sin(\delta) \quad (3.21)$$

$$Q_s = \frac{3}{2} \frac{\omega_s}{\sigma L_s} |\vec{\psi}_s^r| \cdot \left[\frac{L_{sr}}{L_r} |\vec{\psi}_s^r| - |\vec{\psi}_r^r| \cos(\delta) \right] \quad (3.22)$$

Analyzing these equations, the control variables can be defined as:

- Stator flux $\vec{\psi}_s^r$: The stator is directly connected to the grid; thus, the stator flux space vector can be assumed to have constant amplitude and rotating speed.
- Rotor flux $\vec{\psi}_r^r$ and angle δ : in 3.21 and 3.22 it can be noticed that the terms $|\vec{\psi}_r^r| \sin(\delta)$ and $|\vec{\psi}_r^r| \cos(\delta)$ influence active and reactive powers respectively. This influence indicates that, by controlling these terms separately, the active and reactive power control can be decoupled.

In Figure 3.21, the space vector representation of stator and rotor fluxes is shown. As can be noticed,

the terms $|\vec{\psi}_r^r| \sin(\delta)$ and $|\vec{\psi}_r^r| \cos(\delta)$ are the components of the rotor flux at the perpendicular and the same direction of the stator flux respectively. As such, if the change of the rotor flux is at the perpendicular direction of the stator flux, the active power P_s is changed. Otherwise, if the rotor flux changes at the same direction of the stator flux, the reactive power is changed.

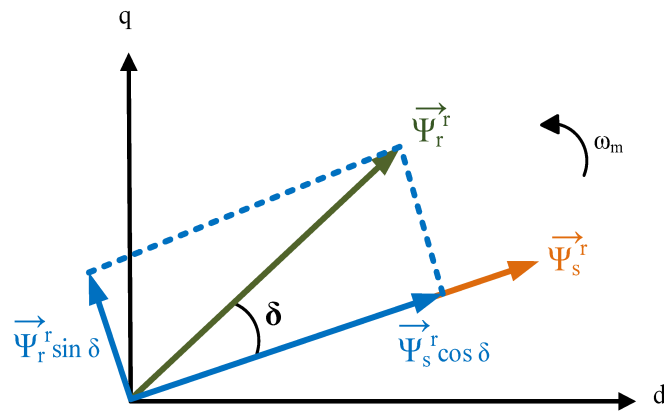


Figure. 3.21 The space vector representation of stator and rotor fluxes in the rotor reference frame.

Then, if a two-level converter is used, the same considerations made for the DTC can be followed. Hence, the expression (3.4) which shows the relationship between rotor flux and rotor voltage, can be taken into consideration. From the knowledge of the relative position between stator and rotor fluxes, by imposing the rotor voltage, the purpose of modifying the angle δ and the amplitude of the rotor flux can be achieved. Table 3.9 defines the voltage vectors selection in conventional DPC, and Figure 3.22 shows the voltage vectors with an example of selection in the first sector.

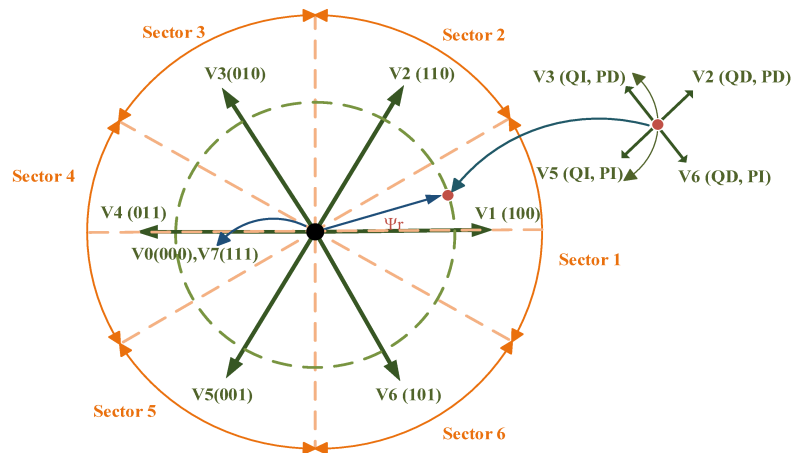


Figure. 3.22 Voltage vectors in conventional DPC scheme.

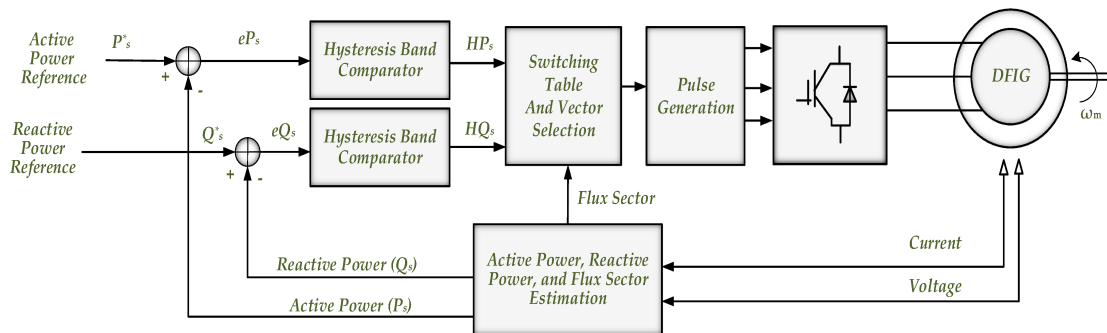
Table 3.9 Voltage vectors selection table for DPC.

HQ_s	HP_s	Voltage Vector
	1	$V(k-2)$
1	0	$V(0,7)$
	-1	$V(k+2)$
	1	$V(k-1)$
-1	0	$V(0,7)$
	-1	$V(k+1)$

3.4.1 DPC Implementation

The DPC system is illustrated in Figure 3.23, and the technique implementation can be divided into these steps:

- Active and reactive power estimation;
- Comparison between reference and estimated values;
- Error elaboration for active and reactive power through hysteresis controllers;
- Rotor voltage selection according to the power errors and the rotor flux position.

**Figure. 3.23** Schematic diagram of DPC.

3.4.2 Active Power, Reactive Power and Stator Flux Estimation

The control variables P_s and Q_s can be calculated from the measured voltages and currents as shown in (2.47) and (2.48). However, because the power is mainly delivered from the stator side, it can be

estimated in the stator reference frame as follows [89]:

$$P_s = \frac{3}{2}(v_{sd}i_{sd} + v_{sq}i_{sq}) \quad (3.23)$$

$$Q_s = \frac{3}{2}(v_{sq}i_{sd} - v_{sd}i_{sq}) \quad (3.24)$$

As stated before, together with the power values, DPC requires the sector in which the rotor flux is located. Using the same equation for DTC, the flux position can be calculated from the flux phase angle θ_{ψ_r} .

3.4.3 Active Power Reference

The active power and electromagnetic torque are related by the following expression [12]:

$$P_s = T_{em} \frac{\omega_s}{P_p} \quad (3.25)$$

Therefore, the active power reference is deduced from the torque reference which was mentioned before in DTC as step changes of torque.

3.4.4 Hysteresis Controllers and Rotor Voltage Vector Selection

Two hysteresis controllers are used in DPC to keep errors between reference and estimated values within prefixed band values. Different from DTC, in this case the zero vectors (V0 and V7) produce a variation in both the active and reactive powers, and their effects are different depending on the operating rotor speed, if in sub-synchronous or hyper-synchronous mode [59]. Moreover, since the rotor resistance has been neglected in (3.3), the impact of the zero vectors is more complicated. For these reasons, the DPC has been implemented with a three-level hysteresis comparator for active power and a two-level hysteresis comparator for reactive power. Both the comparators are shown in Figure 3.24.

The controller outputs HP_s , HQ_s , and the sector number are used to choose the most suitable rotor voltage vector, following the look-up Table 3.10.

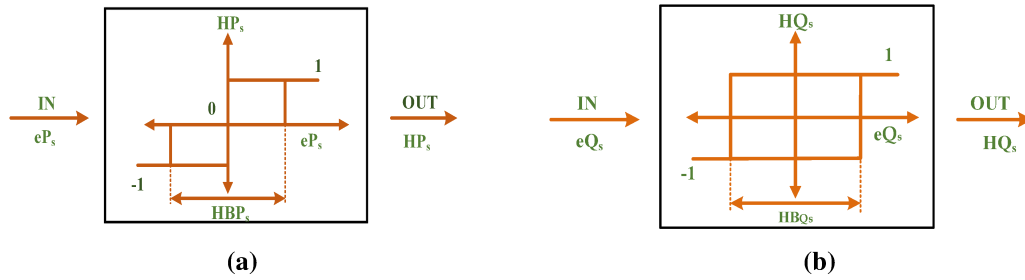


Figure. 3.24 a) Active power hysteresis comparator, b) Reactive power hysteresis comparator.

Table 3.10 Switching table for the conventional DPC

Number of Sector		1	2	3	4	5	6
HQ _s	HP _s						
1	1	V5	V6	V1	V2	V3	V4
	0	V7	V0	V7	V0	V7	V0
	-1	V3	V4	V5	V6	V1	V2
-1	1	V6	V1	V2	V3	V4	V5
	0	V0	V7	V0	V7	V0	V7
	-1	V2	V3	V4	V5	V6	V1

3.4.5 Simulation Results and Discussion

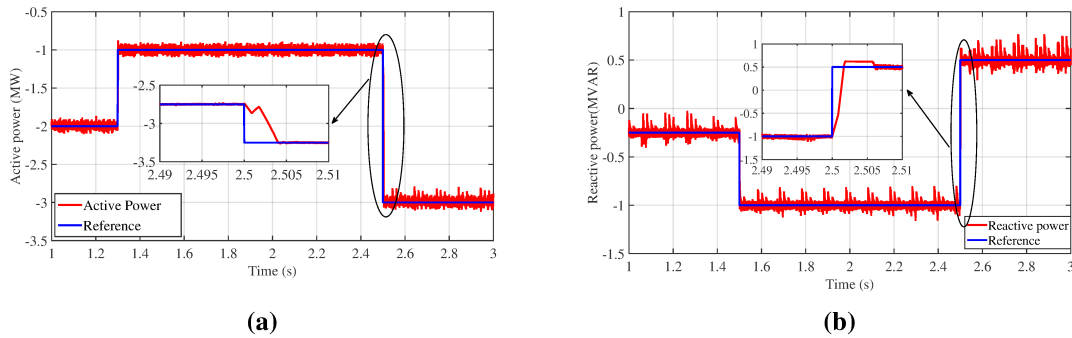


Figure. 3.25 (a) Active power, (b) Reactive power, with DPC.

The dynamic behavior of active and reactive powers is shown in Figures 3.25a and 3.25b respectively. As can be seen, the active power changes according to a step reference from $-P_{nom}$ to $-0.5 * P_{nom}$ at 1.3 s then another step to $1.5 * P_{nom}$ at 2.5 s. The reactive power follows its reference which changes from $-0.5 * Q_{nom}$ to $-2 * Q_{nom}$ at 1.5 s and then to Q_{nom} at 2.5 s. Where $P_{nom} = 2$ MW and $Q_{nom} = 0.5$ MVAR.

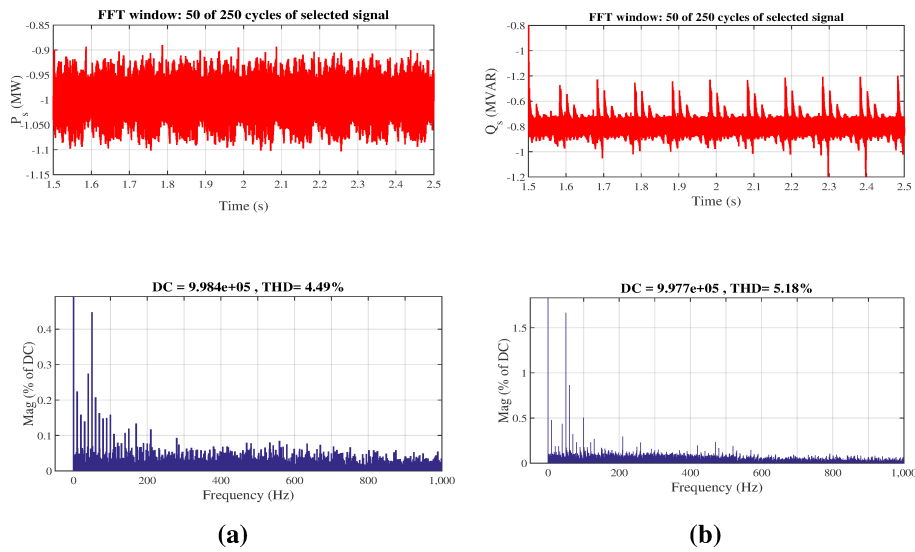


Figure. 3.26 Spectrum waveform with DPC for: (a) Stator active Power, (b) Stator reactive power.

The dynamic response of DPC is relatively fast, as demonstrated in Figure 3.25. It took 4 ms for the active power to track its reference step change at 2.5s, while the reactive power responds in 5.8 ms at the same time. Thus, by comparing these results with those in Table 3.7, the dynamic response of the DPC is considered to be slower than the DTC techniques.

A spectrum analysis of the active and reactive power waveforms has been done. Figure 3.26 shows that the THD for active and reactive power are 4.49 % and 5.18 % respectively.

3.5 Chapter Conclusion

Direct control techniques (DTC and DPC) have been chosen in this analysis due their advantages over the classical FOC. From the results shown in this chapter, it can be concluded that the DTC techniques have an effective torque performance, in which the torque reaches steady state very fast, but the ripples of torque, flux, and current waveforms are different.

According to the results, DTC with twelve sectors shows better performance than conventional and modified algorithms; the ripple percentage and THD are reduced in this control scheme.

DPC is also analyzed in this chapter, and from the results and discussion, it can be concluded that DTC has better performance than DPC according to dynamic behavior and THD.

Chapter 4

Grid Side Converter

In chapter 3, RSC control, including different DTC topologies, was discussed, in addition to DPC. In this chapter, GSC control is described in detail. The purpose of the GSC is to keep the DC-link voltage at a constant value and control the power exchanges to yield a unity power factor [90, 91]. These two objectives can be obtained by controlling the inverter through a vector control scheme that is introduced in the next section. Firstly, the model of the GSC is developed to achieve the relationships between active and reactive powers, and voltages and currents. Then the vector control is implemented, and later, an LCL grid filter is designed to improve inverter output signal.

4.1 Grid Side Converter Structure

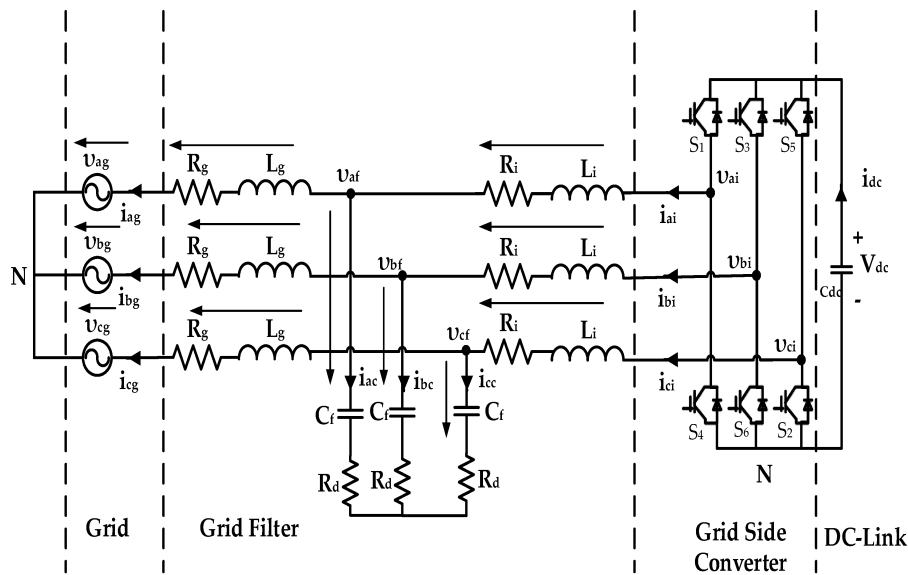


Figure. 4.1 Grid Side Converter equivalent circuit.

The GSC can be represented by the circuit in Figure 4.1 (LCL filter is used in this analysis and the details will be discussed further in the following sections). Where v_a , v_b and v_c are the voltages in abc reference frame. i_a , i_b and i_c are the currents in abc reference frame; with g and i denoted grid side and inverter side respectively. R_g and L_g are the grid side filter resistance and inductance. R_i and L_i are the inverter side filter resistance and inductance. C_f and R_d are the filter capacitance and

damping resistance. v_{dc} and i_{dc} are the voltage and current through the dc link capacitor. Thus, by applying Kirchhoff's law, the following equations can be immediately obtained:

$$\begin{cases} v_{ag} = v_{af} + i_{ag}R_g + L_g \frac{di_{ag}}{dt} \\ v_{bg} = v_{bf} + i_{bg}R_g + L_g \frac{di_{bg}}{dt} \\ v_{cg} = v_{cf} + i_{cg}R_g + L_g \frac{di_{cg}}{dt} \end{cases} \quad (4.1)$$

$$\begin{cases} v_{ai} = v_{af} + i_{ai}R_i + L_i \frac{di_{ai}}{dt} \\ v_{bi} = v_{bf} + i_{bi}R_i + L_i \frac{di_{bi}}{dt} \\ v_{ci} = v_{cf} + i_{ci}R_i + L_i \frac{di_{ci}}{dt} \end{cases} \quad (4.2)$$

The current through the capacitor branch of the filter is given by:

$$\begin{cases} i_{ac} = i_{ai} - i_{ag} = C_f \frac{d}{dt}(v_{af} - i_{ac}R_d) \\ i_{bc} = i_{bi} - i_{bg} = \frac{d}{dt}(v_{bf} - i_{bc}R_d) \\ i_{cc} = i_{ci} - i_{cg} = \frac{d}{dt}(v_{cf} - i_{cc}R_d) \end{cases} \quad (4.3)$$

At frequencies lower than half of the resonance frequency, the LCL filter can be considered as RL filter [90]. Thus, the filter can be simplified as:

$$R_f = R_i + R_g \quad (4.4)$$

$$L_f = L_i + L_g \quad (4.5)$$

Here, R_f and L_f are the filter resistance and inductance of the RL filter as assumed. Therefore, to perform the vector control, the space vector representation introduced in section 2.2.1 is applied on equations (4.1), (4.2) and (4.3). The dq model of the GSC in an arbitrary reference frame rotating

[12]:

$$P_{gc} = \frac{3}{2}(v_{dg}i_{dg} + v_{qg}i_{qg}) \quad (4.8)$$

$$Q_{gc} = \frac{3}{2}(v_{qg}i_{dg} - v_{dg}i_{qg}) \quad (4.9)$$

Hence, considering equations (4.6) and (4.7) to decouple the active and reactive power relationships, the angular speed ω is chosen equal to the grid angular speed ω_{gs} , and the d axis of the rotating reference frame is aligned with the grid voltage space vector, as shown in Figure 4.3.

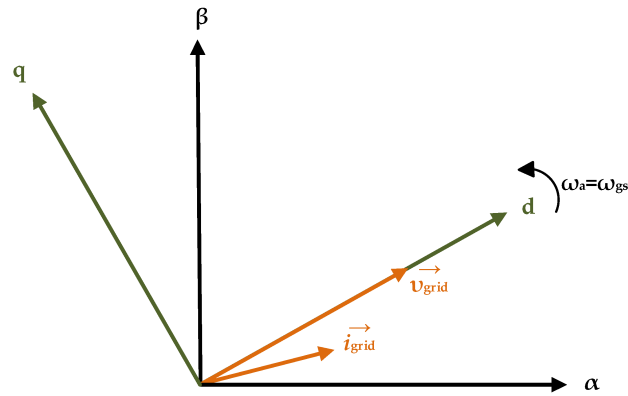


Figure. 4.3 Alignment of the d axis with the grid voltage space vector.

This decision yields the following expressions:

$$\omega_a = \omega_{sg} \quad (4.10)$$

$$v_{dg} = |\vec{v}_g| \quad (4.11)$$

$$v_{qg} = 0 \quad (4.12)$$

Substituting Equation (4.12) in equations (4.8) and (4.9), for simplicity in notation, the superscript is omitted in the vectors rotating at the grid angular frequency, active and reactive powers can be given

by:

$$P_{gc} = \frac{3}{2}(v_{dg}i_{dg}) \quad (4.13)$$

$$Q_{gc} = -\frac{3}{2}(v_{dg}i_{qg}) \quad (4.14)$$

Thus, under ideal conditions, the voltage term v_{dg} is constant, and the active and reactive power could be controlled respectively by the d axis and the q axis currents. Because the aim of the control is to achieve a unity power factor, $Q_{gc} = 0$, the reference current in the q-axis should be zero, $i_{qg} = 0$. Regarding the current in the d axis, neglecting the harmonics due to the switching and ignoring the losses of IGBTs in Figure 4.1, the input and output powers should be equal. The following expression can then be written:

$$v_{dc}C_{dc}\frac{dv_{dc}}{dt} + v_{dc}i_{rsc} = \frac{3}{2}(v_{dg}i_{dg}) \quad (4.15)$$

Where i_{rsc} is the RSC current.

Hence, the purpose of the GSC control is to regulate the DC-link voltage and achieve a unity power factor. This goal can be achieved by controlling the dq axis currents. Rewriting the grid side converter equations (4.6) and (4.7) in the dq reference frame with the new assumptions derived from equations (4.10), (4.11) and (4.12) as follows:

$$v_{di} = L_f \frac{di_{dg}}{dt} + R_f \cdot i_{dg} - (\omega_{gs}L_f i_{qg} - v_{dg}) \quad (4.16)$$

$$v_{qi} = L_f \frac{di_{qg}}{dt} + R_f \cdot i_{qg} + (\omega_{gs}L_f i_{dg}) \quad (4.17)$$

As it can be noticed, the d and q axis have the coupling terms $\omega_{gs}L_f i_{qg}$ and $\omega_{gs}L_f i_{dg}$ due to the transformation. Thus, to achieve competitive control performances, a feed-forward control combined with PI controllers is used [12]. The PI controllers are chosen because they have successful performance in controlling constant quantities, such as the d-q currents in the synchronous reference frame. The

compensation terms, which have been put into brackets in (4.16) and (4.17), are as follows:

$$v_d^{comp} = -\omega_{gs}L_f i_{qg} + v_{dg} \quad (4.18)$$

$$v_q^{comp} = \omega_{gs}L_f i_{dg} \quad (4.19)$$

Therefore, by considering these terms, the controller output voltages are:

$$v_d' = v_{di} - v_d^{comp} = L_f \frac{di_{dg}}{dt} + R_f \cdot i_{dg} \quad (4.20)$$

$$v_q' = v_{q0} - v_q^{comp} = L_f \frac{di_{qg}}{dt} + R_f \cdot i_{qg} \quad (4.21)$$

Here, v_d' and v_q' are the outputs of the PI controllers. Hence, the last equations describe the currents loop, which is the inner control loop. The block diagram in Figure 4.2 represent the vector control of the GSC; a current reference for the inner loop, is given by an outer control loop which is needed to control the DC-link voltage.

4.3 Reference Frame Alignment

4.3.1 Zero Crossing Method

A simple method for detecting the phase and frequency information is to detect the zero-crossing of the grid voltage, by using comparators that can identify the changes in the polarity of the voltage [92–94]. But this method has two notable drawbacks. First, as the zero-crossing point can be detected only at every half period of the wave between two detecting points, the phase tracking cannot be obtained [95]. As such, the dynamic performance of this system is too slow. The second important drawback is that the grid voltage is prone to being corrupted by the notches from power device switching, low frequency harmonic content and noise, easily causing inaccuracy and multiple zero-crossing detection [96, 97]. Therefore, a digital filter is needed to obtain the fundamental component of the grid voltage at the line frequency. The delay introduced by the filter and the effects due to the noise and switching notches of the grid voltage can be avoided, and numerous techniques have been presented in the technical literature: advanced filtering techniques were presented in [97, 98],

and time to digital filtering algorithm was presented in [99]. However, starting from its simplicity, if the two major drawbacks are avoided by using advanced and relatively complex techniques, the zero-crossing method results in a complicated and unsuitable method if accuracy and fast tracking of the grid voltage angle are requested.

4.3.2 Arctangent Method

One more solution for obtaining the phase angle of the grid voltage is to implement the arctangent function to the voltages, transformed into a Cartesian coordinate system, such as stationary or synchronous reference frames. This method has been used in [100] for transforming feedback variables in different reference frames and in [101] for the grid voltage synchronization. However, the main drawback of this strategy is that to achieve an accurate detection of the phase angle and frequency even in case of distorted grid voltage, additional filtering is needed, as shown in the diagram blocks above. Therefore, it is more advisable to use different approaches for grid-connected converter applications.

4.3.3 Phase Locked Loop

Phase locked loop (PLL) is a widely used phase tracking algorithm, and it currently represents the state-of-the-art method for obtaining the phase angle of the grid voltage [102–105]. This algorithm is essentially a closed-loop feedback control; it is able to provide an output signal, which is synchronized in both phase and frequency with the reference input signal [106]. The PLL is commonly realized in the dq reference frame.

4.3.4 Reference Frame Method Selection

Chiefly, PLL is a closed-loop feedback signal control [107]. It has a simple and flexible structure. The PLL tracking algorithm has been chosen in this analysis so as to obtain the phase angle of the grid voltage because of its attractive specifications over the other methods mentioned before. Those specifications are as follows:

- Good filtering because of the narrow-band tracking feature.
- Ability of realizing perfect frequency control.
- High accuracy without complex calculations.
- Obtaining more accurate PWM.

- More efficient by presenting several options for clock configurations.
- Small number of measurements is used for phase and frequency tracking.

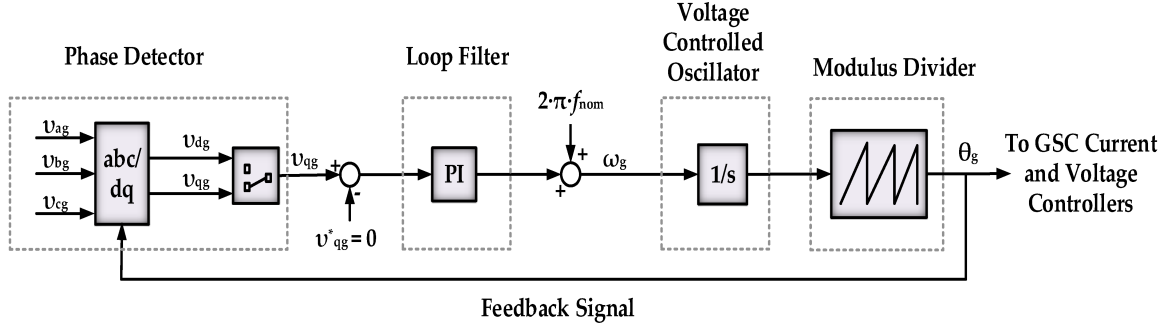


Figure. 4.4 PLL block diagram.

The block diagram of the PLL for phase tracking using the synchronous reference frame is shown in Figure 4.4. As can be noted, the input of the system is the measured grid voltage that is transformed into the dq reference frame. Because the d component of the grid voltage must be aligned with the rotating reference frame, the estimated angle θ_g is modified until the q component of the grid voltage is zero. Hence, after the transformation, the voltage in q axis is selected and compared with the constant zero reference, and the error is performed by a PI controller that gives as output the grid frequency. The PI output, when added to a feed-forward frequency and integrated provides the grid phase angle θ_g , whose inclination is cut every 2π magnitude by the Modulus divider block. The transfer function of the PLL can be written as follows:

$$H_{PLL}(s) = \frac{K_p \cdot s + \frac{K_p}{T_i}}{s^2 + K_p \cdot s + \frac{K_p}{T_i}} \quad (4.22)$$

This expression can be compared with the similar standard second order transfer function as given by:

$$G(s) = \frac{2\omega_n \xi \cdot s + \omega_n^2}{s^2 + 2\omega_n \xi \cdot s + \omega_n^2} \quad (4.23)$$

From (4.22) and (4.23) the gains of the PI controller can be calculated as functions of the damping factor ξ and the settling time T_{set} :

$$K_p = \frac{9.2}{T_{set}} \quad (4.24)$$

$$T_i = \frac{T_{set} \cdot \xi^2}{4.3} \quad (4.25)$$

Here, ω_n is the undamped natural frequency $\omega_n = 4.6 / T_{set} \xi$. Choosing a damping factor $\xi = 0.707$, which determine an overshoot of less than 5 % for a step response [108], and a settling time $T_{set} = 30$ ms, the values of the PI gains can be obtained. The achieved values are $K_p = 306.66 \text{ s}^{-1}/\text{V}$ and $T_i = 6.50$ ms, which give $K_i = K_p / T_i = 47178.46 \text{ s}^{-1}$. The grid phase angle synchronization has been implemented in MATLAB/Simulink, and the phase tracking is shown in Figure 4.5.

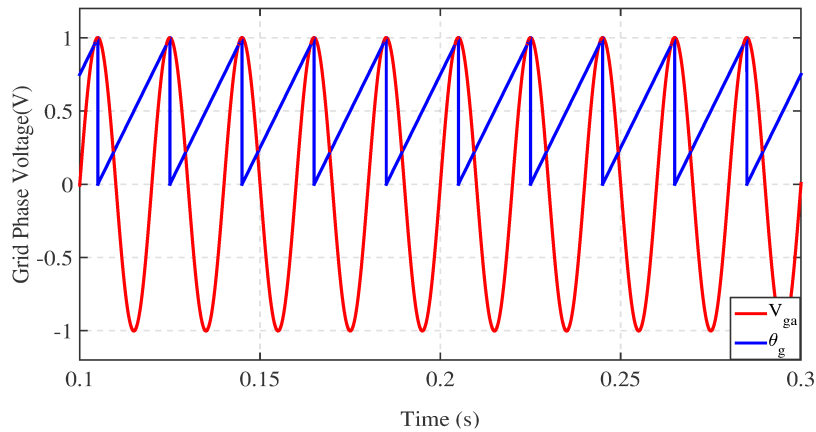


Figure 4.5 PLL tracking for the simulated grid phase voltage and the phase angle.

4.4 LCL Filter Design

Due to the harmonics of the GSC output current, a grid filter is located between GSC and the grid to eliminate the ripple and avoid its effect on the overall system efficiency. Typically, the connection of the converter to the grid is done by using a low-pass filter, which works to eliminate the high-frequency harmonics produced by the converter switching [109]. Traditionally, an L or LC [110, 111] filter is used. However, since the switching frequency usually cannot be very high, the result is a large, bulky, and expensive filter inductance. Compared to L type filter, the same amount of switching ripple

reduction can be achieved with smaller inductors using LCL filter. Thus, the LCL filter is an effective alternative which provides good performance and lower ripple and cost [112–114, 105, 106]. The LCL filter implemented is shown in Figure 4.6, where only one phase has been considered since each phase has the same configuration, the LCL filter components designed for the analyzed system using the following parameters according to [115–117]:

- Rated power: $P_{nom} = 2$ MW
- Rated line-to-line rms voltage: $V_{nom} = 690$ V
- Converter switching frequency: $f_{sw} = 5$ kHz
- DC link voltage reference: $V_{DC} = 1200$ V.

The filter parameters have to be chosen carefully as smaller values lead to resonance and instability, even though it can eliminate the current ripple [118].

4.4.1 Filter Parameters

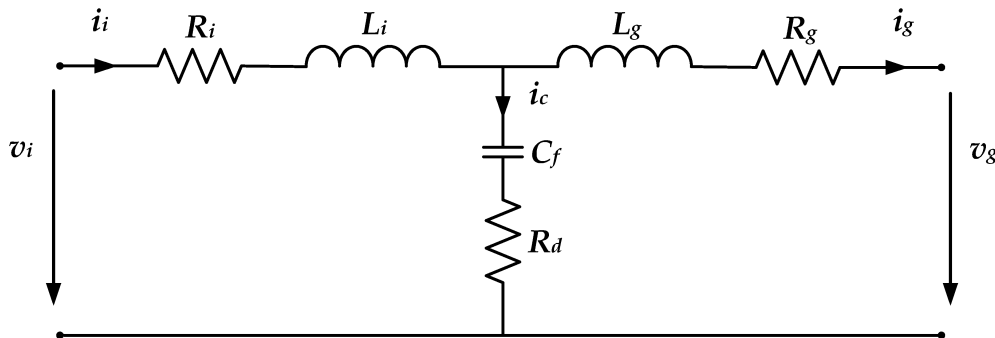


Figure 4.6 Ideal LCL equivalent circuit

First, the base values are calculated, as they are useful for the filter parameters calculation:

$$Z_b = \frac{V_{nom}^2}{P_n} \quad (4.26)$$

$$C_b = \frac{1}{\omega_{nom} Z_b} \quad (4.27)$$

Then, the converter side inductance is calculated by selecting the desired current ripple. The percentage of ripple (ripple coefficient n) can be calculated as:

$$n = \frac{\Delta i_{max,rip}}{I_i} \quad (4.28)$$

Here, $\Delta i_{max,rip}$ is the maximum increased or decreased inverter current (ripple current), and I_i is the rms inverter current. The coefficient (n) in this analysis was chosen as 10 % according to the German Electricity Association (VDEW) standard [119] and the analysis in [120], which also follows the VDEW standards where the ripple current's permitted range is between 10% and 20 % of the current in converter side. Thus, the ripple current can be achieved by:

$$\Delta i_{max,rip} = 0.1 \cdot I_i = 0.1 \cdot \frac{\sqrt{2}P_{nom}}{3 \frac{V_{nom}}{\sqrt{3}}} \quad (4.29)$$

Therefore, the inductance L_i can be evaluated by [121]:

$$L_i = \frac{V_{DC}}{4 \cdot \Delta i_{max,rip} \cdot f_{sw}} \quad (4.30)$$

To define the capacitor value, it should be considered that for converters connected to the grid, the reactive power absorbed at rated conditions is generally less than 5%. Thus, C_f is calculated as a percentage of the base value:

$$C_f = x \cdot C_b = 0.05C_b \quad (4.31)$$

Regarding the grid side inductance L_g , it can be calculated by selecting the desired current ripple attenuation with respect to the ripple of the converter side current:

$$\frac{i_{g(f_{sw})}}{i_{c(f_{sw})}} = \frac{1}{|L_g C_f \omega_{sw}^2 - 1|} = 10\% \quad (4.32)$$

Here, $i_{g(f_{sw})}$ and $i_{c(f_{sw})}$ are the grid and converter currents ripple respectively at the switching frequency. Having chosen the filter values, the resonance frequency can be calculated and used to check the system quality, as the following relationship must be respected to avoid resonance problems:

$$10 \cdot f_{grid} \leq f_{res} \leq 0.5 \cdot f_{sw} \quad (4.33)$$

Here, $10 \cdot f_{grid} = 10 \cdot 50 \text{ Hz} = 500 \text{ Hz}$ and $0.5 \cdot f_{sw} = 0.5 \cdot 5000 \text{ Hz} = 2500 \text{ Hz}$. The resonance frequency of the designed filter can be obtained as:

$$\omega_{res} = \sqrt{\frac{L_i + L_g}{L_i L_g C_f}} \quad , \quad f_{res} = \frac{\omega_{res}}{2\pi} \quad (4.34)$$

Thus, the relationship 4.32 is perfectly respected. As stated in the transfer function calculation, a damping resistor is employed to increase the stability of the system. The damping resistor should have a sufficient value to avoid oscillations, but it should not be excessively big otherwise it can cause large power losses. In this analysis, it is chosen as one-third of the impedance of the capacitors at resonant frequency [116]:

$$R_d = \frac{1}{3\omega_{res}C_f} \quad (4.35)$$

Simulation Results As stated before, the LCL filter is connected to the inverter output. The simulation results of the inverter output voltage, and current with and without using the filter, under the same conditions of Section 3.3 are illustrated in Figure 4.7. It is clear the voltage and current inverter outputs are very pure when the filter is used, as the performance is better, and the ripple is reduced.

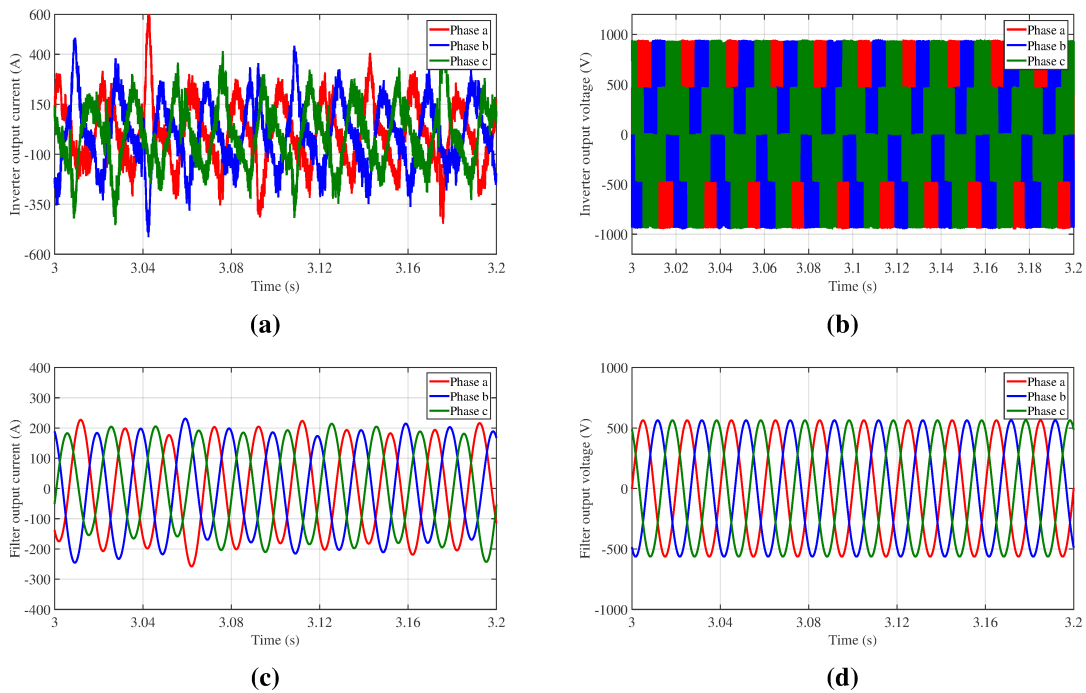


Figure. 4.7 (a) and (b): Grid current and voltage without using filter, (c) and (d): Grid current and voltage with using filter.

4.5 Chapter Conclusion

This chapter described the control of GSC of DFIG system. The purpose of GSC control is to maintain constant DC-link voltage. A vector control algorithm controls power exchanges to achieve unity power factor. Moreover, an LCL filter is implemented to filter the inverter output and reduce the harmonics of voltage and current. It can be seen in the results in previous section that the filter improves the inverter output and reduces the ripples, so its main purpose is achieved.

Chapter 5

Synchronization

As stated in the earlier chapters, one of the main advantages of the DFIG is the size reduction of the power converter connected to the rotor side of the generator. As such, the limited AC voltage only permits control of the machine in a range of speeds near to the synchronism ($\pm 30\%$). This feature of the DFIG requires finding another strategy for the startup of the machine, as the AC voltage requested from the machine during startup is higher than the voltage requested at normal operations around the synchronous speed [122, 123, 18, 124].

Typically, the solution adopted consists of disconnecting the stator of the machine from the grid by using a breaker so that the wind makes the rotor of the machine rotate [125–128]. Then, when the rotor reaches a controllable speed range, a connection process between stator and grid is carried out. Before closing the stator breaker and connecting the machine to the grid, some important conditions must be respected: The induced stator voltages must be as equal as possible to the grid voltages in phase, frequency, and amplitude. Therefore, a control strategy is necessary. The most generic algorithm is depend on a vector control that use two different PI controllers to accomplish the amplitude and phase equality separately [129]. In this chapter, the grid synchronization is achieved by using Direct Virtual Torque Control (DVTC), which provide some advantages, as direct torque control has been used for the control of normal operation of the machine [130, 129].

5.1 Principles of Direct Virtual Torque Control

As mentioned in the introduction to this chapter, before the synchronization of the stator voltage to the grid voltage, the stator breaker is opened as shown in Figure 5.1.

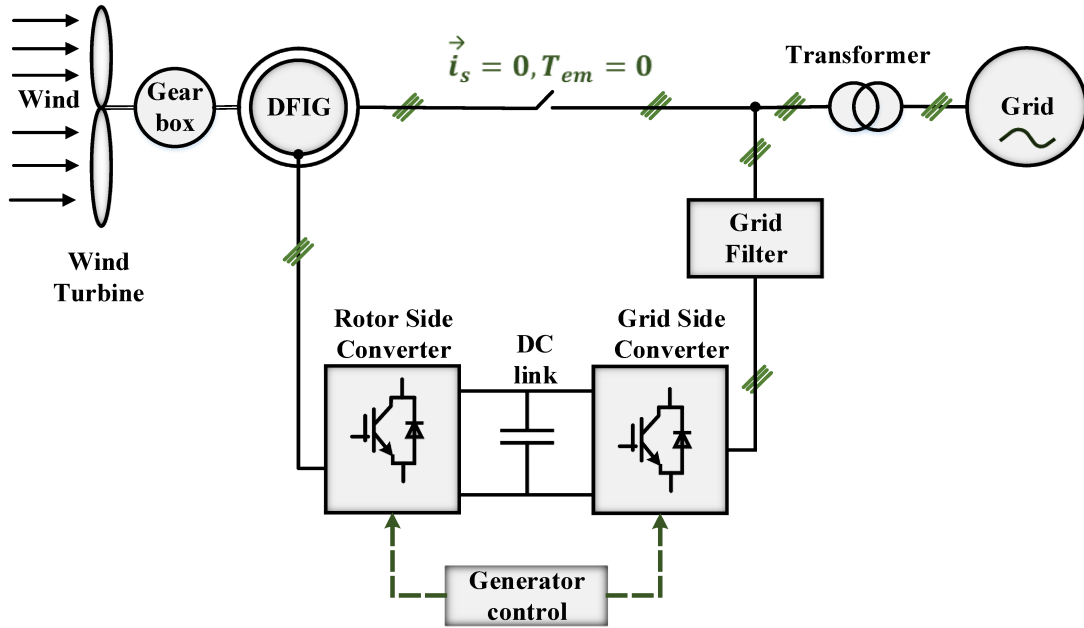


Figure 5.1 DFIG configuration in synchronization process.

Under these conditions, the stator current \vec{i}_s is equal to zero. As a consequence, from (3.5), it can be easily deduced that the electromagnetic torque T_{em} is equal to zero as well. Thus, instead of the torque T_{em} , the DVTC bases the control in a "virtual" torque T_{vi} in which the generator stator flux $\vec{\psi}_s$ is substituted by a "virtual" grid flux $\vec{\psi}_g$. This is defined in the next section. Therefore, the classical torque equation presented in (2.46) assumes the form:

$$T_{vi} = \frac{3}{2} P_p \frac{L_{sr}}{\sigma L_s L_r} \vec{\psi}_g \cdot \vec{\psi}_r \sin \delta_v \quad (5.1)$$

Summarizing, virtual torque is created by the real rotor flux $\vec{\psi}_r$ and the virtual grid flux $\vec{\psi}_g$ with δ_v the angle between them. The grid voltage vector \vec{v}_g can be expressed in terms of $\vec{\psi}_g$ as:

$$\vec{v}_g = \frac{d\vec{\psi}_g}{dt} \quad (5.2)$$

If expressed in the grid stationary reference frame, phase and magnitude of the virtual flux can be defined as follows:

$$\theta_{sg} = \tan^{-1} \frac{v_{g\beta}}{v_{g\alpha}} \quad (5.3)$$

$$|\vec{\psi}_g| = \frac{|\vec{v}_g|}{\omega_{gs}} \quad (5.4)$$

Here, ω_{gs} is the grid angular frequency [rad/s], $v_{g\alpha}$ and $v_{g\beta}$ are the α - β components of grid voltage. Once these magnitudes have been defined, the method of their control for the grid synchronization is investigated in the next section.

5.2 DVTC for Grid Synchronization

As stated before, the purpose of the control is to adjust the stator voltage until it reaches the same amplitude, phase, and frequency of the grid voltage. If the voltage drop in the stator resistance is neglected, the stator flux in the stator reference frame can be expressed as a function of the stator voltage:

$$\frac{d\vec{\psi}_s}{dt} = \vec{v}_s \quad (5.5)$$

$$\theta_{sg} = \tan^{-1} \frac{v_{s\beta}}{v_{s\alpha}} \quad (5.6)$$

Therefore, from Equations (5.2) and (5.5) it can be seen that the requirements of phase and frequency equality between stator voltage and grid voltage can be obtained by the phase and frequency equality between the stator flux $\vec{\psi}_s$ and the grid virtual flux $\vec{\psi}_g$. However, as stated in an earlier chapter, because the stator breaker is still opened the electromagnetic torque is zero. This means that the stator flux $\vec{\psi}_s$ and the rotor flux $\vec{\psi}_r$ are collinear (from Equation 2.46). Therefore, the aim of the control regarding phase and frequency synchronization can be met by bringing to collinearity the grid virtual flux $\vec{\psi}_g$ and the rotor flux $\vec{\psi}_r$. From Equation (5.1), δ_v must then be forced to zero, and thus the torque as well. This condition can be guaranteed by imposing a reference virtual torque equal to zero in the DVTC scheme, which is the same as the DTC scheme with the changes in the estimation and reference torque. Thus, the advantage of this synchronization technique is that the same structure with the same look-up table of DTC is used for load and no-load operations. The switching from the virtual torque estimator to the electromagnetic torque estimator does not decline the performance of the system, since in the transition from no-load to grid-connected mode both the torques are zero. As well known, another condition regarding the amplitude of the stator voltage must be imposed. This goal can be achieved by acting on the rotor flux controller, obtaining in this way a decoupled control

between the instantaneous phase and amplitude of the stator voltage. Taking into consideration the stator current, it follows that:

$$\vec{i}_s = 0 \quad (5.7)$$

And substituting its value to the flux equations of the machine presented in Equation (2.45), the following expressions are achieved:

$$\vec{\psi}_s = L_{sr} \cdot \vec{i}_r \quad (5.8)$$

$$\vec{\psi}_r = L_r \cdot \vec{i}_r \quad (5.9)$$

From the combination of the equations above and following the purpose of generating voltage and flux of the stator with the same amplitudes of the grid voltage and flux ($|\vec{v}_g| = |\vec{v}_s|$, $|\vec{\psi}_s| = |\vec{\psi}_g|$), the rotor flux reference should be imposed as follows:

$$|\vec{\psi}_r^*| = \frac{L_r}{L_{sr}} |\vec{\psi}_s| = \frac{L_r}{L_{sr}} |\vec{\psi}_g| = \frac{L_r}{L_{sr}} \frac{|\vec{v}_g|}{\omega_{gs}} \quad (5.10)$$

Controlling the rotor flux amplitude with this reference and the same look-up table used for DTC, it makes the stator voltage of the same amplitude of the grid voltage. It can be noted from (5.10) that only the measurement of grid voltage and frequency is requested.

The simulations of the grid synchronization have been carried out with the same DFIG characteristics used for both DTC and DPC.

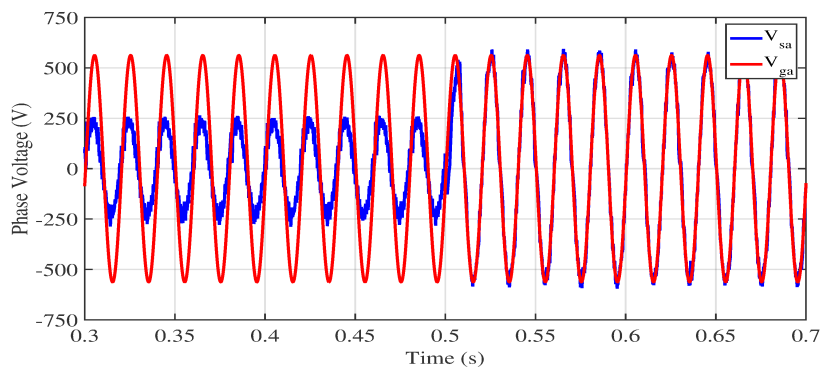
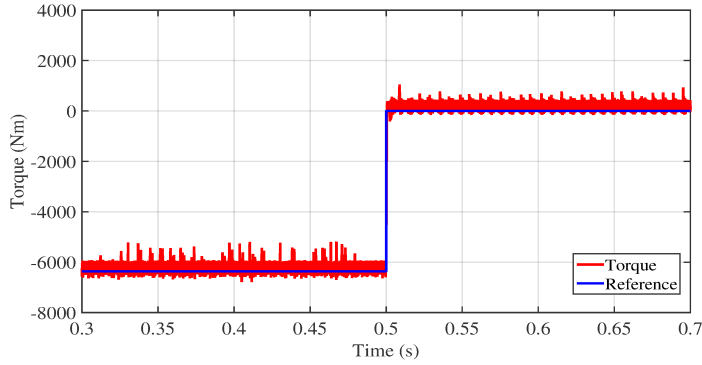


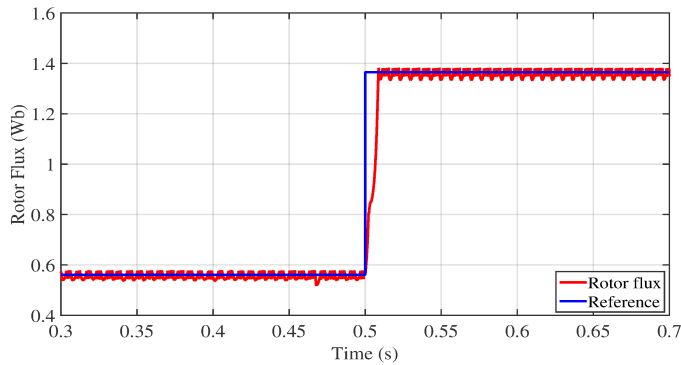
Figure. 5.2 Phase 'a' of grid and stator voltages during synchronization process.

In Figure 5.2, the synchronization in phase and frequency has been imposed at 0.5 s.

As it has been explained, the phase synchronization can be reached when the virtual torque is forced to zero. Therefore, in Figure 5.3a a torque step from $0.5 T_{nom}$ to zero has been imposed. The rotor flux changed from $0.5 |\vec{\psi}_r|_{nom}$ to $|\vec{\psi}_r|_{ref}$, which is shown in Figure 5.3b. As a consequence, the synchronization is achieved.



(a) Virtual torque step to zero.



(b) Rotor flux step to virtual value.

Figure 5.3 (a) Electromagnetic torque, (b) Rotor flux during synchronization.

5.3 Chapter Conclusion

As stated earlier in this chapter, the AC voltage needed from the machine during starting is much higher than the voltage needed in normal operation, thus a synchronism is an important issue to be applied. In this chapter, DVTC was used to synchronize the stator of DFIG and the grid in amplitude, phase, and frequency.

Chapter 6

Low Voltage Ride Through for DFIG

Recently, with the increased demand on wind power, system operators should meet the power grid requirements to maintain safe, stable, and continuous operation of the power generation system. Past grid codes* (e.g first German grid codes for wind energy in 2003) recommended disconnection of the wind turbine system when a voltage dip occurs under 0.8 per unit [131]. Later up from 2007, instead of disconnection, larger wind turbines had to support the electric grid during voltage sags [69]. LVRT is an important challenge for the system operators, especially when a DFIG power system is used. There are many ways to solve the LVRT problem, two modifications of the rotor circuit including the addition of either a silicon-controlled rectifier (SCR) rotor-crowbar circuit or a three-phase rectifier and modulated resistive load to improve in the DFIG ride-through capability [132–134]. In this chapter, different types of grid faults (symmetrical and asymmetrical three-phase dip) are analyzed, and DFIG behavior is discussed as well as LVRT solutions.

6.1 LVRT Grid Codes Requirements for a DFIG Wind Turbine

One of the main drawbacks of DFIG-based wind turbines is the sensitivity to grid disturbances. Older wind turbine systems had to be disconnected from the grid and synchronized again when the grid voltage recovered. The latest grid codes do not allow generator tripping even during severe voltage dips (down to 20 % - 0 % remaining voltage) and request provisioning of high reactive currents only few milliseconds after fault occurrence to support the grid. [135] states that contemporary DFIG based wind turbines are in almost all cases unable to meet rising LVRT and reactive power requirements. The LVRT profile according to the German transmission code [69] is shown in Figure 6.1. The areas in Figure 6.1 denote the following requirements:

- Area 1: 'Three-phase short circuits or symmetrical voltage drops due to disturbances must not lead to instability or to a disconnection of the generating facility from the network' [69].
- Area 2 the following shall apply: All generating facilities shall pass through the fault without being disconnected from the network. Short-time disconnection (with short clearing time) is also allowed by agreement with grid operator if the generator becomes

unstable during grid fault. In this case, re-synchronization should take place for higher than 2 s, and an active power can be increased after clearing the fault to less than 10 % of the nominal value per second [69].

- Area 3: A short-time disconnection of the generating facility from the network is always permitted [69].
- Area 4: The range where only a disconnection through system automatics is admissible (selective disconnection of generators depending on their state) [69]. Moreover, the voltage control should continue supplying the grid by reactive current with at least 2 % of the rated value per percent of the voltage drop when the voltage drops to more than 10 % of the nominal value. The control characteristics are identified in Figure 6.2,

and more

details about the LVRT requirements can be found in [69].

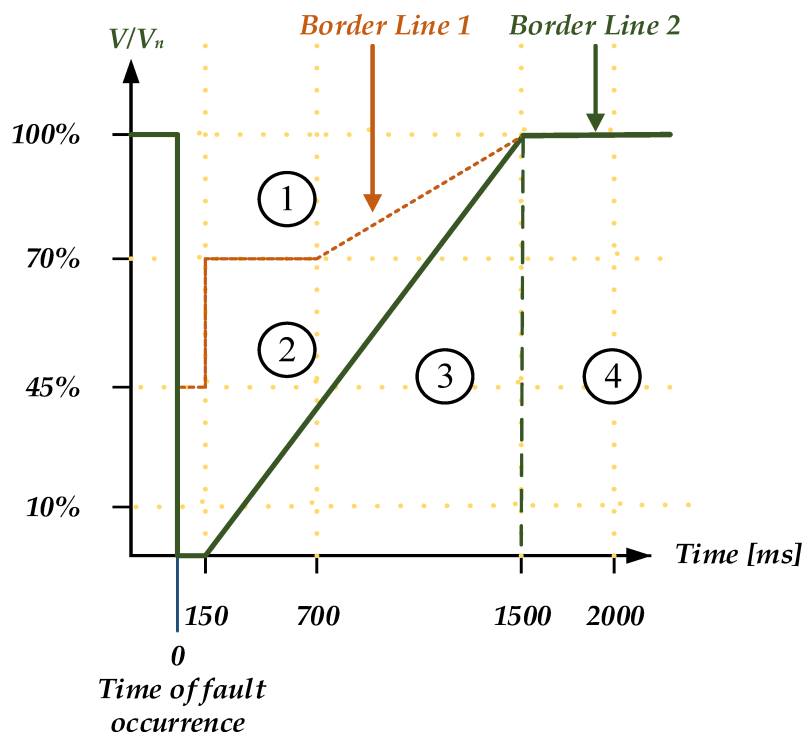


Figure 6.1 Low voltage ride through requirement for German transmission codes (self-designed based on [69]).

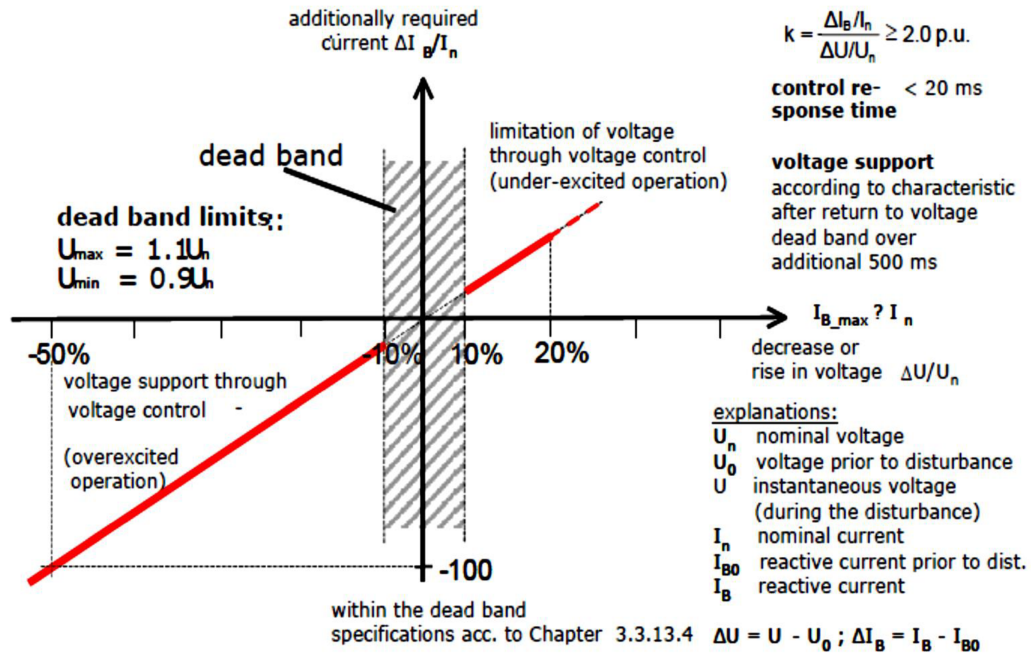


Figure 6.2 Voltage control requirements during grid faults according to the grid codes [69].

6.2 DFIG Under Voltage Dip

Voltage dips appear in the form of:

- Symmetrical three-phase voltage dips.
- Asymmetrical one or two phase voltage dips.

The system used in the analysis is shown in Figure 6.3 and consists of the DFIG, back to back converter with control algorithm, LCL filter, and the voltage sag generator which generates the voltage dip.

6.2.1 Voltage Sag Generator

There are several ways to generate the grid faults, such as transformer-based voltage sag generators, which are described in [136]. A generator-based voltage sag generator using a diesel powered 15 kW SG was presented in [137]. In this case, the cost of the hardware was high due to the weight and scale of the diesel engine and the SG. In [138], another solution to build a voltage sag generator was presented by using a full converter setup. A back-to-back converter was connected between the grid and the load, and all kinds of grid faults could be generated by controlling the load-side

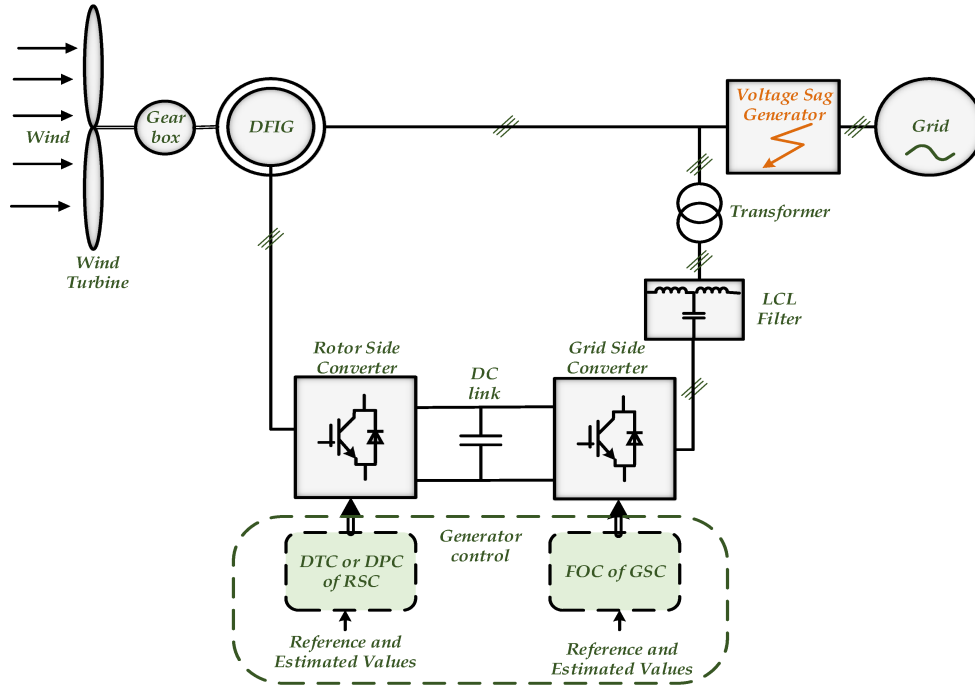


Figure. 6.3 DFIG under voltage dip.

output voltage. The hardware for this method is expensive and complex due to the need of a fully controlled back-to-back converter. An impedance sag generator, which is used in this study, is a very common and effective solution for generating different types of grid faults; the same strategy was used in [139–143]. In a three-phase grid, a number of different fault types can occur, such as single-phase-to-neutral, phase-to-phase, two-phase to-neutral, and three phase faults. As can be seen in Figure 6.4, two impedances series and shunt are designed, permitting testing with different levels of voltage sags. These impedances also present a medium tap, allowing different sag magnitudes. When the switch “ S_1 ” is opened and “ S_2 ” is closed, the currents flowing through Z_2 cause a voltage drop on Z_1 . A voltage sag occurring at the point of common coupling (PCC) as defined in [144] is calculated as:

$$V_{sag} = V_g \left| \frac{Z_2}{(Z_1 + Z_g) + Z_2} \right| \quad (6.1)$$

Here, V_{sag} is the voltage during the sag condition, V_g is the grid voltage before the fault, Z_g is the grid impedance, and Z_1 and Z_2 are the series and shunt impedances.

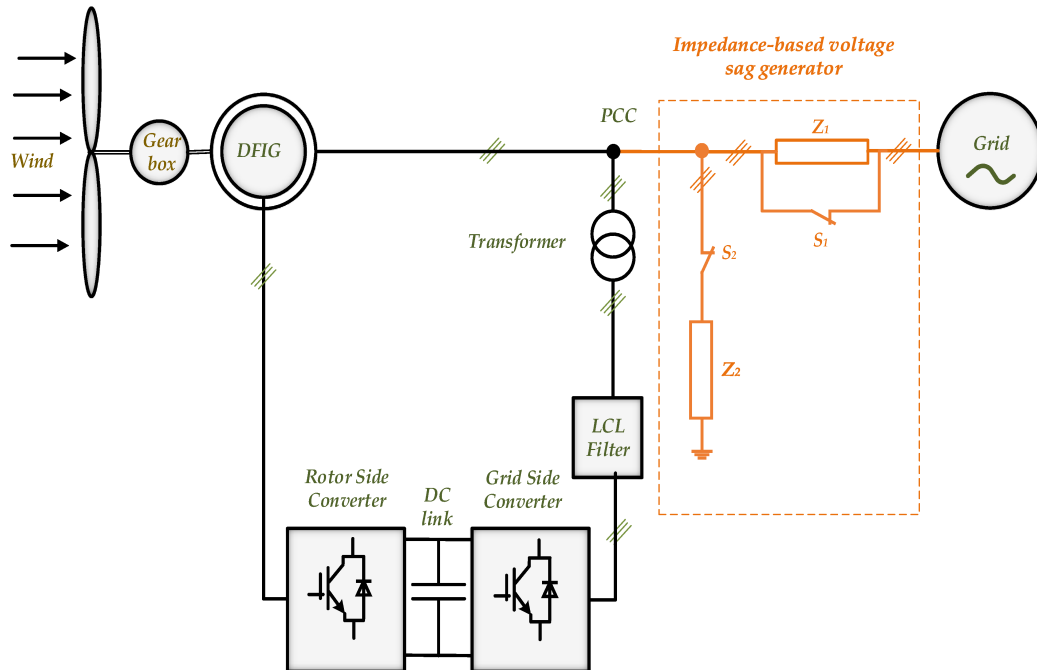


Figure. 6.4 The DFIG system with an impedance sag generator.

6.2.2 DFIG Behavior Under Grid Fault

The dynamic response of the DFIG under three phase, two phase, and single phase voltage dip is illustrated in the following sections. For all cases, 90 % voltage dip (the remaining voltage is 10 % of the nominal grid voltage) is applied by appropriate selection of impedances Z_1 , Z_2 during fault at a time of 1 s and maintained for a duration of 150 ms.

6.2.3 Simulation Results and Discussion

For LVRT analysis, a 2MW DFIG was used under the same conditions as in Section 3.3; 90 % symmetrical and asymmetrical voltage dip is applied on the grid, and the simulation results are discussed.

Three-Phase Grid Fault Three-phase 90 % voltage dip was applied on the grid to study the dynamic behavior of DFIG during the fault without using any protection; the grid voltage in this case is shown in Figure 6.5. The fault was applied at 1 s and maintained for 150 ms. Figure 6.6 demonstrates the performance of rotor voltage and current, in addition to the stator current during voltage dip. From the results, it is obvious that a sudden voltage dip causes rotor over voltage and

current.

Thus the rotor over voltages and currents are not preferred because they could damage the RSC if it is not over dimensioned. And over-dimensioning the converter increases the cost as the IGBT's are thus more expensive.

Rotor and stator fluxes behavior is illustrated in Figures 6.7a and 6.7b; both waveforms have a small increase at the end of the fault duration. The torque during the voltage dip is unstable and having ripples as can be seen in Figure 6.7c.

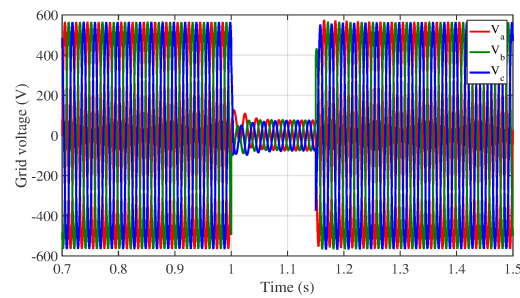
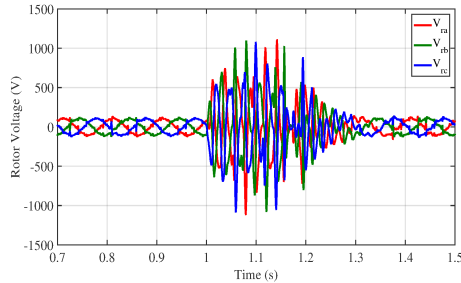
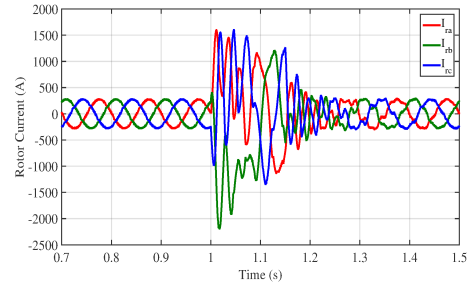


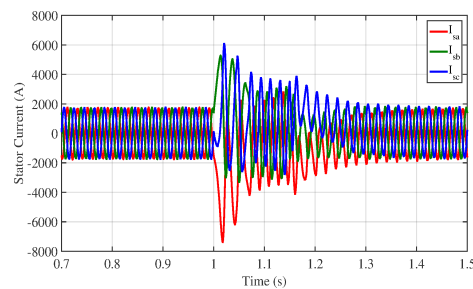
Figure. 6.5 Grid voltage with three-phase 90% voltage dip at time 1 s for 150 ms.



(a)



(b)



(c)

Figure. 6.6 (a) Rotor voltage, (b) Rotor current and (c) Stator current under 90% three-phase voltage dip at time 1 s for 150 ms.

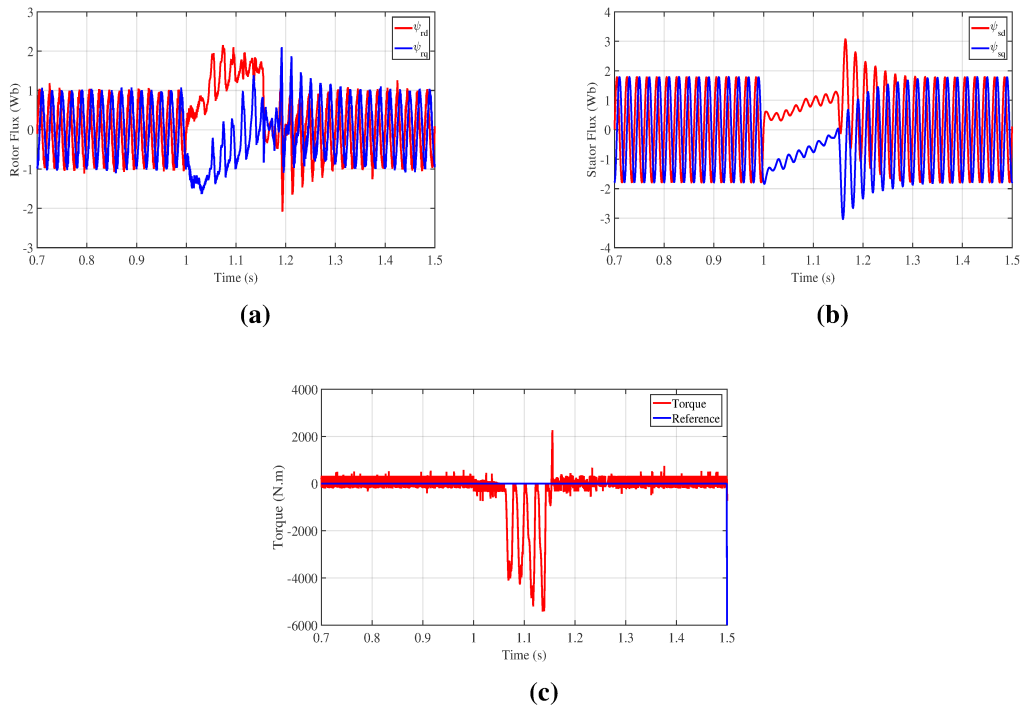


Figure. 6.7 (a) Rotor flux (DQ), (b) Stator flux (DQ) and (c) Electromagnetic torque under 90% three-phase voltage dip at time 1 s for 150 ms.

Two-Phase Grid Fault In this section, asymmetrical 90 % two-phase voltage dip was applied on the grid, as in Figure 6.8.

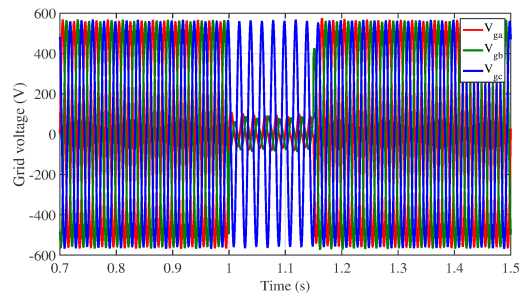


Figure. 6.8 Grid voltage with 90% two-phase voltage dip at time 1 s for 150 ms.

From Figures 6.9 and 6.10, it can be noted that two-phase grid voltage dip causes rotor voltage, rotor current, and stator current to rise during the fault, even though the rotor voltage overshoot is lower (about 350 V) when compared to that in three-phase voltage dip (about 1100 V). In spite of these high values, the waveforms recovered very quickly after a maximum of 100 ms. Figure 6.10 presents the waveforms of rotor flux, stator flux, and electromagnetic torque. As can be seen in the

figure, the rotor flux during voltage dip is increased while the stator flux is decreased, but the torque has a better performance because it has less fluctuations and more stable.

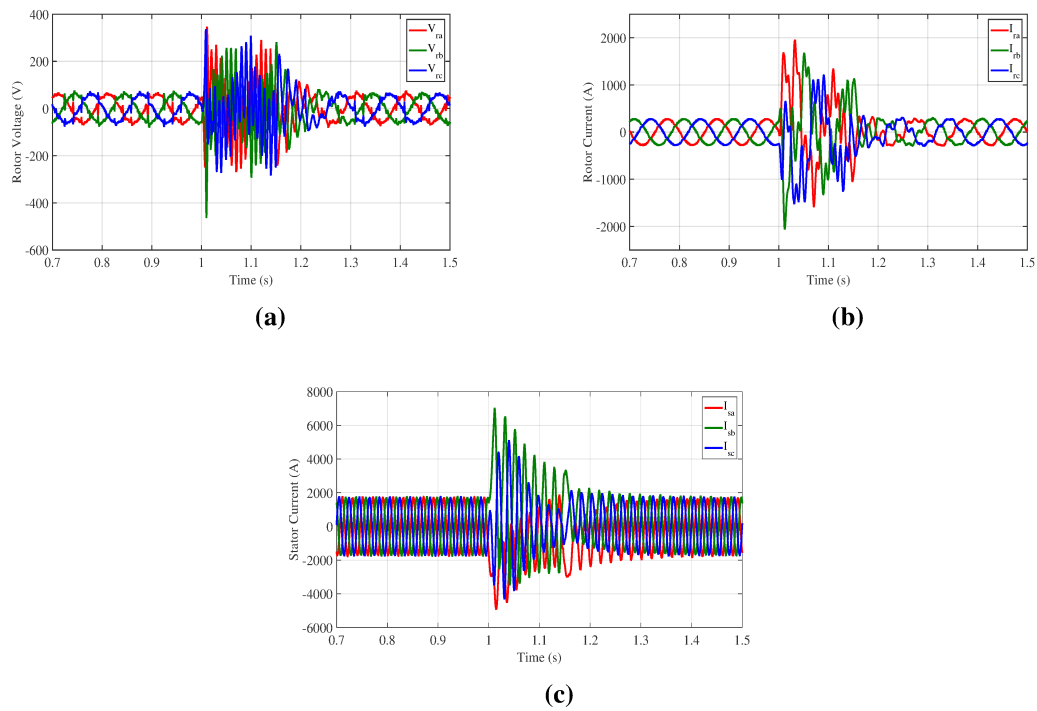


Figure. 6.9 (a) Rotor voltage, (b) Rotor current, and (c) Stator current under 90% two-phase voltage dip at time 1 s for 150 ms.

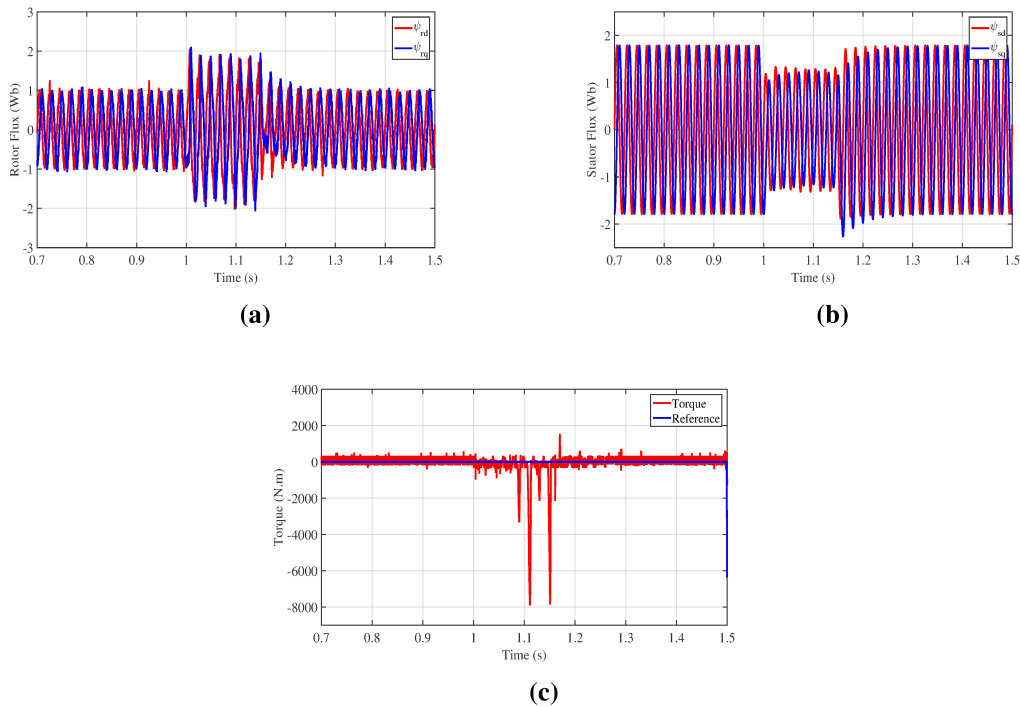


Figure. 6.10 (a) Rotor flux (DQ), (b) Stator flux (DQ), and (c) Electromagnetic torque under 90% two phase voltage dip at time 1 s for 150 ms.

Single-Phase Grid Fault Single-phase 90 % voltage dip of nominal grid voltage was applied to the DFIG system; the grid voltage is shown in Figure 6.11.

Based on the results in Figure 6.12, a grid single-phase fault generates peaks in rotor voltage, rotor current, and stator current amplitudes above the values in nominal operation. Thus, the rotor voltage reaches about 275 V at the moment of fault, four times its nominal value, while the rotor and stator currents rises to 1600 A (4 times the peak value before fault) and 5700 A (3 times the peak value before fault) respectively. Figure 6.13 shows that only the q component of rotor and stator fluxes are affected by the single-phase voltage dip, and the electromagnetic torque does not have a notable change during the voltage dip.

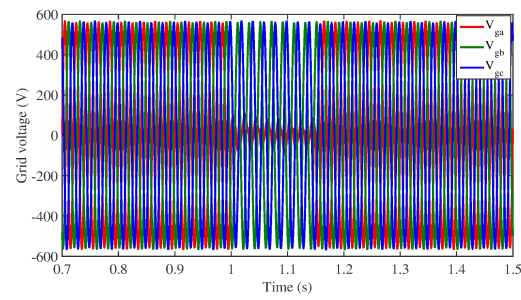


Figure. 6.11 Grid voltage with 90% single phase voltage dip at time 1 s for 150 ms.

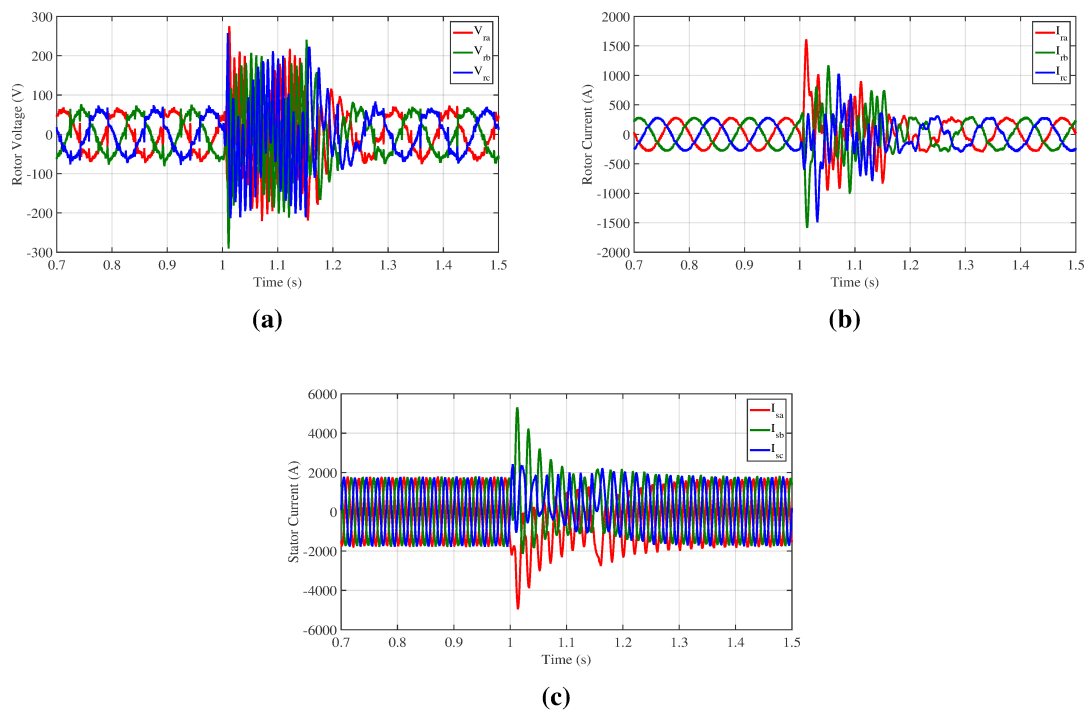


Figure. 6.12 (a) Rotor voltage, (b) Rotor current, and (c) Stator current under 90% single phase voltage dip at time 1 s for 150 ms.

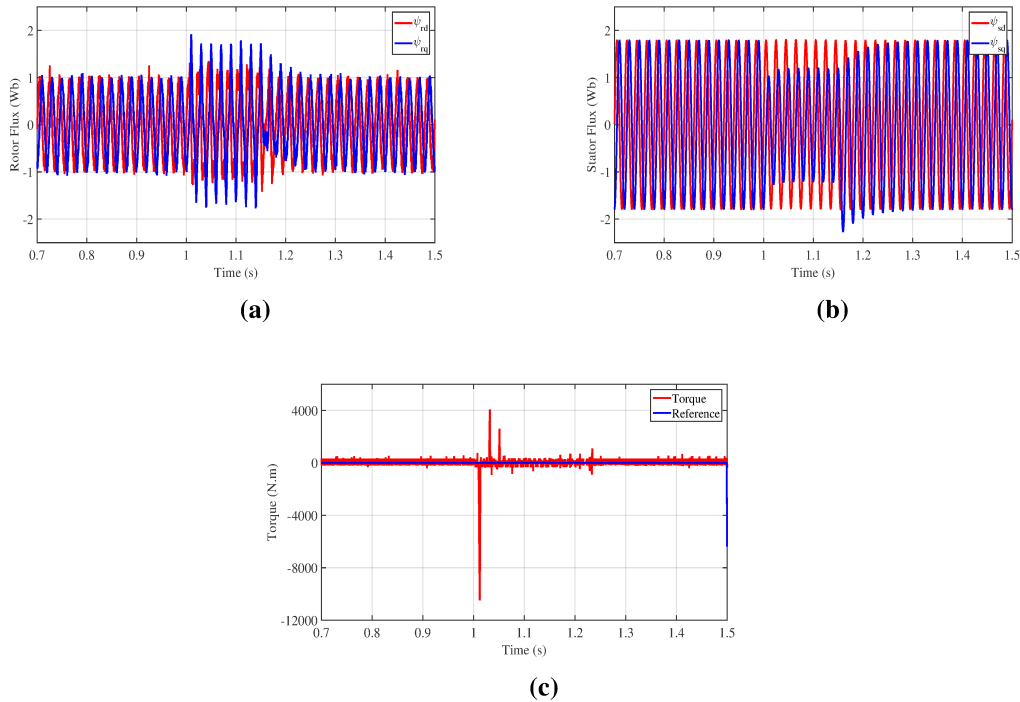


Figure. 6.13 (a) Rotor flux (DQ), (b) Stator flux (DQ), and (c) Electromagnetic torque under 90% single phase voltage dip at time 1 s for 150 ms.

6.3 LVRT Solutions

The problem of the LVRT is the sudden grid voltage changes that lead to over-currents and over-voltages in the rotor windings [72]. These changes can result in loss of control over the machine; severe dips even destroy the back-to-back converter if no countermeasures are taken. Due to the increasing number of DFIG-based wind turbines, it became an important issue to fulfill the LVRT grid-codes requirements. The DFIG system should maintain controlled and stable to avoid any transients of voltages and currents during grid fault. Several approaches have been carried out to find a feasible solution for LVRT capability [43–49, 55, 50, 51]; these strategies can be summarized according to [73] as:

- **DC Chopper:** DC chopper is a power resistor that is connected in parallel with the DC-link capacitor to limit the DC-link over-voltage during voltage dip while the RSC over-currents are blocked by the built in anti-parallel capacitors [73]. This control method does not have any effect on the over-current of the machine rotor circuit [73], thus, it is commonly used with another protection circuit called crowbar (resistance through a

power electronic switch connected to the rotor circuit), which is discussed later in this section.

- **Series Dynamic Braking Resistor:** To limit the rotor over-current, a series dynamic resistor is connected in series with the rotor circuit. Moreover, it can also limit the over-voltage because of its series connection [74].
- **Reverse Current Tracking Method:** The main principle of this topology depends on the limitation that the sum of rotor and stator current vectors equal to the excitation current corresponds to the stator flux, so the rotor current can be controlled by tracking the stator current in the opposite direction [75].
- **Stator Current Feed Back Technique:** This technique is based on modifying the control system in such a way that the rotor current is reduced without adding any hardware to the system. When the fault occurs, the rotor and stator currents are measured and fed back to the rotor current controller as reference. The aim of this control strategy is to reduce stator current oscillations and the rotor currents [76].
- **Flux Linkage Tracking:** The main purpose of this control strategy is to keep the difference between the rotor and stator flux linkage small so that the rotor current does not exceed its maximum allowed value [70].
- **Crowbar Circuit:** This circuit is the conventional method for LVRT [71, 77–79]. In the voltage dip situation, the rotor circuit of DFIG is disconnected, and the machine runs as squirrel cage induction motor. Thus, the crowbar circuit is connected to the rotor circuit and becomes a path for the rotor current, but the DFIG still connected to the grid. This method is chosen as a LVRT solution in this work due to its simplicity, functionality, and low cost. The next section propose the crowbar protection method with a more detailed analysis.

6.3.1 Crowbar Protection

DFIG systems are equipped with a protection called "crowbar" that is connected in parallel between the rotor terminals and the RSC [145, 146]. The design of crowbars and their control systems are an important issue of modern research efforts. The crowbar provides a path for the rotor currents to avoid the high current on the RSC once the converter loses current control. The operation of the crowbar protection system during grid fault can be summarized into the following steps:

- Disconnection of the rotor windings from the RSC.
- Insertion of the three-phase resistance in series to the rotor windings (crowbar system).
- Disconnection of the crowbar system from the rotor windings.
- Reconnection of the RSC to the rotor windings.

Two different configurations are available for the crowbar: passive and active. Both schemes rectify the rotor current and short-circuit the rotor by means of a resistance.

The passive crowbar is constructed with a thyristor and allows closing the circuit but does not allow it to open until the crowbar current is extinguished [147]. The active crowbar, as shown in Figure 6.14, is constructed from an IGBT and allows opening the circuit in forced commutation [12, 148–150]. The crowbar circuit should be activated immediately by the generated pulses trigger. The active crowbar is used in this work.

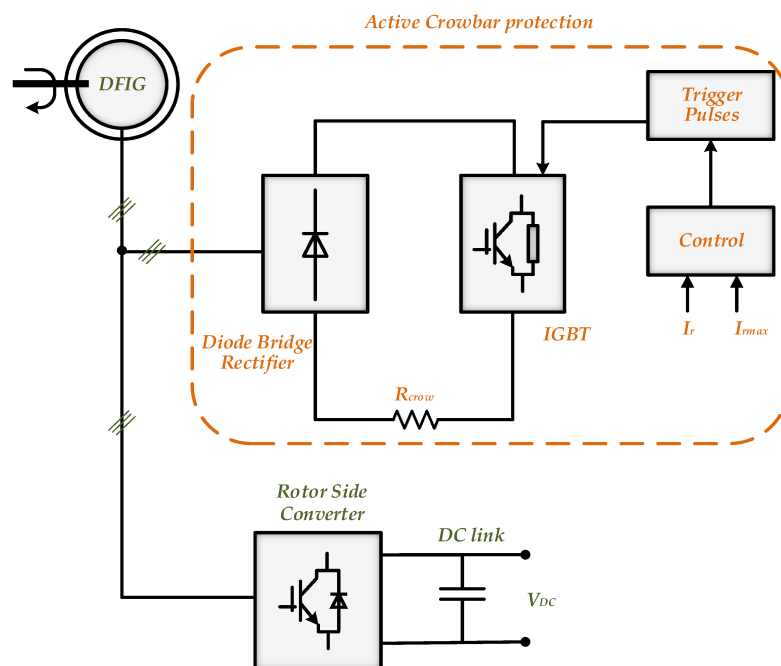


Figure 6.14 Active crowbar protection circuit.

Simulations with using crowbar protection As the dynamic behavior of the DFIG during voltage dip is highly affected by the value of crowbar resistance, it is necessary to choose an appropriate value for it, because small values of crowbar resistances cause high current flowing through the rotor of the machine. Thus, a high electromagnetic torque is generated and may damage the mechanical parts of the machine and the wind turbine. Alternatively, higher values of the crowbar resistances cause higher

rotor voltage, and so may damage the back-to-back converter[66].

To choose the best value of crowbar resistance, different crowbar resistance has been chosen as 20, 50, 100, and 200 times the rotor resistance and simulated as shown in Figure 6.15.

As can be seen in the figure, a crowbar resistance with a value of $200 * R_r$ (the red curve) had the highest peaks in most waveforms. This value is then not preferred as a crowbar resistance because the main purpose of it should be to reduce these peaks. Having a look again to Figure 6.15, it can be concluded that the other curves, which perform $20 * R_r$, $50 * R_r$, and $100 R_r$ have slightly similar effects on damping the peaks of torque, stator flux, and rotor flux. The impact of those resistances is different in rotor voltage and current waveforms. To conclude based on these results, a crowbar resistance of a value $20 * R_r$ can be chosen in the crowbar protection circuit to dampen the rotor over voltage and current to 50 V and 1821 A respectively. The results of 3.5 kW DFIG under three phase voltage dip with and without crowbar protection are presented in Appendix B.2.

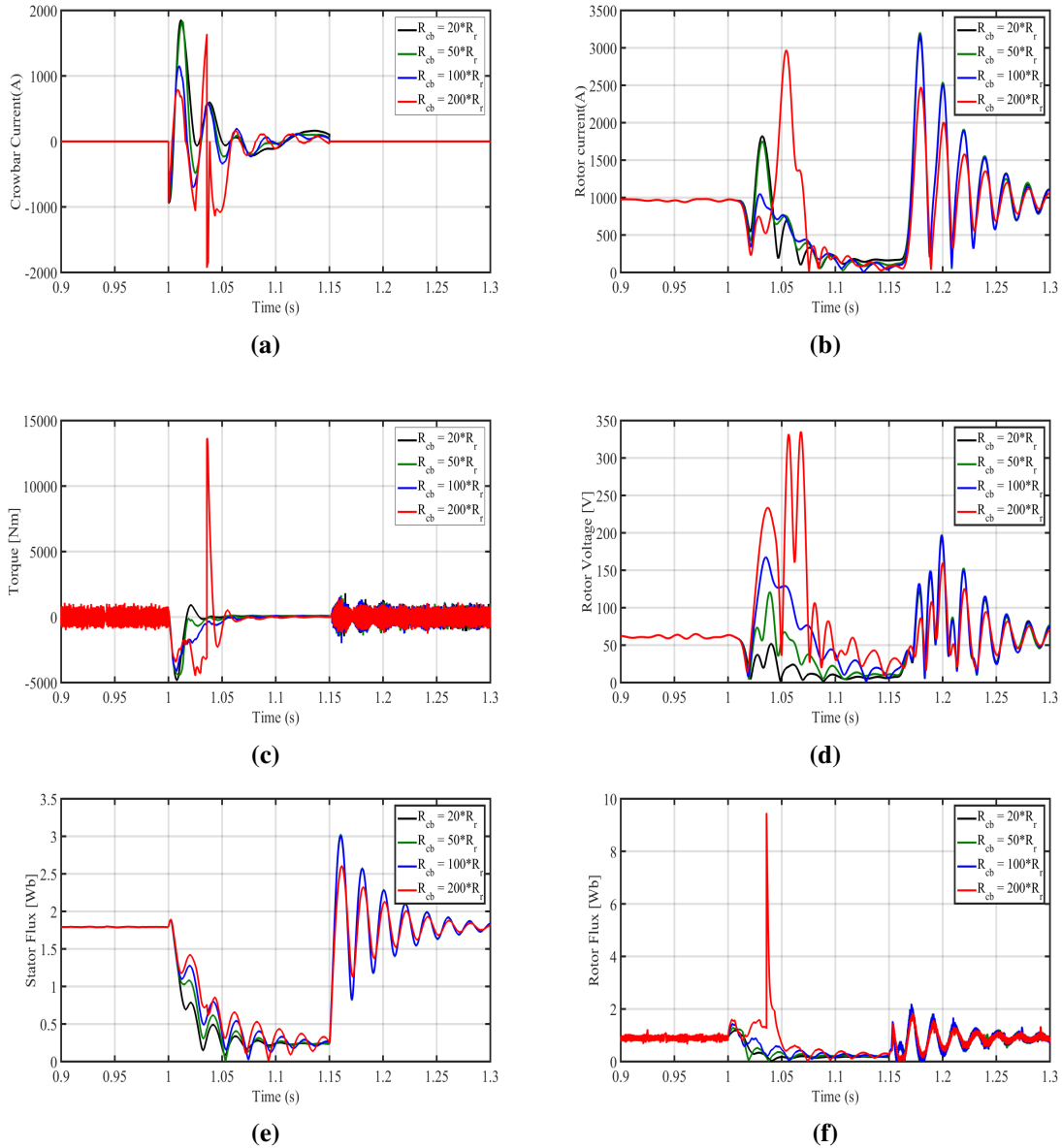


Figure. 6.15 (a) Crowbar current, (b) Rotor current, (c) Electromagnetic torque, (d) Rotor voltage, (e) Stator flux, and (f) Rotor flux during three phase voltage dip using different crowbar resistances.

6.4 Practical Implementation of Impedance Based Voltage Sag Generator for 3.5 kW DFIG

The VSG was used to generate a voltage dip, which should be capable of providing different depths (10 % to 100 %) of the nominal grid voltage to test the generator under LVRT conditions. The impedance-based VSG was built in the lab and the circuit is shown in Figure 6.16a. The switches S_1 and S_2 were contactors (L60 and L84 from ABB), and they were switched using the time relay E1ZM [151]. The output of the time relay that is normally connected to the input, was connected to the coil of the contractor S_1 , and the other was connected to the coil of S_2 , switching them at the same instant as shown in Figure 6.16b. The control input of the relay was connected to 230 V via a button that could be used to trigger the fault. The duration of the fault could be changed directly at the time relay.

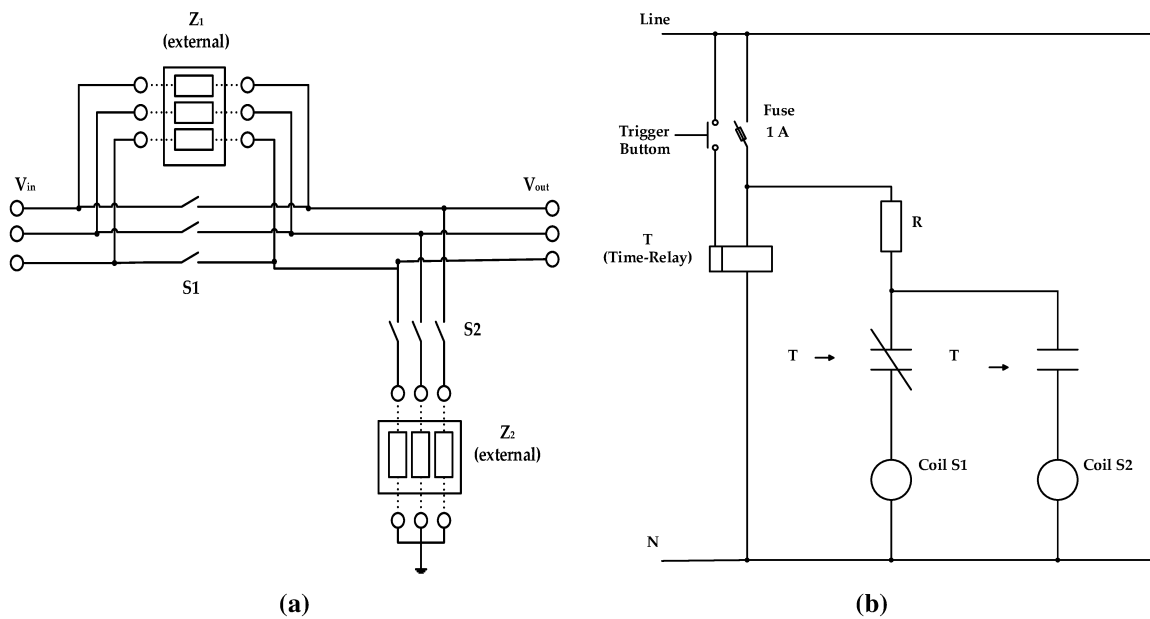


Figure. 6.16 a) Impedance based VSG, b) Coils details.

The operation of impedance based VSG from Figure 6.16 can be summarized as:

- Z_1 and Z_2 worked as voltage divider, according to Equation 6.1.
- A voltage sag was generated when the trigger button is pushed, thus S_1 is opened and S_2 is closed.
- The duration of the fault could be set using the time-relay, in this case (do not change the mode, only the time) after the specified time, the switches were back to their normal

condition: S_1 is closed and S_2 is opened.

- The control circuit had a 1 A fuse.

6.4.1 Fault Detection

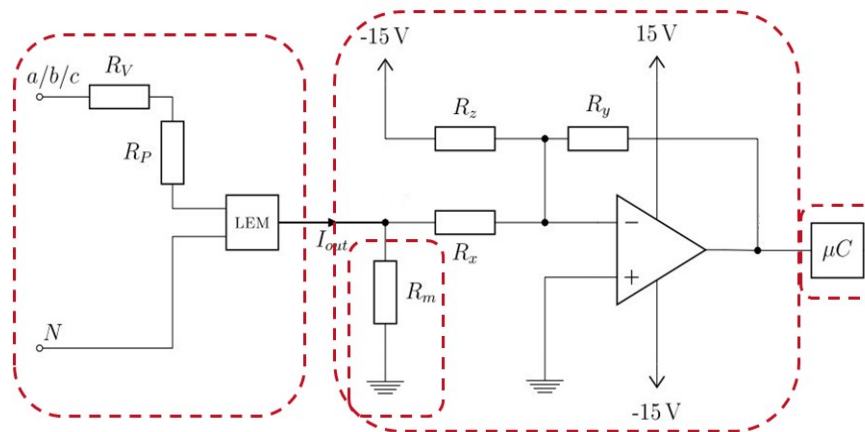


Figure. 6.17 Fault detection circuit.

To detect a fault in reality, it is necessary to know the three phase voltage values. To measure them, the voltage transducer LEM-25p was used; the output is a current that is proportional to the phase voltage. Using a resistor, it is possible to measure a voltage that is proportional to the output current and thus to the measured voltage. The circuit, which can be seen in Figure 6.17, consisted of the voltage transducer (LEM-25p) with all the required resistances (R_v , R_m). R_p is the resistance of the primary windings, which in this case were far smaller than R_v but, for the sake of completeness, are still included in the scheme. Afterwards, the output signal was shifted upwards using an inverting adder consisting of R_x , R_y , R_z and an OPAMP (doing so is possible because the voltage transducer requires -15V as supply). ATMEGA32 was the microcontroller used to give an indication. Because the controller (ATMEGA32) cannot work with negative voltages or voltages that are bigger than 5V, the output signal needed to be manipulated further, for this purpose, an amplifying adder was used. The parameters for the fault detection circuit can be found in A.5.

6.4.2 Circuit Components

For the practical realization of the fault detection circuit, a micro-controller (ATMEGA32) and an OPAMP (LM358 N-P) were printed and soldered onto a PCB. In addition to ATMEGA32 and OPAMP,

the following components were added:

- Zener Diodes to protect the inputs of the μC from over-voltages.
- A voltage regulator to break down the +15V to +5V for the μC .
- Capacitors to stabilize the supply voltages.
- Potentiometer to set the threshold value, at which the circuit outputs an error signal.
- Plug for the ISP-programmer.
- A pull-up resistance between 5 V and the reset-pin of the controller to ensure that it had a fixed potential. The resistances in Figure 6.17 have been calculated to meet the system requirements. The parameters of the fault detection circuit are in A.5.

6.4.3 Test Realization

To evaluate the performance of the components that have been designed in this work, a test of the sag generator and sag detector has been performed. A 3ph-voltage sag of 100% was simulated using a transformer as voltage source, while a squirrel cage induction machine was the load that simulated the inductive load of the DFIG.

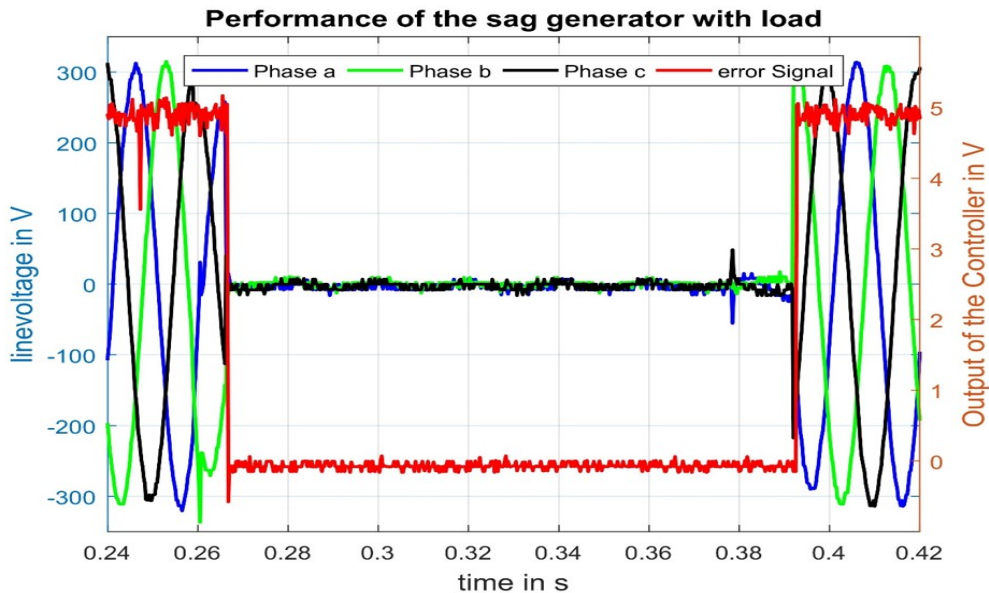


Figure. 6.18 Generation of 100% voltage dip.

The performance of VSG with load is illustrated in Figure 6.18. to evaluate the behavior of the fault detection. Several measurements with the same setup have determined the time the fault detection takes. The result of these tests is that the detection of the fault takes between 0.4ms and

0.75ms, depending on the timing of fault occurrence. With the components that were designed and built in this work, it is now possible to simulate any fault in the grid on the test bench, detect the fault and then activate the crowbar to operate the DFIG as compliant to the grid codes as possible.

6.5 Chapter Conclusion

The LVRT is an important challenge for grid-connected DFIG in wind power generation. DFIG under symmetrical and asymmetrical grid faults were discussed in this chapter; an impedance-based VSG was used to implement the grid fault.

The behavior of DFIG under voltage dip was studied in different fault types, and the results demonstrated that the DFIG performance is affected by the voltage dip, and when the fault occurs, there are over-voltages and over-currents on the rotor circuit, in addition to instability of the electromagnetic torque. The solution of LVRT risk was also handled in this chapter, and the crowbar circuit was chosen. The crowbar protection showed successful performance in reducing the overshoots in voltage, current, flux, and torque. Different values of crowbar resistance were applied, and the results were compared to choose the most suitable value. Thus, a value of $20 * R_r$ was chosen to dampen the overvalues in the waveforms. Finally, VSG realization was presented as well as the fault detection circuit, then, the generation of 100 % 3-phase voltage sag was investigated.

Chapter 7

Conclusion

7.1 Conclusion

This dissertation focuses on the performance of DFIG based wind power generation. The main purpose of this work is to analyze DFIG characteristics with several control strategies. Thus, a comparison between these algorithms was carried out to improve system reliability and achieve better behavior of the machine.

First, a dynamic model of DFIG has been designed in abc , $\alpha\beta$, and dq reference frames to provide better understanding of the machine behavior. Doing so provides the possibility to study the dynamic and steady state effects of the machine under different operating conditions.

DTC has been designed and implemented for the RSC control. The principle of the conventional control algorithm was first established in detail, then another DTC techniques were presented so as to improve the performance and overcome the disadvantages of the conventional method. Thus modified switching table and twelve sectors DTC techniques have been implemented. The simulations have been carried out in the MATLAB/SIMULINK environment, and the characteristics of DFIG for the three DTC algorithms have been discussed and compared to satisfy the best topology depending on torque, flux ripple calculations, and the spectrum analysis of the stator current.

From the analysis of the DTC techniques, it was found that the twelve sectors DTC technique has the lowest torque and flux ripples, and that the THD of the stator current is reduced, so it can be concluded that the twelve sectors DTC has the best output characteristics when compared to the conventional and modified DTC. Moreover, DPC was designed to control the RSC; the active and reactive power waveforms were analyzed and the spectrum waveform of them was presented. Comparing the THD with the DTC techniques, DPC has higher harmonic distortion. As a result, DTC has better performance than DPC.

In this work, FOC was used for GSC control. The main purpose of this control was to achieve unity power factor by controlling the DC-link voltage. The ripple occurred due to switching the IGBT's was eliminated by using LCL filter, the harmonics were successfully removed since the filter parameters have been chosen accurately.

DVTC was proposed for the start-up of the machine, the synchronization process secured equality between stator and grid voltage of amplitude, phase and angle, to provide smooth machine starting. In addition to the direct control techniques, the LVRT problem is the second main contribution of this dissertation. The LVRT effect was deeply explained, the conventional DTC was used in this analysis, several grid faults were discussed, and the results have been obtained. Then different scenarios for LVRT were discussed, the crowbar protection circuit was chosen in this work, and the results were compared for 2 MW DFIG with and without using the crowbar. Thus, it can be concluded that the peaks generated due to the voltage dip can be reduced by connecting crowbar resistances in parallel with the machine rotor circuit.

The main contributions of this dissertation can be summarized as:

- Dynamic modeling and analysis of a DFIG-based wind power generation.
- Analysis and simulation of three different DTC topologies.
- Analysis and simulation of DPC.
- Analysis and simulation of DFIG synchronization.
- Study of LVRT for DFIG with discussion of the problem solutions.

7.2 Future Work

This work covers important subjects concerning the DFIG wind energy system. Nevertheless, there are more aspects that can be recommended for future research, listed as follows:

- Experimental verification of back-to-back converter control including DTC techniques and DPC.
- DPC improvement to eliminate active and reactive power harmonics and oscillation.
- Study of DTC with constant switching frequency by modification of the control algorithm.
- Apply dual DTC in which two switching tables for rotor and stator fluxes vector control are used to control the back-to-back converters.
- There are many interesting points can be investigated associated with the LVRT problem such as:
 - Analysis of additional LVRT solutions such as:
 - Adding additional hardware components: Series dynamic braking resistor or DC breaking chopper.

- Possible modifications on the control system: stator current feedback, reverse current tracking, and flux linkage tracking.
- Include loss calculations for the DFIG to perform a more realistic analysis.

7.3 Associated publications

1. A. Al-Quteimat, A. Roccaforte, and U. Schäfer, “Performance improvement of direct torque control for doubly fed induction generator with 12 sector methodology,” in 2016 IEEE International Conference on Renewable Energy Research and Applications (ICRERA), Birmingham, United Kingdom, Nov. 2016 - Nov. 2016, pp. 242–246.
2. A. Al-Quteimat, C. Niewianda, and U. Schäfer, “Low voltage ride through of doubly fed induction generator in wind power generation using crowbar solution,” in Proceedings, 2017 International Conference on Optimization of Electrical and Electronic Equipment (OPTIM) & 2017 Intl Aegean Conference on Electrical Machines and Power Electronics (ACEMP) : The Cheile Gradistei Fundata Complex, Brasov, Romania, 25-27 May 2017, Brasov, Romania, 2017, pp. 667-674.

References

- [1] A. Bakouri, A. Abbou, H. Mahmoudi, and K. Elyaaloui, "Direct torque control of a doubly fed induction generator of wind turbine for maximum power extraction," in *Proceedings of 2014 International Renewable & Sustainable Energy Conference*, M. Essaïdi and Y. Zaz, Eds. Piscataway, NJ: IEEE, 2014, pp. 334–339.
- [2] R. K. Patel and G. Dyanamina, "Direct torque control of doubly fed induction generator for wind energy conversion system," in *The 8th International Conference on Computing, Communications and Networking Technologies*. Piscataway, NJ: IEEE, 2017, pp. 1–4.
- [3] M. Z. Rifqi Zuber Ahmadi, A. Jidin, M. Azri, K. Rahim, and T. Sutikno, "Improved Torque Control Performance in Direct Torque Control using Optimal Switching Vectors," *International Journal of Power Electronics and Drive Systems (IJPEDS)*, vol. 5, no. 3, p. 441, 2015.
- [4] "GLOBAL WIND REPORT 2014 | GWEC." [Online]. Available: <http://gwec.net/publications/global-wind-report-2/global-wind-report-2014-annual-market-update/#>
- [5] "The world's most used renewable power sources - Power Technology." [Online]. Available: <http://www.power-technology.com/features/featurethe-worlds-most-used-renewable-power-sources-4160168/>
- [6] "The Law of Wind: A Guide to Business and Legal Issues | Stoel Rives LLP." [Online]. Available: <https://www.stoel.com/legal-insights/special-reports/the-law-of-wind>
- [7] Renewable Energy Policy Network for the 21st Century, "Renewables 2017: Global Status Report," Paris.
- [8] Siegfried Heier, *GRID INTEGRATION OF WIND ENERGY: ONSHORE AND OFFSHORE CONVERSION SYSTEMS*, third edition ed. United Kingdom: John Wiley & Sons, Ltd, 2014.
- [9] B. Fox, *Wind power integration: Connection and system operational aspects / Brendan Fox ... [et al.]*, ser. IET power and energy series. London: Institution of Engineering and Technology, 2007, vol. 50.
- [10] C. E. Brown, *World Energy Resources: International Geohydroscience and Energy Research Institute*. Berlin, Heidelberg: Springer Berlin Heidelberg, 2002.
- [11] M. Liserre, R. Cardenas, M. Molinas, and J. Rodriguez, "Overview of Multi-MW Wind Turbines and Wind Parks," *IEEE Transactions on Industrial Electronics*, vol. 58, no. 4, pp. 1081–1095, 2011.
- [12] G. Abad, *Doubly fed induction machine: Modeling and control for wind energy generation / by Gonzalo Abad ... [et al.]*, ser. IEEE Press series on power engineering. Oxford: Wiley-Blackwell, 2011.
- [13] C. M. R. Charles, V. Vinod, and A. Jacob, "Field oriented control of Doubly Fed Induction Generator in wind power system," in *2015 IEEE International Conference on Computational Intelligence and Computing Research*, N. Krishnan, M. Karthikeyan, I. I. C. o. C. I. Research, and Computing, Eds. Piscataway, NJ: IEEE, 2015, pp. 1–5.
- [14] M. El Azzaoui, H. Mahmoudi, C. Ed-dahmani, and K. Boudaraia, "Comparing performance of PI and Sliding Mode in control of grid connected doubly fed induction generator," in *Proceedings of 2016 International Renewable & Sustainable Energy Conference (IRSEC'16)*, M. Essaïdi and Y. Zaz, Eds. Piscataway, NJ: IEEE, 2016, pp. 769–774.

- [15] N. Ullah, M. Asghar Ali, A. Ibeas, and J. Herrera, "Adaptive Fractional Order Terminal Sliding Mode Control of a Doubly Fed Induction Generator-Based Wind Energy System," *IEEE Access*, vol. 5, pp. 21 368–21 381, 2017.
- [16] S. E. Ben Elghali, M. El Hachemi Benbouzid, T. Ahmed-Ali, and J. F. Charpentier, "High-Order Sliding Mode Control of a Marine Current Turbine Driven Doubly-Fed Induction Generator," *IEEE Journal of Oceanic Engineering*, vol. 35, no. 2, pp. 402–411, 2010.
- [17] R. Zhu, Z. Chen, X. Wu, and H. Liu, "High order sliding mode control of doubly-fed induction generator under unbalanced grid faults," in *IECON 2013*. Piscataway, NJ and Piscataway, NJ: IEEE, 2013, pp. 1662–1667.
- [18] S. Mueangngoen and Y. Kumsuwan, "Grid-flux-oriented control and synchronization for a doubly-fed induction generator system," in *TENCON 2017 - 2017 IEEE Region 10 Conference*. IEEE, 11/5/2017 - 11/8/2017, pp. 1257–1262.
- [19] X. Wei, M. Cheng, W. Wang, P. Han, and R. Luo, "Direct Voltage Control of Dual-Stator Brushless Doubly Fed Induction Generator for Stand-Alone Wind Energy Conversion Systems," *IEEE Transactions on Magnetics*, vol. 52, no. 7, pp. 1–4, 2016.
- [20] M. Essaadi, M. Khafallah, A. Saad, A. Hamdoun, and H. Chaikhy, "A comparative analysis between conventionnal and new direct torque control strategies of induction machine," in *2014 Second World Conference on Complex Systems (WCCS)*. Piscataway, NJ and Piscataway, NJ: IEEE, 2014, pp. 350–354.
- [21] A. Adel, A. Refky, S. Abo-Zaid, and M. Elwany, "Torque Ripple Reduction in Direct Torque Control of Induction Motor Drives by Improvement of the Switching Table," *Journal of Multidisciplinary Engineering Science and Technology (JMEST)*, vol. 1, no. 5, pp. 238–243, 2014.
- [22] S. Mondal and D. Kastha, "Improved Direct Torque and Reactive Power Control of a Matrix-Converter-Fed Grid-Connected Doubly Fed Induction Generator," *IEEE Transactions on Industrial Electronics*, vol. 62, no. 12, pp. 7590–7598, 2015.
- [23] J. Mohammadi, S. Vaez-Zadeh, S. Afsharnia, and E. Daryabeigi, "A Combined Vector and Direct Power Control for DFIG-Based Wind Turbines," *IEEE Transactions on Sustainable Energy*, vol. 5, no. 3, pp. 767–775, 2014.
- [24] H. Tao, H. Ma, Y. Wei, Y. Li, and L. Xu, "A Novel Grid Connection Method for DFIG Based on Direct Power Control," in *2016 IEEE Vehicle Power and Propulsion Conference (VPPC)*. Piscataway, NJ and Piscataway, NJ: IEEE, 2016, pp. 1–6.
- [25] H. Lhachimi, Y. Sayouti, and Y. Elkouari, "Direct power control of a DFIG fed by a two level inverter using SVM algorithm," in *MEES'2017*. [Piscataway,NJ] and [Piscataway,NJ]: IEEE, 2017, pp. 12–15.
- [26] L. Li, H. Nian, L. Ding, and B. Zhou, "Direct Power Control of DFIG System Without Phase-Locked Loop Under Unbalanced and Harmonically Distorted Voltage," *IEEE Transactions on Energy Conversion*, vol. 33, no. 1, pp. 395–405, 2018.
- [27] K. Boulaam and A. Boukhelifa, "Fuzzy sliding mode control of DFIG power for a wind conversion system," in *16th International Power Electronics and Motion Control Conference (PEMC), 2014*. Piscataway, NJ: IEEE, 2014, pp. 353–358.

- [28] R. Mahalakshmi, J. Viknesh, R. M. G. V. M. R, and K. S. Thampatty, "Fuzzy Logic based Rotor Side Converter for constant power control of grid connected DFIG," in *PEDES 2016*. [Piscataway, New Jersey]: IEEE, 2016, pp. 1–6.
- [29] K. Belmokhtar, M. L. Doumbia, and K. Agbossou, "Modelling and fuzzy logic control of DFIG based Wind Energy Conversion Systems," in *Proceedings : 2012 IEEE International Symposium on Industrial Electronics*. Piscataway, NJ: IEEE, 2012, pp. 1888–1893.
- [30] G. Cipriani, M. Corpora, V. Di Dio, F. Di Piazza, and A. Sferlazza, "Feedback linearization control of wind turbine equipped with doubly fed induction generator," in *Infrastructures for energy and ICT: opportunities for fostering innovation*, AEIT, Ed. [Piscataway, NJ: IEEE], 2017, pp. 1–6.
- [31] I. Takahashi and T. Noguchi, "A New Quick-Response and High-Efficiency Control Strategy of an Induction Motor," *IEEE Transactions on Industry Applications*, vol. IA-22, no. 5, pp. 820–827, 1986.
- [32] M. Depenbrock, "Direct self-control (DSC) of inverter fed induction machine," in *1987 IEEE Power Electronics Specialists Conference*. IEEE, 6/21/1987 - 6/26/1987, pp. 632–641.
- [33] P. Maciejewski and G. Iwanski, "Direct Torque Control for Autonomous Doubly Fed Induction Machine based DC Generator," in *2017 Twelfth International Conference on Ecological Vehicles and Renewable Energies (EVER)*. [Piscataway, NJ] and [Piscataway, NJ]: IEEE, 2017, pp. 1–6.
- [34] M. E. Zarei, C. Vezinas Nicolas, and J. Rodriguez Arribas, "Improved Predictive Direct Power Control of Doubly Fed Induction Generator During Unbalanced Grid Voltage Based on Four Vectors," *IEEE Journal of Emerging and Selected Topics in Power Electronics*, vol. 5, no. 2, pp. 695–707, 2017.
- [35] A. P. Shah and A. J. Mehta, "Direct power control of grid-connected DFIG using variable gain super-twisting sliding mode controller for wind energy optimization," in *IECON 2017 - 43rd Annual Conference of the IEEE Industrial Electronics Society*. IEEE, 2017, pp. 2448–2454.
- [36] D. Sun, X. Wang, H. Nian, and Z. Q. Zhu, "A Sliding-Mode Direct Power Control Strategy for DFIG Under Both Balanced and Unbalanced Grid Conditions Using Extended Active Power," *IEEE Transactions on Power Electronics*, vol. 33, no. 2, pp. 1313–1322, 2018.
- [37] D. Zhi and L. Xu, "Direct Power Control of DFIG With Constant Switching Frequency and Improved Transient Performance," *IEEE Transactions on Energy Conversion*, vol. 22, no. 1, pp. 110–118, 2007.
- [38] S. Dinesh, R. Meenakshi, M. S. Suhanya, M. S. Kumaran, and R. Muthu, "Modeling and direct power control of DFIG for wind energy conversion system with a back to back converter," in *Proceeding of the IEEE International Conference on Green Computing, Communication and Electrical Engineering (ICGCCEE'14)*, K. Porkumaran and V. K. Chinnaiyan, Eds. [Piscataway, NJ]: IEEE, 2014, pp. 1–6.
- [39] D. Kairous, R. Wamkeue, and M. Ouhrouche, "Second order sliding-mode for direct power control of DFIG under distorted grid," in *2015 IEEE International Conference on Smart Energy Grid Engineering (SEGE)*. IEEE / Institute of Electrical and Electronics Engineers Incorporated, 2015, pp. 1–6.

- [40] M. T. Hagh, S. Roozbehani, F. Najaty, S. Ghaemi, Y. Tan, and K. M. Muttaqi, "Direct power control of DFIG based wind turbine based on wind speed estimation and particle swarm optimization," in *2015 Australasian Universities Power Engineering Conference (AUPEC)*. Piscataway, NJ: IEEE, 2015, pp. 1–6.
- [41] R. Errouissi, A. Al-Durra, S. M. Muyeen, S. Leng, and F. Blaabjerg, "Offset-Free Direct Power Control of DFIG Under Continuous-Time Model Predictive Control," *IEEE Transactions on Power Electronics*, vol. 32, no. 3, pp. 2265–2277, 2017.
- [42] A. P. Shah and A. J. Mehta, "Direct Power Control of DFIG using Super-Twisting Algorithm based on Second-Order Sliding Mode Control," in *2016 14th International Workshop on Variable Structure Systems (VSS)*. Piscataway, NJ: IEEE, 2016, pp. 136–141.
- [43] Y. Shen, B. Zhang, T. Cui, J. Zuo, F. Shen, and D. Ke, "Novel Control of DFIG with ESD to Improve LVRT Capability and to Perform Voltage Support during Grid Faults," in *ICEI 2017*, J. Cao and I. I. C. o. E. Internet, Eds. Piscataway, NJ: IEEE, 2017, pp. 136–141.
- [44] M. Firouzi and G. B. Gharehpetian, "LVRT Performance Enhancement of DFIG-Based Wind Farms by Capacitive Bridge-Type Fault Current Limiter (CBFCL)," *IEEE Transactions on Sustainable Energy*, p. 1, 2017.
- [45] X. An-cheng, G. Fei, Y. Yu-tin, L. Ping, Yang-Yang, and S. Shi, "Research on the Improvement of LVRT ability of An actual DFIG-type wind farm with Crowbar and SVG," in *International Conference on Renewable Power Generation (RPG 2015)*. [Stevenage, United Kingdom]: Institution of Engineering and Technology, 2015?, p. 5.
- [46] M. Q. Duong and G. N. Sava, "Coordinated reactive power control of DFIG to improve LVRT characteristics of FSIG in wind turbine generation," in *2017 International Conference on Electromechanical and Power Systems (SIELMEN)*, D. D. Lucache, Ed. [Piscataway, New Jersey]: IEEE, 2017, pp. 256–260.
- [47] F. Rehman, B. Azeem, C. A. Mehmood, S. M. Ali, B. Khan, and F. Rehman, "Control of Grid Interfaced Doubly Fed Induction Generator (DFIG) Using Adaptive SMC Improved with LVRT Enhancement," in *14th International Conference on Frontiers of Information Technology*, I. C. o. F. o. I. Technology, Ed. Piscataway, NJ: IEEE, 2016, pp. 336–341.
- [48] M. Reddak, A. Berdai, A. Gourma, and A. Nouaiti, "Nonlinear control strategy for wind turbine based on DFIG to enhance the LVRT capability," in *Proceedings of 2016 International Renewable & Sustainable Energy Conference (IRSEC'16)*, M. Essaïdi and Y. Zaz, Eds. Piscataway, NJ: IEEE, 2016, pp. 520–524.
- [49] X. Zheng and X. Chen, "Enhancement on transient stability of LVRT of DFIG based on neural network D-STATCOM and crowbar," in *Proceedings of 2017 11th IEEE International Conference on Anti-counterfeiting, Security, and Identification (ASID)*, J. Zhou, D. Guo, and J. Dong, Eds. [Piscataway, New Jersey]: IEEE Press, 2017, pp. 64–68.
- [50] Y. Chang and X. Kong, "Linear demagnetizing strategy of DFIG-based WTs for improving LVRT responses," *The Journal of Engineering*, vol. 2017, no. 13, pp. 2287–2291, 2017.
- [51] H. Ma, L. Xu, Y. Li, Z. Zheng, and L. Peng, "Direct power control of doubly-fed-induction-generator-based wind turbines under asymmetrical grid voltage dips," in *IEEE Energy Conversion Congress and Exposition (ECCE), 2012*. Piscataway, NJ: IEEE, 9/15/2012 - 9/20/2012, pp. 787–792.

- [52] X. Zheng and G. Xu, "Study on LVRT of DFIG under the asymmetric grid voltage based on fuzzy PID D-STATCOM," in *Proceedings of 2016 IEEE Advanced Information Management, Communicates, Electronic and Automation Control Conference (IMCEC 2016)*, B. Xu, Ed. Piscataway, NJ: IEEE Press, 2016, pp. 237–242.
- [53] Y. M. Alsmadi, L. Xu, F. Blaabjerg, A. Pina Ortega, A. Y. Abdelaziz, A. Wang, and Z. Al-bataineh, "Detailed Investigation and Performance Improvement of the Dynamic Behavior of Grid-Connected DFIG-Based Wind Turbines under LVRT Conditions," *IEEE Transactions on Industry Applications*, p. 1, 2018.
- [54] G. Rashid and M. H. Ali, "Nonlinear Control-Based Modified BFCL for LVRT Capacity Enhancement of DFIG-Based Wind Farm," *IEEE Transactions on Energy Conversion*, vol. 32, no. 1, pp. 284–295, 2017.
- [55] A. Uphues, K. Notzold, R. Wegener, and S. Soter, "DFIG's virtual resistance demagnetization for crowbar less LVRT," in *2017 IEEE 12th International Conference on Power Electronics and Drive Systems (IEEE PEDS 2017)*, I. PEDS, Ed. [Piscataway, NJ]: IEEE, 2017, pp. 265–270.
- [56] M. R. A. Kashkooli, S. M. Madani, and R. Sadeghi, "Improved Direct Torque Control of DFIG with reduced torque and flux ripples at constant switching frequency," in *2016 7th Power Electronics and Drive Systems Technologies Conference (PEDSTC)*. IEEE, 2/16/2016 - 2/18/2016, pp. 58–63.
- [57] M. Mokhtari and S. A. Davari, "Predictive torque control of DFIG with torque ripple reduction," in *2016 IEEE International Conference on Power and Energy (PECon)*. IEEE, 11/28/2016 - 11/29/2016, pp. 763–768.
- [58] A. Gundavarapu, H. Misra, and A. K. Jain, "Direct Torque Control Scheme for DC Voltage Regulation of the Standalone DFIG-DC System," *IEEE Transactions on Industrial Electronics*, vol. 64, no. 5, pp. 3502–3512, 2017.
- [59] L. Xu and P. Cartwright, "Direct Active and Reactive Power Control of DFIG for Wind Energy Generation," *IEEE Transactions on Energy Conversion*, vol. 21, no. 3, pp. 750–758, 2006.
- [60] Y. N. Tatte and M. V. Aware, "Torque Ripple and Harmonic Current Reduction in a Three-Level Inverter-Fed Direct-Torque-Controlled Five-Phase Induction Motor," *IEEE Transactions on Industrial Electronics*, vol. 64, no. 7, pp. 5265–5275, 2017.
- [61] Y. Ren and Z. Q. Zhu, "Reduction of Both Harmonic Current and Torque Ripple for Dual Three-Phase Permanent-Magnet Synchronous Machine Using Modified Switching-Table-Based Direct Torque Control," *IEEE Transactions on Industrial Electronics*, vol. 62, no. 11, pp. 6671–6683, 2015.
- [62] S. Kaboli, M. R. Zolghadri, and E. Vahdati-Khajeh, "A Fast Flux Search Controller for DTC-Based Induction Motor Drives," *IEEE Transactions on Industrial Electronics*, vol. 54, no. 5, pp. 2407–2416, 2007.
- [63] B. El Badsı, B. Bouzidi, and A. Masmoudi, "DTC Scheme for a Four-Switch Inverter-Fed Induction Motor Emulating the Six-Switch Inverter Operation," *IEEE Transactions on Power Electronics*, vol. 28, no. 7, pp. 3528–3538, 2013.
- [64] Y. Zhang, J. Zhu, Z. Zhao, W. Xu, and D. G. Dorrell, "An Improved Direct Torque Control for Three-Level Inverter-Fed Induction Motor Sensorless Drive," *IEEE Transactions on Power Electronics*, vol. 27, no. 3, pp. 1502–1513, 2012.

- [65] J.-W. Kang and S.-K. Sul, "Analysis and prediction of inverter switching frequency in direct torque control of induction machine based on hysteresis bands and machine parameters," *IEEE Transactions on Industrial Electronics*, vol. 48, no. 3, pp. 545–553, 2001.
- [66] A. Al-Quteimat, A. Roccaforte, and U. Schafer, "Performance improvement of direct torque control for doubly fed induction generator with 12 sector methodology," in *2016 IEEE International Conference on Renewable Energy Research and Applications (ICRERA)*. IEEE, 11/20/2016 - 11/23/2016, pp. 242–246.
- [67] C. Lascu, S. Jafarzadeh, M. S. Fadali, and F. Blaabjerg, "Direct Torque Control With Feedback Linearization for Induction Motor Drives," *IEEE Transactions on Power Electronics*, vol. 32, no. 3, pp. 2072–2080, 2017.
- [68] Y. Kwak, J.-W. Ahn, and D.-H. Lee, "A DTC-PWM control scheme of PMSM based on 12-sectors division and speed information," in *The 2014 International Power Electronics Conference - ECCE ASIA - IPEC-Hiroshima 2014*. [Piscataway, N.J.]: IEEE, 2014, pp. 2693–2699.
- [69] Verband der Netzbetreiber – VDN, "Network and System Rules of the German Transmission System Operators: Transmission Code 2007," August 2007.
- [70] S. Xiao, G. Yang, H. Zhou, and H. Geng, "An LVRT Control Strategy Based on Flux Linkage Tracking for DFIG-Based WECS," *IEEE Transactions on Industrial Electronics*, vol. 60, no. 7, pp. 2820–2832, 2013.
- [71] M. Q. Duong, H. H. Nguyen, K. H. Le, T. V. Phan, and M. Mussetta, "Simulation and performance analysis of a new LVRT and damping control scheme for DFIG wind turbines," in *ICSET 2016*, I. I. C. o. S. E. Technologies, Ed. [Piscataway, NJ]: IEEE, 2016, pp. 288–293.
- [72] S. Hu, X. Lin, Y. Kang, and X. Zou, "An Improved Low-Voltage Ride-Through Control Strategy of Doubly Fed Induction Generator During Grid Faults," *IEEE Transactions on Power Electronics*, vol. 26, no. 12, pp. 3653–3665, 2011.
- [73] D. S and K. K. T, "Combination of super capacitor-switch type fault current limiter for LVRT enhancement of DFIG wind turbines," in *2015 International Conference on Control, Communication & Computing India (ICCC)*, C. & C. I. International Conference on Control, Ed. [Piscataway, NJ]: IEEE, 2015, pp. 343–348.
- [74] J. Yang, J. E. Fletcher, and J. O'Reilly, "A Series-Dynamic-Resistor-Based Converter Protection Scheme for Doubly-Fed Induction Generator During Various Fault Conditions," *IEEE Transactions on Energy Conversion*, vol. 25, no. 2, pp. 422–432, 2010.
- [75] H. Qingjun, S. Mucun, Z. Xudong, T. Li, X. Wei, and C. Jianqing, "A reverse current tracking based LVRT strategy for doubly fed induction generator (DFIG)," in *IECON 2013*. Piscataway, NJ and Piscataway, NJ: IEEE, 2013, pp. 7295–7300.
- [76] C. Wessels and F. W. Fuchs, "Fault ride through of DFIG wind turbines during symmetrical voltage dip with crowbar or stator current feedback solution," in *IEEE Energy Conversion Congress and Expo*. [Piscataway, N.J.]: IEEE, 2010, pp. 2771–2777.
- [77] S. Yang, T. Zhou, L. Chang, Z. Xie, and X. Zhang, "Analytical Method for DFIG Transients During Voltage Dips," *IEEE Transactions on Power Electronics*, vol. 32, no. 9, pp. 6863–6881, 2017.

- [78] J.-Y. Ruan, Z.-X. Lu, Y. Qiao, and Y. Min, "Analysis on Applicability Problems of the Aggregation-Based Representation of Wind Farms Considering DFIGs' LVRT Behaviors," *IEEE Transactions on Power Systems*, vol. 31, no. 6, pp. 4953–4965, 2016.
- [79] H. Wen and S. Cai, "Modeling and LVRT analysis of DFIG wind power system," in *Proceedings of the 2015 IEEE PES Asia-Pacific Power and Energy Engineering Conference (APPEEC)*, I. P. APPEEC, Ed. Piscataway, NJ: IEEE, 2015, pp. 1–5.
- [80] A. Petersson, "Analysis, modeling and control of doubly-fed induction generators for wind turbines," Thesis (Ph.D.), CHALMERS UNIVERSITY OF TECHNOLOGY, Göteborg, 2005.
- [81] B. Wu, *Power conversion and control of wind energy systems*, ser. IEEE Press series on power engineering 29. Oxford: Wiley-Blackwell, 2011.
- [82] N. P. Quang and J.-A. Dittrich, *Vector control of three-phase AC machines: System development in the practice*, ser. Power systems. Berlin: Springer, 2008.
- [83] A. E. Fitzgerald, C. Kingsley, and S. D. Umans, *Electric machinery*, 6th ed., ser. McGraw-Hill series in electrical and computer engineering. Boston, Mass. [u.a.]: McGraw-Hill, 2009.
- [84] E. Clarke, *Circuit Analysis of A-C Power Systems*. S.I.: John Wiley & Sons, 1943.
- [85] R. H. Park, "Abridgment of two-reaction theory of synchronous machines generalized method of analysis — Part I," *Journal of the A.I.E.E.*, vol. 48, no. 3, p. 194, 1929.
- [86] G. Bartolini, A. Pisano, and P. Pisu, "Simplified exponentially convergent rotor resistance estimation for induction motors," *IEEE Transactions on Automatic Control*, vol. 48, no. 2, pp. 325–330, 2003.
- [87] Kalyan P. Gokhale, Douglas W. Karraker, Samuli J. Heikkilä, "Controller for a Wound Rotor Slip Ring Induction Machine: Patent," Patent US6 448 735B1, 2002.
- [88] "Direct Torque Control Simulink." [Online]. Available: <https://de.mathworks.com/help/physmod/sps/powersys/ref/directtorquecontroller.html>
- [89] D. Sun and X. Wang, "Low-Complexity Model Predictive Direct Power Control for DFIG under both Balanced and Unbalanced Grid Conditions," *IEEE Transactions on Industrial Electronics*, p. 1, 2016.
- [90] T. Barisa, D. Sumina, and M. Kutija, "Control of generator- and grid-side converter for the interior permanent magnet synchronous generator," in *4th The International Conference on Renewable Energy Research and Applications (ICRERA 2015)*. [Piscataway, NJ] and [Piscataway, NJ]: IEEE, 2015, pp. 1015–1020.
- [91] K. Yu, W. Xu, Y. Liu, and J. Gao, "Improved vector control for stand-alone brushless doubly-fed induction generator," in *IECON 2017 - 43rd Annual Conference of the IEEE Industrial Electronics Society*. IEEE, 2017, pp. 274–279.
- [92] M. S. KP, J. Peter, and R. Ramchand, "Space vector based synchronized PWM strategies for field oriented control of VSI fed induction motor," in *PEDES 2016*. [Piscataway, New Jersey]: IEEE, 2016, pp. 1–5.
- [93] D. Wang, P. Zhang, Y. Jin, M. Wang, G. Liu, and M. Wang, "Influences on Output Distortion in Voltage Source Inverter Caused by Power Devices' Parasitic Capacitance," *IEEE Transactions on Power Electronics*, vol. 33, no. 5, pp. 4261–4273, 2018.

- [94] H. Xu, W. Yao, and S. Shao, "Improved SVPWM schemes for vienna rectifiers without current distortion," in *ECCE 2017*. Piscataway, NJ and Piscataway, NJ: IEEE, 2017, pp. 3410–3414.
- [95] M. Alizadeh Bidgoli, A. Soori, and M. Tavakoli Bina, "A new phase sequence detector for the three-phase rotary loads," in *2011 2nd Power Electronics, Drive Systems and Technologies Conference*. Piscataway: IEEE, Feb. 2011, pp. 529–533.
- [96] M. V. Reddy and R. Sodhi, "A robust frequency estimator for single-phase microgrid applications," in *2017 IEEE Power & Energy Society General Meeting*. [Piscataway, NJ] and [Piscataway, NJ]: IEEE, 2017, pp. 1–5.
- [97] B. P. McGrath, D. G. Holmes, and J. Galloway Galloway, "Power Converter Line Synchronization Using a Discrete Fourier Transform (DFT) Based on a Variable Sample Rate," *IEEE Transactions on Power Electronics*, vol. 20, no. 4, pp. 877–884, 2005.
- [98] J. M. Schellekens, J. L. Duarte, H. Huisman, and M. A. M. Hendrix, "Elimination of zero-crossing distortion for high-precision amplifiers," in *Proceedings IECON 2011*. Piscataway, NJ: IEEE, 2011, pp. 3370–3375.
- [99] Q. Nasir and K. A. Mezher, "Time to digital conversion zero crossing DPLL (TDC-ZCDPLL)," in *Information and Communication Technology Research (ICTRC), 2015 International Conference on*. Piscataway, NJ: IEEE, 2015, pp. 104–107.
- [100] M. P. Kaźmierkowski, R. Krishnan, and F. Blaabjerg, *Control in power electronics: Selected problems / editors, Marian P. Kazmierkowski, R. Krishnan, Frede Blaabjerg*, ser. Academic Press series in engineering. Amsterdam and New York: Academic Press, 2002.
- [101] F. Blaabjerg, R. Teodorescu, M. Liserre, and A. V. Timbus, "Overview of Control and Grid Synchronization for Distributed Power Generation Systems," *IEEE Transactions on Industrial Electronics*, vol. 53, no. 5, pp. 1398–1409, 2006.
- [102] J. Ma, Y. Qiu, Y. Li, W. Zhang, Z. Song, and J. S. Thorp, "Research on the Impact of DFIG Virtual Inertia Control on Power System Small-Signal Stability Considering the Phase-Locked Loop," *IEEE Transactions on Power Systems*, vol. 32, no. 3, pp. 2094–2105, 2017.
- [103] M. Wan and J. Hu, "Modal analysis of a grid-connected DFIG-based WT considering multi-timescale control interactions," *The Journal of Engineering*, vol. 2017, no. 13, pp. 1118–1123, 2017.
- [104] A. Timbus, M. Liserre, R. Teodorescu, and F. Blaabjerg, "Synchronization Methods for Three Phase Distributed Power Generation Systems. An Overview and Evaluation," in *2005 IEEE 36th Annual Power Electronic Specialists Conference (PESC)*. Piscataway, N.J.: Institute of Electrical and Electronics Engineers, 2005, pp. 2474–2481.
- [105] J. A. Suul, K. Ljokelsoy, T. Midtsund, and T. Undeland, "Synchronous Reference Frame Hysteresis Current Control for Grid Converter Applications," *IEEE Transactions on Industry Applications*, vol. 47, no. 5, pp. 2183–2194, 2011.
- [106] W. Luo, J. Jiang and H. Liu, "Frequency-Adaptive Modified Comb-Filter-Based Phase-Locked Loop for a Doubly-Fed Adjustable-Speed Pumped-Storage Hydropower Plant under Distorted Grid Conditions," *Energies*, vol. 10, no. 6, p. 737, 2017.
- [107] S. Golestan, M. Monfared, F. D. Freijedo, and J. M. Guerrero, "Advantages and Challenges of a Type-3 PLL," *IEEE Transactions on Power Electronics*, vol. 28, no. 11, pp. 4985–4997, 2013.

- [108] K. Ogata, *Modern control engineering*, 5th ed. Boston and London: Pearson, 2010.
- [109] L. Alhmoud, "Reliability improvement for high-power IGBT in wind energy applications," *IEEE Transactions on Industrial Electronics*, p. 1, 2018.
- [110] C. Dirscherl and C. M. Hackl, "Model predictive current control with analytical solution and integral error feedback of doubly-fed induction generators with LC filter," in *PRECEDE 2017*. [Piscataway, New Jersey]: IEEE, 2017, pp. 25–30.
- [111] R. Sankar, R. Rajarajan, P. Aravindan, and S. Shobana, "Maximum power extraction in grid connected DFIG using multilevel inverter," in *2012 International Conference on Emerging Trends in Electrical Engineering and Energy Management*. [Place of publication not identified]: IEEE, 2012, pp. 411–416.
- [112] Y. Song, F. Blaabjerg, and X. Wang, "Analysis and comparison of high frequency resonance in small and large scale DFIG system," in *ECCE 2016*. [Piscataway, New Jersey]: IEEE, 2016, pp. 1–8.
- [113] Y. Song and F. Blaabjerg, "Overview of DFIG-Based Wind Power System Resonances Under Weak Networks," *IEEE Transactions on Power Electronics*, vol. 32, no. 6, pp. 4370–4394, 2017.
- [114] D. Zhou, F. Blaabjerg, T. Franke, M. Tonnes, and M. Lau, "Reduced Cost of Reactive Power in Doubly Fed Induction Generator Wind Turbine System With Optimized Grid Filter," *IEEE Transactions on Power Electronics*, vol. 30, no. 10, pp. 5581–5590, 2015.
- [115] M. Liserre, F. Blaabjerg, and S. Hansen, "Design and Control of an LCL-Filter-Based Three-Phase Active Rectifier," *IEEE Transactions on Industry Applications*, vol. 41, no. 5, pp. 1281–1291, 2005.
- [116] P. Zhan, W. Lin, J. Wen, M. Yao, and N. Li, "Design of LCL filters for the back-to-back converter in a Doubly Fed Induction Generator," in *2012 IEEE Innovative Smart Grid Technologies - Asia*, I. Staff, Ed. [Place of publication not identified]: IEEE, 2012, pp. 1–6.
- [117] A. Reznik, M. G. Simoes, A. Al-Durra, and S. M. Mueeen, "LCL filter design and performance analysis for small wind turbine systems," in *2012 IEEE Power Electronics and Machines in Wind Applications*. Piscataway, NJ and Piscataway, NJ: IEEE, 2012, pp. 1–7.
- [118] S. Tahir, J. Wang, M. Baloch, and G. Kaloi, "Digital Control Techniques Based on Voltage Source Inverters in Renewable Energy Applications: A Review," *Electronics*, vol. 7, no. 2, p. 18, 2018.
- [119] Verlags- und Wirtschaftsgesellschaft der Elektrizitätswerke m.b.H.—VWEW, "Eigenerzeugungsanlagen am mittelspannungsnetz," Frankfurt, Germany, 1998.
- [120] A. A. Rockhill, M. Liserre, R. Teodorescu, and P. Rodriguez, "Grid-Filter Design for a Multimegawatt Medium-Voltage Voltage-Source Inverter," *IEEE Transactions on Industrial Electronics*, vol. 58, no. 4, pp. 1205–1217, 2011.
- [121] R. W. Erickson and D. Maksimović, *Fundamentals of Power Electronics*, second edition ed. Boston, MA: Kluwer Academic Publishers, 2004. [Online]. Available: <http://dx.doi.org/10.1007/b100747>
- [122] R. Sadeghi, S. M. Madani, and M. Ataei, "A New Smooth Synchronization of Brushless Doubly-Fed Induction Generator by Applying a Proposed Machine Model," *IEEE Transactions on Sustainable Energy*, vol. 9, no. 1, pp. 371–380, 2018.

- [123] Y. Zhang, J. Zhu, and J. Hu, "Model predictive direct torque control for grid synchronization of doubly fed induction generator," in *2011 IEEE International Electric Machines & Drives Conference (IEMDC)*. IEEE, 5/15/2011 - 5/18/2011, pp. 765–770.
- [124] R. Sadeghi, S. M. Madani, and M. R. A. Kashkooli, "Grid synchronization of brushless Doubly Fed Induction Generator using direct torque control," in *2016 7th Power Electronics and Drive Systems Technologies Conference (PEDSTC)*. IEEE, 2/16/2016 - 2/18/2016, pp. 53–57.
- [125] R. McMahon, A. Broekhof, and M. Tatlow, "Vector-controlled Grid Synchronization for the Brushless Doubly-Fed Induction Generator," in *7th IET International Conference on Power Electronics, Machines and Drives (PEMD 2014)*. Institution of Engineering and Technology, 8-10 April 2014, p. 0251.
- [126] J. Hu, J. Zhu, Q. Ma, and Y. Zhang, "Predictive direct virtual torque control of doubly fed induction generator for grid synchronization," in *2011 International Conference on Electrical Machines and Systems*. IEEE, 8/20/2011 - 8/23/2011, pp. 1–6.
- [127] J. Hu, J. Zhu, Y. Zhang, G. Platt, D. G. Dorrell, and Q. Ma, "Predictive direct control of doubly fed induction generator for grid synchronization in wind power generation," in *2011 IEEE Energy Conversion Congress and Exposition*. IEEE, 9/17/2011 - 9/22/2011, pp. 2381–2388.
- [128] J. Hu, J. Zhu, Y. Zhang, G. Platt, Q. Ma, and D. G. Dorrell, "Predictive Direct Virtual Torque and Power Control of Doubly Fed Induction Generators for Fast and Smooth Grid Synchronization and Flexible Power Regulation," *IEEE Transactions on Power Electronics*, vol. 28, no. 7, pp. 3182–3194, 2013.
- [129] J. Arbi, M.-B. Ghorbal, I. Slama-Belkhodja, and L. Charaabi, "Direct Virtual Torque Control for Doubly Fed Induction Generator Grid Connection," *IEEE Transactions on Industrial Electronics*, vol. 56, no. 10, pp. 4163–4173, 2009.
- [130] A. Yarahmadi, D. A. Khaburi, and H. Behnia, "Direct Virtual Torque Control of DFIG grid connection using Indirect Matrix Converter," in *2012 3rd Power Electronics and Drive Systems Technology (PEDSTC)*. IEEE, 2/15/2012 - 2/16/2012, pp. 115–120.
- [131] E.ON Netz GmbH, "Grid Code High and Extra High Voltage," Bayreuth, 2003.
- [132] S. Yang, T. Zhou, X. Zhen, X. Zhang, R. Shao, and L. Chang, "A SCR crowbar commutated with rotor-side converter for doubly fed wind turbines," in *2015 IEEE 6th International Symposium on Power Electronics for Distributed Generation Systems (PEDG)*. Piscataway, N.J.: IEEE, 2015, pp. 1–7.
- [133] N. R. Raju, "Regenerative and ride-through capability for AC drives through thyristor-based extensions of the diode front-end," in *Crossroads to innovation*. IEEE, 2003, pp. 1571–1575.
- [134] J. Vidal, G. Abad, J. Arza, and S. Aurtenechea, "Single-Phase DC Crowbar Topologies for Low Voltage Ride Through Fulfillment of High-Power Doubly Fed Induction Generator-Based Wind Turbines," *IEEE Transactions on Energy Conversion*, vol. 28, no. 3, pp. 768–781, 2013.
- [135] M. Ezzat, M. Benbouzid, S. M. Mueen, and L. Harnefors, "Low-voltage ride-through techniques for DFIG-based wind turbines: State-of-the-art review and future trends," in *IECON 2013*. Piscataway, NJ and Piscataway, NJ: IEEE, 2013, pp. 7681–7686.
- [136] C. Wessels, R. Lohde, and F. W. Fuchs, "Transformer based voltage sag generator to perform LVRT and HVRT tests in the laboratory," in *Proceedings of EPE-PEMC 2010*. [Piscataway, N.J.]: IEEE, 2010.

- [137] E. R. Collins and R. L. Morgan, "A three-phase sag generator for testing industrial equipment," *IEEE Transactions on Power Delivery*, vol. 11, no. 1, pp. 526–532, 1996.
- [138] A. Uphues, K. Notzold, R. Wegener, K. Fink, M. Bragard, R. Griessel, and S. Soter, "Inverter based test setup for LVRT verification of a full-scale 2 MW wind power converter," in *2013 15th European Conference on Power Electronics and Applications (EPE)*. IEEE, 2013, pp. 1–5.
- [139] V. Mendes, F. Matos, S. Liu, A. Cupertino, H. Pereira, and C. de Sousa, "Low Voltage Ride-Through Capability Solutions for Permanent Magnet Synchronous Wind Generators," *Energies*, vol. 9, no. 1, p. 59, 2016.
- [140] S. O. Zain Elabideen, A. A. Helal, and I. F. El-Arabawy, "Low Voltage Ride through Capability Techniques for DFIG-Based Wind Turbines," *World Academy of Science, Engineering and Technology, International Science Index 115, International Journal of Electrical, Computer, Energetic, Electronic and Communication*, vol. 10, no. 7, pp. 910–918, 2016.
- [141] D. Raca, "Practical Implications of Low Voltage Ride Through Requirements on Windturbine Power Conversion," *ELECTRONICS, Faculty of Electrical Engineering, University of Banja Luka, Bosnia and Herzegovina*, vol. 14, no. 2, pp. 3–11, DECEMBER 2010.
- [142] A. Wang, S. Shu, and Y. Wang, "Dynamic behavior of DFIG during asymmetrical voltage dips in a coupled simulation," in *2015 18th International Conference on Electrical Machines and Systems (ICEMS)*. [Piscataway, NJ] and [Piscataway, NJ]: IEEE, 2015, pp. 1051–1058.
- [143] A. Zuccato, P. Mattavelli, A. Abdelhakim, and A. Petucco, "Low-voltage ride through (LVRT) testing of full power converter for wind turbines using all-electronic equipment," in *Power electronics, machines and drives*. Stevenage, Hertfordshire, UK: The Institution of Engineering and Technology, 2016, p. 6.
- [144] M. Mohseni, S. M. Islam, and M. A. S. Masoum, "Impacts of Symmetrical and Asymmetrical Voltage Sags on DFIG-Based Wind Turbines Considering Phase-Angle Jump, Voltage Recovery, and Sag Parameters," *IEEE Transactions on Power Electronics*, vol. 26, no. 5, pp. 1587–1598, 2011.
- [145] M. A. Azzouz and E. F. Elsaadany, "An enhanced fault-ride-through capability of doubly-fed induction generators during grid faults," in *IEEE Power and Energy Society general meeting, 2012*. Piscataway, NJ: IEEE, 2012, pp. 1–7.
- [146] A. Al-Quteimat, C. Niewienda, and U. Schafer, "Low voltage ride through of doubly fed induction generator in wind power generation using crowbar solution," in *Proceedings, 2017 International Conference on Optimization of Electrical and Electronic Equipment (OPTIM) & 2017 Intl Aegean Conference on Electrical Machines and Power Electronics (ACEMP) : The Cheile Gradistei Fundata Complex, Brasov, Romania, 25-27 May 2017*. Piscataway, NJ: IEEE, 2017, pp. 667–674.
- [147] S. B. Pawar, A. M. Jain, and J. D. Patil, "Increasing low voltage ride through capability of doubly fed induction generator in wind energy transfer system during grid fault," in *International Conference & Workshop on Electronics & Telecommunication Engineering (ICWET 2016)*. Institution of Engineering and Technology, 26-27 Feb. 2016, p. 5.
- [148] F. Lima, A. Luna, P. Rodriguez, E. H. Watanabe, and F. Blaabjerg, "Rotor Voltage Dynamics in the Doubly Fed Induction Generator During Grid Faults," *IEEE Transactions on Power Electronics*, vol. 25, no. 1, pp. 118–130, 2010.

-
- [149] S. Swain and P. K. Ray, "Fault ridethrough and power quality improvement of Doubly-Fed Induction Generator based wind turbine system during grid fault with Novel Active Crowbar Protection design," in *Proceedings of the 2016 IEEE Region 10 Conference (TENCON)*, TENCON, Ed. [Piscataway, NJ]: IEEE, 2016, pp. 2628–2633.
- [150] L. Zhang, X. Jin, T. Ma, and Y. Tong, "An improved control scheme for Doubly Fed Induction Generator during grid fault ride-through," in *Proceedings 2012 3rd IEEE International Symposium on Power Electronics for Distributed Generation Systems*. [Piscataway, N.J.]: IEEE, 2012, pp. 301–306.
- [151] "en_e1zm,e1z1." [Online]. Available: https://www.tele-online.com/resources/data-sheets/en_e1zm,e1z1.pdf

List of Figures

1.1	Capacities of renewable power in world, BRICS (Brazil, Russian Federation, India, China and South Africa), EU-28 (European Union) and Top 6 Countries, 2016 [7].	2
1.2	Maximum power tracking for fixed and variable speed turbines.	3
1.3	Wind turbine configuration using Synchronous Generators.	3
1.4	Wind turbine configuration using Doubly Fed Induction Generators.	4
1.5	Sub-synchronous speed ($\omega_m < \omega_s$).	6
1.6	Hyper-synchronous speed ($\omega_m > \omega_s$).	6
2.1	Sectional view of the wound rotor induction machine.	11
2.2	The space vectors in the three reference frames.	19
3.1	DFIG system based wind power generation.	22
3.2	Flux vectors diagram in rotor reference frame.	24
3.3	Space vector representation of voltage vectors.	24
3.4	Rotor and stator flux trajectory in first three sectors with the active voltage vectors.	26
3.5	Conventional DTC scheme for DFIG.	27
3.6	a) Three-level hysteresis comparator for torque control, b) Two-level hysteresis comparator for flux control.	30
3.7	Voltage vectors in conventional DTC scheme, with: TI, TD and FI, FD: Increase and Decrease of Torque and Flux.	30
3.8	Switching frequency limiter.	31
3.9	Voltage vectors in twelve sector DTC scheme.	34
3.10	Voltage vectors in modified DTC scheme.	35
3.11	Electromagnetic torque.	37
3.12	(a) Rotor current in dq, (b) Rotor voltage in dq, and (c) Rotor flux.	37
3.13	(a) Three phase stator current, (b) Three phase stator voltage.	38
3.14	Active and reactive powers.	38
3.15	Rotor flux sectors for conventional DTC.	38
3.16	(a) Electromagnetic torque, (b) Rotor flux for twelve sectors DTC.	39
3.17	Rotor flux sectors for twelve sectors DTC.	39

3.18	(a) Electromagnetic torque, (b) Rotor flux with modified DTC.	39
3.19	Average switching frequency of DTC techniques.	40
3.20	Spectrum waveform of the stator current for: (a) Conventional DTC, (b) Modified DTC. (c) Twelve sectors DTC.	42
3.21	The space vector representation of stator and rotor fluxes in the rotor reference frame.	44
3.22	Voltage vectors in conventional DPC scheme.	44
3.23	Schematic diagram of DPC.	45
3.24	a) Active power hysteresis comparator, b) Reactive power hysteresis comparator.	47
3.25	(a) Active power, (b) Reactive power, with DPC.	47
3.26	Spectrum waveform with DPC for: (a) Stator active Power, (b) Stator reactive power.	48
4.1	Grid Side Converter equivalent circuit.	49
4.2	Vector control of the GSC.	51
4.3	Alignment of the d axis with the grid voltage space vector.	52
4.4	PLL block diagram.	56
4.5	PLL tracking for the simulated grid phase voltage and the phase angle.	57
4.6	Ideal LCL equivalent circuit	58
4.7	(a) and (b): Grid current and voltage without using filter, (c) and (d): Grid current and voltage with using filter.	61
5.1	DFIG configuration in synchronization process.	63
5.2	Phase 'a' of grid and stator voltages during synchronization process.	65
5.3	(a) Electromagnetic torque, (b) Rotor flux during synchronization.	66
6.1	Low voltage ride through requirement for German transmission codes (self-designed based on [69]).	68
6.2	Voltage control requirements during grid faults according to the grid codes [69].	69
6.3	DFIG under voltage dip.	70
6.4	The DFIG system with an impedance sag generator.	71
6.5	Grid voltage with three-phase 90% voltage dip at time 1 s for 150 ms.	72
6.6	(a) Rotor voltage, (b) Rotor current and (c) Stator current under 90% three-phase voltage dip at time 1 s for 150 ms.	72

6.7	(a) Rotor flux (DQ), (b) Stator flux (DQ) and (c) Electromagnetic torque under 90% three-phase voltage dip at time 1 s for 150 ms.	73
6.8	Grid voltage with 90% two-phase voltage dip at time 1 s for 150 ms.	73
6.9	(a) Rotor voltage, (b) Rotor current, and (c) Stator current under 90% two-phase voltage dip at time 1 s for 150 ms.	74
6.10	(a) Rotor flux (DQ), (b) Stator flux (DQ), and (c) Electromagnetic torque under 90% two phase voltage dip at time 1 s for 150 ms.	75
6.11	Grid voltage with 90% single phase voltage dip at time 1 s for 150 ms.	76
6.12	(a) Rotor voltage, (b) Rotor current, and (c) Stator current under 90% single phase voltage dip at time 1 s for 150 ms.	76
6.13	(a) Rotor flux (DQ), (b) Stator flux (DQ), and (c) Electromagnetic torque under 90% single phase voltage dip at time 1 s for 150 ms.	77
6.14	Active crowbar protection circuit.	79
6.15	(a) Crowbar current, (b) Rotor current, (c) Electromagnetic torque, (d) Rotor voltage, (e) Stator flux, and (f) Rotor flux during three phase voltage dip using different crowbar resistances.	81
6.16	a) Impedance based VSG, b) Coils details.	82
6.17	Fault detection circuit.	83
6.18	Generation of 100% voltage dip.	84
B.0	Electromagnetic torque, Rotor flux for 3.5 kW DFIG with: (a) Conventional DTC, (b) Modified DTC, and (c) Twelve DTC.	108
B.1	Rotor current, Stator current, Grid voltage for 3.5 kW DFIG with: (a) Conventional DTC, (b) Modified DTC, and (c) Twelve DTC.	109
B.2	Grid voltage, Rotor current, Stator current, and Electromagnetic torque for 3.5 kW DFIG during 90 % three phase voltage dip: (a) Without using crowbar protection, (b) With using crowbar protection.	110

List of Tables

3.1	Voltage vectors selection table, where (1,-1, and 0): denote increasing, decreasing, and constant torque and flux variables. (k-1): the previous sector, (k+1): the next sector.	24
3.2	Sector division for the flux position determination	28
3.3	Voltage vectors in conventional DTC scheme, with: TI, TD and FI, FD: Increase and Decrease of Torque and Flux.	31
3.4	Switching table for the twelve sector DTC.	33
3.5	Comparison of sectors zones for conventional and modified DTC.	35
3.6	Switching table of modified DTC	36
3.7	Comparison analysis between DTC algorithms.	41
3.8	Ripples percentage of torque and flux for DTC algorithms.	41
3.9	Voltage vectors selection table for DPC.	45
3.10	Switching table for the conventional DPC	47

Appendix A

System Parameters

A.1 Machine Parameters

Parameter	Symbol	2 MW	3.5 kW
Rated Power	P_n	2 MW	3.5 kW
Rated Frequency	F_n	50 Hz	50 Hz
Synchronous Speed	ω_s	1500 r.p.m	1500 r.p.m
Rated rms Line to Line Stator voltage	V_g	690 V	380 V
Rated rms Stator Current	I_s	1760 A	8.100 A
Rated rms Line to Line Rotor Voltage	V_r	2070 V	140 V
Rated rms Rotor Current	I_r	1807.400 A	17 A
Nominal Torque	T_{nom}	12732 N.m	23.700 N.m
Pole Pairs	P	2	2
Stator Resistance	R_s	2.600 m Ω	996.900 m Ω
Rotor Resistance	R_r	2.900 m Ω	268.800 m Ω
Rotor Resistance Referred to stator	R'_r	26.100 m Ω	1.476 Ω
Mutual Inductance	L_m	2.500 mH	186.640 mH
Stator Leakage Inductance	$L_{\sigma s}$	0.087 mH	12.327 mH
Rotor Leakage Inductance	$L_{\sigma r}$	0.087 mH	12.327 mH
Stator Inductance	$L_s = L_m + L_{\sigma s}$	2.587 mH	0.199 H
Rotor Inductance	$L_r = L_m + L_{\sigma r}$	2.587 mH	254.341 mH
Turns Ratio	u	0.34	0.54

A.2 DC Link Parameters

Parameter	Symbol	Value
DC link voltage	V_{DC}	1200 V
DC link capacitor	C_{DC}	15 mF
Modulation index	m	0.82
Carrier triangle signal amplitude	V_{tri}	1

A.3 GSC Control Parameters

Outer Control Loop (DC Voltage)		
Parameter	Symbol	Value
Controller Proportional Gain	$Kp_{(dc)}$	$0.4750 s^{-1}/V$
Controller Integral Gain	$Ki_{(dc)}$	$139.7059 s^{-1}$
Inner Control Loop (d and q Current)		
Controller Proportional Gain	$Kp_{(i)}$	$13.3333 s^{-1}/A$
Controller Integral Gain	$Ki_{(i)}$	$333.3333 s^{-1}$
Phase Locked Loop (PLL)		
Settling Time	T_{set}	30 ms
Damping Factor	ξ	0.707
Undamped Natural Frequency	ω_n	47.1476 rad/s
Controller Proportional Gain	$Kp_{(PLL)}$	$306.66 s^{-1}/V$
Controller Integral Gain	$Ki_{(PLL)}$	$47178.46 s^{-1}$

A.4 RSC Control Parameters

Parameter	Symbol	Value
Torque Hysteresis Band	HB_T	5% T_{nom}
Flux Hysteresis Band	HB_ψ	2% ψ_{nom}
Maximum Limited Switching Frequency	$f_{sw,max}$	5 kHz
Sample Time	T_{sDTC}	5 μ s

A.5 Fault Detection Parameters

Symbol	Description	Value
R_v	Input resistance of LV-25p	2.2 k Ω
R_p	Primary winding resistance of LV-25p	250 Ω
R_m	Measuring resistance	150 Ω
R_x, R_y, R_z	OPAMP circuit resistances	(2.5, 1.1, 6.8) k Ω

Appendix B

Results of 3.5 kW

B.1 Results of DTC Algorithms

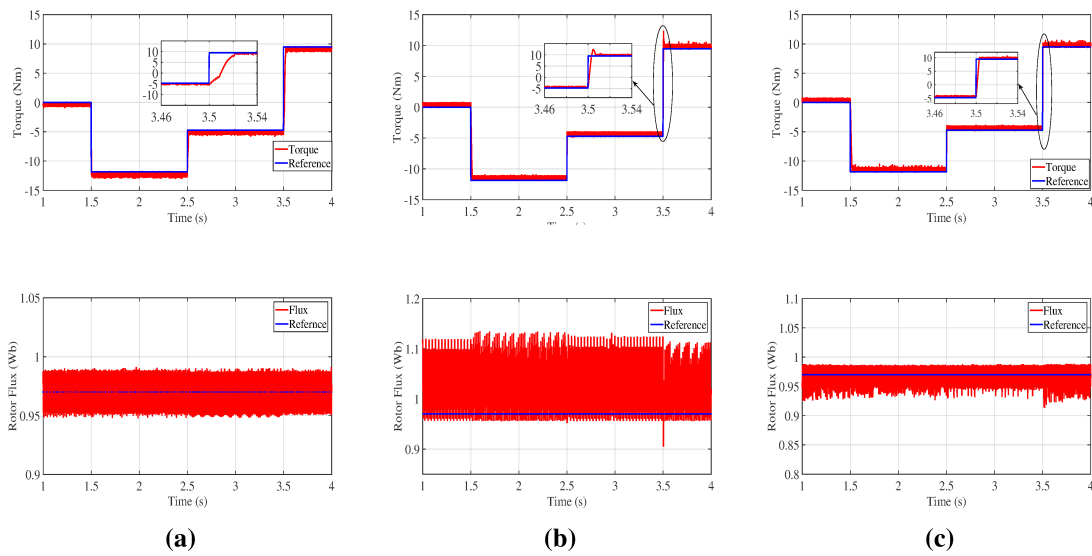


Figure. B.0 Electromagnetic torque, Rotor flux for 3.5 kW DFIG with: (a) Conventional DTC, (b) Modified DTC, and (c) Twelve DTC.

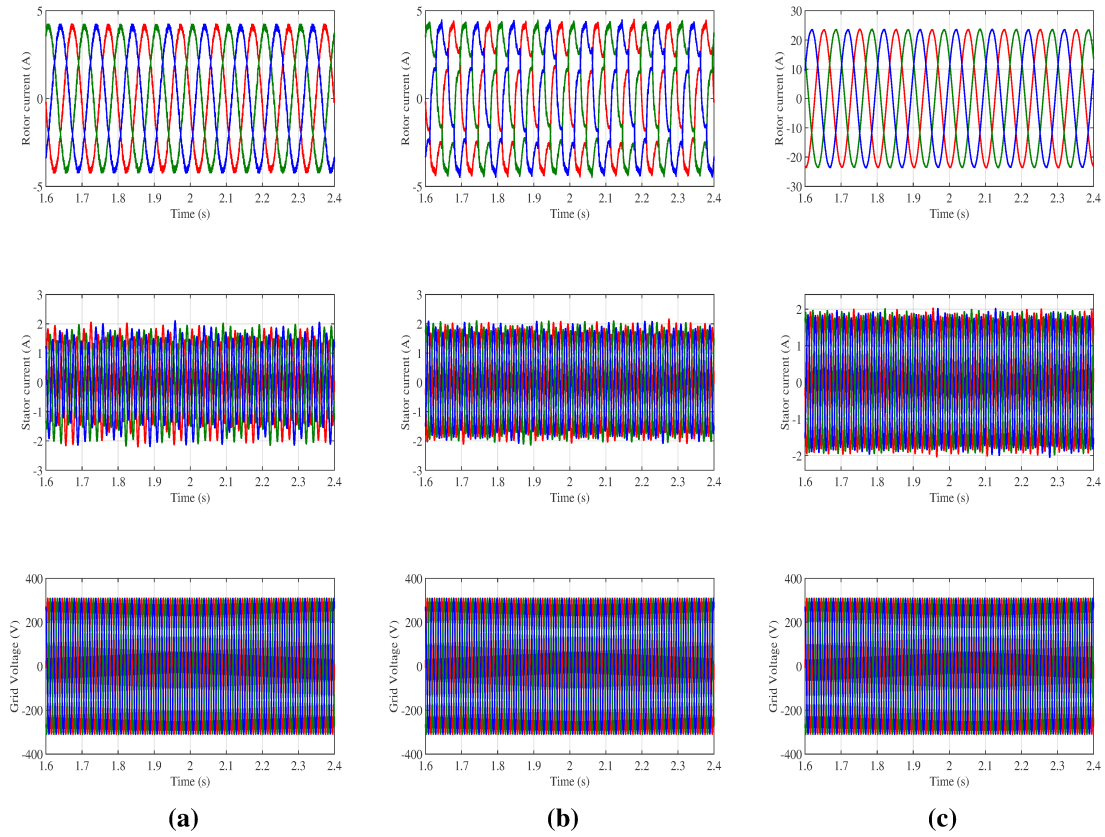


Figure. B.1 Rotor current, Stator current, Grid voltage for 3.5 kW DFIG with: (a) Conventional DTC, (b) Modified DTC, and (c) Twelve DTC.

B.2 DFIG under Three Phase Voltage Dip

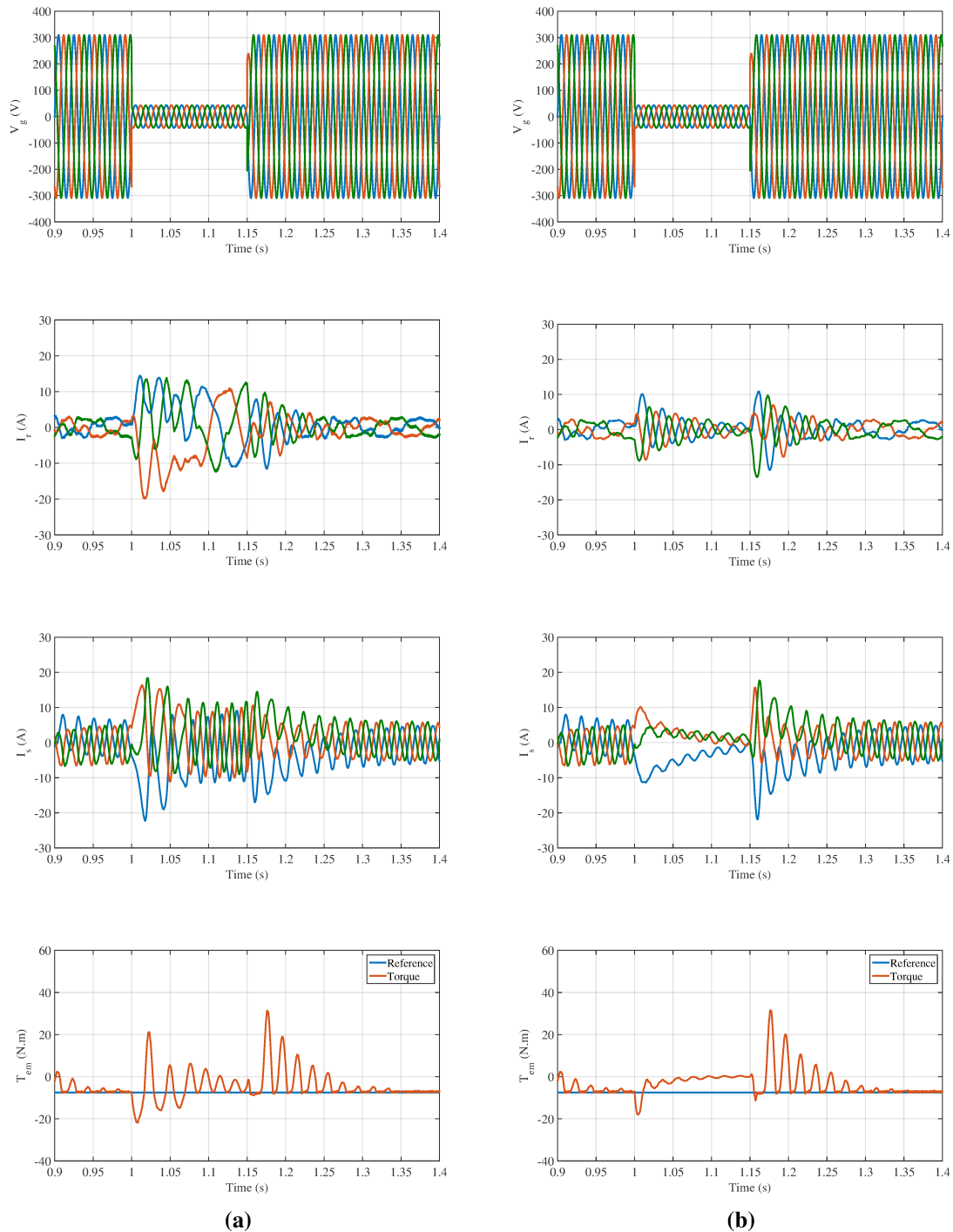


Figure. B.2 Grid voltage, Rotor current, Stator current, and Electromagnetic torque for 3.5 kW DFIG during 90 % three phase voltage dip: (a) Without using crowbar protection, (b) With using crowbar protection.